Observations of the Upper Ocean from Autonomous Platforms during the Passage of Extratropical Cyclone Epsilon (2020)

by

Lieutenant Junior Grade Michael T. Zimmerman,
United States Navy
B.S., United States Naval Academy (2021)

Submitted to the Department of Earth, Atmospheric
and Planetary Sciences
in partial fulfillment of the requirements for the degree of
Master of Science in Physical Oceanography
at the
MASSACHUSETTS INSTITUTE OF TECHNOLOGY
and the
WOODS HOLE OCEANOGRAPHIC INSTITUTION
September 2023

Author .....
Joint Program in Physical Oceanography
Massachusetts Institute of Technology &
Woods Hole Oceanographic Institution
11 August 2023

Certified by .....
Steven R. Jayne
Senior Scientist, Woods Hole Oceanographic Institution
Thesis Supervisor

Accepted by .....
Amala Mahadevan
Chair, Joint Committee for Physical Oceanography
Massachusetts Institute of Technology &
Woods Hole Oceanographic Institution

Observations of the Upper Ocean from Autonomous Platforms during the Passage of Extratropical Cyclone Epsilon (2020)

by

Lieutenant Junior Grade Michael T. Zimmerman,

United States Navy

Submitted to the Joint Program in Physical Oceanography
Massachusetts Institute of Technology &
Woods Hole Oceanographic Institution
on 11 August 2023, in partial fulfillment of the
requirements for the degree of
Master of Science in Physical Oceanography

Abstract

Hurricane Epsilon (2020) was a late-season, category-3 tropical cyclone that underwent extratropical transition and became Extratropical Cyclone Epsilon on 26 October. The upper ocean response to the passage of the storm was observed by three types of autonomous platforms: the eXpendable Spar buoy, the Air-Launched Autonomous Micro Observer profiling float, and two Seagliders. Taken together, this array enabled the rare collection of contemporaneous observations of the upper ocean, air-sea interface, and atmospheric boundary layer before, during, and after the passage of the storm. The evidence presented highlights how Extratropical Cyclone Epsilon broke down the residual North Atlantic summer stratification regime and accelerated the shift to the period of prolonged ocean cooling associated with winter. The significance of the synergistic capabilities of the array is two-fold: 1) comparing observations of the same parameters, taken from different platforms, enables a comprehensive approach to better understanding how storm-induced momentum, sensible heat, and moisture fluxes input kinetic and near-inertial energy into the ocean and thereby alter upper ocean structure; and 2) future, targeted deployments of similarly capable observational arrays will reduce the uncertainty of tropical and extratropical cyclone intensity forecasts by facilitating the assimilation of real-time subsurface ocean data into coupled numerical prediction models.

Thesis Supervisor: Steven R. Jayne
Title: Senior Scientist, Woods Hole Oceanographic Institution

Acknowledgments

While there are many that know some, there are only some that know the story, that is my time in Massachusetts, in its entirety; it is a story of personal realignment, loss, hardship, heartbreak, adventure, growth, love at first sight, and endurance; a story that has managed to explore nearly every corner of human emotion; a story of great triumphs, yet also certain defeats. To those who know some, I am very grateful that you are a part of my life. To those few who know the entire story, I am eternally indebted. My degree and this thesis are testaments to your incessant belief in and support of me, not only as a Joint Program student, but as a person. Allow me to mention you all by name and attempt to portray my gratitude.

After being delinquent in courting a research advisor, Steve Jayne reached out to me via email. After some back and forth, he graciously offered me his tutelage, likely out of pity. We met about a month later, and after only my first day of working for Steve, it was clear that I was in good hands. Yet, more assuringly, it was evident that I would gain a mentor and friend. I am deeply appreciative of Steve's personal and professional guidance. It has been formative in the personal realignment and growth that I referenced earlier. As I head to the Submarine Force, I will seek to emulate Steve's firm, yet always fair leadership; steadfast common-sense approach; easy-going disposition; sincere care for his people; and the dedication he has for his profession. Over the past two years, I have always been proud to announce myself as "Steve's student." And now, for a lifetime, I will be proud to call myself his friend. Thank you for everything, ***Doc***. Give ***Augie*** a treat for me. I will sincerely miss you both.

Through your example, I have learned to endure and attempt to be a light to all those around me. During my time in Massachusetts, I have done my best to hone those skills. You also taught me to be curious and inquisitive on the beach many years ago as you held a lady bug in your hands. That moment continues to motivate me to consider things deeply and study hard. I have kept the photograph encapsulating that moment on my nightstand throughout my time here. Thank you, ***Mom***, for emulating what hard work, dedication, sacrifice, and endurance looks like. Your continued love and support means the world to me.

I would be remiss to not mention my best friend, most trusted associate, and brother. We have been through quite a bit in recent memory. Although, as I reflect, I cannot help but smile; knowing that we have endured it together - laughing our way through it all. Just you and me, dude, and it always will be. As long as we have each other, it is all going to be okay. I do not know where I would be without you, ***Slim***. Take care of yourself. You most certainly deserve it.

And most of all, I have written so much, nearly all, of this story with a tiny dietitian, whom I met on one of my many ventures home. Her ceaseless love and support has powered me through the second half of graduate school, especially during the past few months while this thesis was being written. Her companionship is life's greatest gift, and it is to her that I am the most grateful. Thank you for altering the trajectory of my life, ***Paige***. I love you so big.

I would not have been equipped with the tools to pursue admission, let alone achieve success, in the Joint Program, without the influence of many people throughout the previous two chapters of my academic career. Unbounded gratitude is due to the United States Naval Academy Ocean and Atmospheric Sciences Department faculty, past and present. I owe specific thanks to CAPT Shawn Gallaher, Dr. Brad Barrett, Dr. Gina Henderson, soon-to-be Dr. Matt Burich, Dr. Cecily Steppe, CAPT Beth Sanabia, and Mr. Alex Davies. Similarly, I often thought back to my introduction to ocean science, mathematics, and physics at the Marine Academy of Science & Technology over the past two years. Thanks are due to Clare Ng, Jess Godkin, Chris Barnes, and most of all, Liza Basin, who provided me with the firm foundation necessary to pursue any sort of degree in Oceanography. Your expertise and continued encouragement have enabled my interests to become a passion.

I must also express gratitude to the Air-Deployed Profiling Instruments Group for welcoming me since my first day at WHOI. The relationship that I developed with my research group was rare amongst the student cohort. I offer sincere thanks to Jess Kozik, Deb West-Mack, Bill Dullea, and Alex Ekholm. Thanks is also due to Lucas Herron - my fellow disciple of Steve, office-mate, and friend. I will think of you all and Taco Tuesdays at Añejo very fondly for a long time. Volare sicut porcus.

I would like to acknowledge the 53rd Weather Reconnaissance Squadron - the World Famous Hurricane Hunters - for taking the time to get to know me and making KBIX and TISX feel like home. Thank you for flying me around the Caribbean, into the eye of a couple hurricanes, and letting me drop a few things along the way. There is truly nothing like the excitement of flying into a hurricane for the first time. Adjacently, I want to thank Manny Haenggi of the Naval Oceanographic Office. Manny is an excellent oceanographer, but a better colleague and friend. Most of all, thank you all for your friendship. The summers of 2022 and 2023 will be seared into my memory forever. I look forward to when we see each other again.

I offer many thanks to my co-authors of a manuscript of the same name, submitted to *Oceanography* and under peer review during the time of this writing. Thank you, John Toole, Jim Edson, Carol Anne Clayson, Casey Densmore, Luc Rainville, Craig Lee, and again, Steve and Alex. Your feedback was greatly appreciated, and your trust was never taken for granted. Due to the hard work of these scientists, this work, as well as the version in review, was supported by the Office of Naval Research under grant numbers N00014-18-1-2813, N00014-20-1-2765, and N00014-18-1-2780.

Last but not least, I am grateful to the Civilians Institution Office at the Naval Postgraduate School, who funded and supported my enrollment in the Joint Program. I vow to make this opportunity matter as a member of the Submarine Force.

"To know the laws that govern the winds, and to know that you know them, will give you an easy mind on your voyage round the world; otherwise you may tremble at the appearance of every cloud. What is true of this in the trade-winds is much more so in the variables, where changes run more to extremes."

- Joshua Slocum, *Sailing Along Around the World*

Contents

THIS PAGE INTENTIONALLY LEFT BLANK

List of Figures

THIS PAGE INTENTIONALLY LEFT BLANK

List of Tables

THIS PAGE INTENTIONALLY LEFT BLANK

Chapter 1

Introduction

1.1 Scope

This thesis presents the findings of an observational array, comprised of the eXpendable Spar buoy, the Air-Launched Autonomous Micro Observer profiling float, and two Seagliders, that contemporaneously observed the passage of the remnants of Extratropical Cyclone Epsilon in late October of 2020 as a part of the Office of Naval Research (ONR)-funded Near-Inertial Shear and Kinetic Energy in the North Atlantic experiment (NISKINe) Departmental Research Initiative (DRI). In support of the ONR NISKINe DRI, the generation, propagation, and decay of near-inertial internal waves and input of kinetic energy into the upper ocean were investigated; specifically in relation to how these phenomena modulated upper ocean structure as a result of the passage of the remnants of Extratropical Cyclone Epsilon. The framework of this study summarizes the development of a synergistic approach to observing hurricanes and extratropical cyclones using autonomous systems and elucidates how this complimentary methodology should be used during future observational campaigns and targeted storm deployments. Future iterations of this, or similarly capable, observational arrays will facilitate a better understanding of the physics that govern the evolution of upper ocean dynamics during and after a strong forcing event such as a hurricane or extratropical cyclone.

1.2 Near-Inertial Shear and Kinetic Energy in the North Atlantic experiment (NISKINe) Background

The ONR NISKINe DRI aimed to better understand the physics that govern the near-inertial response to surface forcing. More specifically, its goals were to investigate how mesoscale and synoptic-scale variability impacted the generation, propagation, and decay of near-inertial internal waves and input of kinetic energy into the upper ocean; thereby enabling more accurate predictive capabilities for the evolution of vorticity, strain, and shear fields after strong forcing events. Further, the experiment sought to better conceptualize the differences between the generation of high-mode near-inertial internal waves, which drive local mixing, and low-mode near-inertial internal waves, which propagate away from the storm environment. Motivating this DRI were previous observations of linkages between mesoscale features, near-inertial internal waves, and modulation of upper ocean structure (Figure 1-1; [1, 2]) [7, 6, 8]. Such modulation pathways affect acoustic propagation in the surface duct and main sound channel [9, 10, 11], yet despite these observations, poor understanding of the dynamics at play remain.

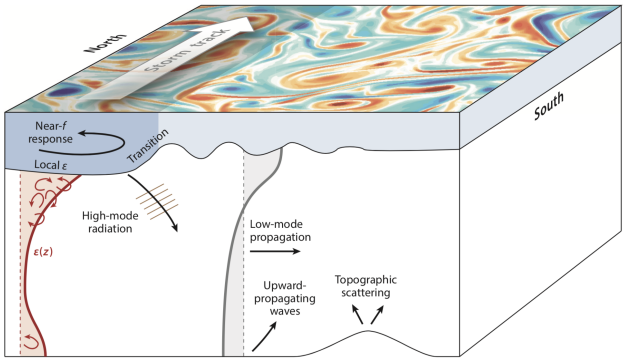

Figure 1-1: Life cycle of the near-inertial internal wave. After a storm (white arrow), upper ocean responses occur according to the local Coriolis frequency (black, cyclonically rotating arrow), which includes the generation near-inertial internal waves. High-mode near-inertial internal waves (black, downward and equatorward pointing arrow) are associated with strong velocity shear, which results in local mixing (represented by ε[z]). Whereas, low-mode near-inertial internal waves (gray structure evolving with depth) propagate away from the storm environment. Figure courtesy of Simmons & Alford (2012) [1], after adaptation by Alford et al. (2015) [2].

The North Atlantic, just south of Iceland, was selected as the ideal observational area to pursue the answers to these research questions given its consistently strong wind forcing, frequency of mature storms, and energetic mesoscale fields. The ONR NISKINe DRI consisted of a pilot cruise in 2018, two major field campaigns in 2019 and 2020, and an analysis period concluding at the time of this writing. The results, analyses, and conclusions of the ONR NISKINe DRI are currently under peer review. Those accepted will be compiled and published as a Special Issue of *Oceanography*. The prospective release date is Fall 2023.

1.3 Motivation

The motivations behind the science presented in this thesis, aside from supporting the ONR NISKINe DRI, are as follows:

1. To explore the surface and subsurface effects of Extratropical Cyclone Epsilon in order to conceptualize how extratropical cyclones, otherwise referred to as nor'easters, are life-threatening natural disasters, not dissimilar to hurricanes. These implications are considered with the context of the grave societal and economic impacts of the "Perfect Storm" and "Superstorm" Sandy in mind.

2. Most importantly, this study aims to advocate for future deployments of similarly capable observational arrays, which can assimilate subsurface ocean data into coupled numerical prediction models in real-time ahead of hurricanes and extratropical cyclones. Thus, allowing forecasters to make more accurate predictions, which will keep the public more informed, and ultimately, safer. While satellite imagery resolves important sea surface features, subsurface ocean observations are key to more accurately forecasting storm intensity. Though this fact is well-documented, subsurface ocean sensors are sparingly deployed in support operational storm forecasting.

Both of these motivations are further described in Chapters 3 and 4, respectively. However, introducing them here equips the reader with the requisite context to grasp

the consequence of this research.

1.4 Organization

The remainder of this thesis is organized as follows:

- Chapter 2 briefly introduces how near-inertial and kinetic energy affect the upper ocean and identifies hurricanes and extratropical cyclones as potential sources of such modulation.
- Chapter 3 details why extratropical cyclones are worth investigating through the context of the case studies mentioned in Section 1.3.
- Chapter 4 evaluates how leveraging autonomous instruments can improve hurricane and extratropical cyclone intensity forecasts, and why such advancements are necessary and worthy investments.
- Chapter 5 outlines the 2020 NISKINe deployment, including a detailed description of each autonomous platform within the observational array.
- Chapter 6 assesses the surface ocean response to the passage of the remnants of Extratropical Cyclone Epsilon.
- Chapter 7 examines the subsurface ocean response to the passage of the remnants of Extratropical Cyclone Epsilon.
- Chapter 8 summarizes the contributions of this thesis and describes the way ahead for this area of scholarship.

Chapter 2

Upper Ocean Modulation Pathway

2.1 Near-Inertial Internal Waves

Atmospheric forcing at the air-sea interface, such as time-variable wind stress, can incite motions in the upper ocean that oscillate at or near the local Coriolis frequency. Thus, these oscillations are governed by frequencies that are constrained by the local rotation rate of earth. Such phenomena exchange momentum across the air-sea interface, which drives internal waves and currents [12, 13, 14]. Motions at these near-inertial frequencies, so called near-inertial internal waves (NIWs), dominate upper ocean velocity shear. The restoring forces for NIWs are gravity and Coriolis frequency. Consequently, when they grow large enough or propagate sufficiently poleward, they break non-linearly; akin to surface gravity waves becoming unstable in the surf zone after reaching the requisite steepness ratio. The breaking of NIWs significantly contributes to mechanical mixing of the ocean [15, 16].

Historically, the transition from fall to winter is when the North Atlantic experiences the strongest atmospheric forcing [6, 17, 18]. Many storms transport dry and cold continental air masses over the ocean. This drives some of the largest known momentum, sensible heat, and moisture fluxes across the air-sea interface. A key characteristic of the surface forcing during the passage of a mid-latitude storm is that the cyclonic rotation rate is on a comparable time scale to the near-inertial motion that develops in response, suggesting a possible resonant response exists in the upper

ocean [19].

Near-inertial motions can create significant velocity shear at the base of the mixed layer, which enhances vertical mixing and directly affects the momentum, sensible heat, and moisture balances of the mixed layer [20, 21]. The temporal alignment of the wind stress and ocean current vectors can result in significant wind work being done on near-inertial motions in the mixed layer [22]. A fraction of this near-inertial energy can radiate across the mixed layer base and propagate into the stratified ocean interior below [23].

While a portion of this energy is lost at the mixed layer base due to turbulent mixing processes and conversion to potential energy, some, in the form of propagating low-mode NIWs, can radiate downward, beyond the mixed layer, and laterally [24]. Such propagation has been observed modulating upper ocean structure far away from a generation area [1, 15]; whereas, high-mode NIWs drive mixing locally in the generation area. While their effects are evident, details about the generation, evolution, and decay of NIWs still remain unresolved. However, recent advances in theory, modeling, and observations have highlighted mesoscale and synoptic-scale atmospheric features, and their impact on upper ocean vorticity, strain, and shear fields, as potentially important mechanisms in the NIW life cycle. Significant synoptic-scale systems features worth investigating in this regard are hurricanes and extratropical cyclones [25].

2.2 Synoptic-Scale Sources

Hurricanes (tropical cyclones; TCs) are warm-core, non-frontal, synoptic-scale systems that feature organized, deep moist convection and a closed surface wind field that cyclonically rotates about a definable center. TCs originate over the tropical and subtropical oceans and are steered by upper-level atmospheric flows. If TCs propagate northward into the extratropics, they preferentially lose their tropical characteristics such as a symmetrical, warm-core structure [26], which causes the wind field to expand and become increasingly asymmetric [27]. A degradation of tropical characteristics is linked to the shift from a barotropically-driven, convective regime in the tropics

to the baroclinically-driven extratropics. Oftentimes, this dynamical regime shift is evident as the TC will weaken and dissipate, or it will evolve into a post-tropical cyclone, which can either be a frontal (extratropical cyclone; ETC) or non-frontal low pressure system (Figure 2-1; [3]) [26, 28]. The National Weather Service (NWS) uses the term "post-tropical" to refer to any closed low-pressure system that no longer qualifies as a TC but continues to pose danger in the form of damaging winds and heavy rains.

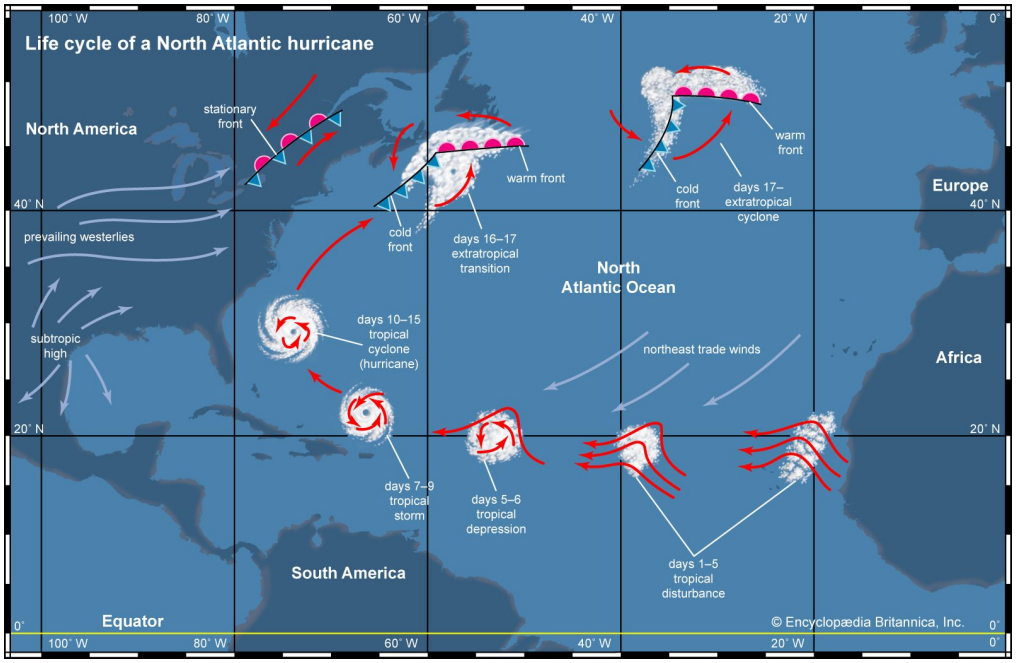

Figure 2-1: Typical life cycle of a North Atlantic TC, including transition to an ETC in part due to frontal development. Figure courtesy of Flynn (2023) [3].

The public largely acknowledges that TCs, regardless of potential landfall, can be life-threatening natural disasters. However, when a TC is downgraded in intensity, according to the Saffir-Simpson Hurricane Wind Scale (Table 2.1; [29]), or stripped of its TC-status altogether, there is a common misconception to no longer consider it a serious threat [26]. Sometimes, storm evolution and associated changes in classification can cause media coverage to cease and government-issued warnings to read less urgently, be downgraded, or be called off completely. Yet, these storms often remain life-threatening and potentially pose an even greater threat to the public than the previously forewarned TC [30].

Table 2.1: The Saffir-Simpson Hurricane Wind Scale rates TC intensity based on average one-minute wind speed observations and provides an estimation of property damage. Major hurricanes (Category 3+; italicized) can cause devastating to catastrophic wind damage and loss of life. While tropical depressions and tropical storms are not officially a part of the scale, it is useful for the reader to take note of their characteristics.

Category	**Sustained Winds**	**Damage Description**
Tropical Depression	0-33 kt 0-38 mph	-
Tropical Storm	34-63 kt 39-73 mph	-
1	64-82 kt 74-95 mph	Very dangerous winds will produce some damage.
2	83-95 kt 96-110 mph	Extremely dangerous winds will cause extensive damage.
3	*96-112 kt* *111-129 mph*	*Devastating damage will occur.*
4	*113-136 kt* *130-156 mph*	*Catastrophic damage will occur.*
5	*137+ kt* *157+ mph*	*Catastrophic damage will occur.*

2.3 Extratropical Cyclones

Many TCs that originate and propagate net-northward in the Atlantic Ocean basin transition to ETCs after entering the mid-latitudes by a process called extratropical transition (Figure 2-1; [3]). This occurs especially during late fall when the meridional temperature gradient is enhanced. As a TC propagates northward, the baroclinic influence of the extratropics, such as large-scale temperature contrasts between warm and cold air masses, leads to an increased likelihood for the storm to interact with synoptic-scale atmospheric features such as upper-level troughs or fronts [3, 27, 28]. The coupling of systems originating from different dynamical regimes sets the stage for extratropical transition to occur.

There is no traditional, rigorous meteorological definition for extratropical transition. However, it is loosely defined by some combination of the following, mainly satellite-borne, observations: 1) decrease of deep moist convection; 2) erosion or disorganization of the low-level center or "eye"; 3) dissipation of the high-cloud canopy;

4) frontal development; 5) high-level clouds developing a comma-shaped appearance; 6) asymmetrical wind and precipitation fields; 7) increase of the tropical storm (TS)-force surface wind radius; and 8) storm propagation over sea surface temperatures (SSTs) less than 26°C [26, 31]. Some or all of these observations indicate that the internal structure and dynamics of the TC are evolving or have fully transitioned. Soon after these changes are identified, the National Hurricane Center (NHC) will reclassify a TC as an ETC.

THIS PAGE INTENTIONALLY LEFT BLANK

Chapter 3

Extratropical Cyclone Case Studies

Regardless of the transitional pathway or observation of key transitory milestones, ETCs are fast-moving, powerful storms that continue to produce TC-scale winds, intense rainfall, and large waves despite their non-TC status [26, 28]. Thus, they continue to pose a significant threat in many of the same ways that a TC would. Two such case studies of costly and fatal ETCs are seared into the lexicon of those affected as the "Perfect Storm" (1991) and "Superstorm" Sandy (2012). While both of these storms originated as TCs, they caused devastating damage as ETCs. This context makes studying their unique life cycles a worthwhile research endeavour.

3.1 The Perfect Storm (1991)

Synoptic History

From 1988 to 1990, the Atlantic Ocean basin featured above-average TC activity, yet 1991 was uniquely dormant. No storm south of 25°N reached TC-intensity, and for only the third time in the twentieth century, no storm reached TS-, let alone TC-intensity, over the Gulf of Mexico [32]. The relative quietness throughout the season proved to be an eerie, foreshadowing quietness for New Englanders, who surely remember the 1991 Atlantic TC Season. In late August and then again in late October, the only two systems to make landfall in North America, TC Bob and the colloquially

named Perfect Storm, devastated the region [32].

The Perfect Storm of late October and early November was the result of the interaction between TC Grace, an unnamed ETC (hereafter, Unnamed ETC), and a cold front, associated with Unnamed ETC, that presided over the region (Figure 3-1; [32, 33]). The incipient circulation of Unnamed ETC formed on 26 October as a small depression along a stationary front in the Midwest region of the United States. By 1800 UTC 28 October, it developed into an ETC southeast of Nova Scotia, Canada [33, 34]. Meanwhile, TC Grace formed at 0000 UTC 28 October, approximately 240 km south of Bermuda, and slowly propagated north-northwest [32]. Later that evening, the elongated cold front trailing behind the powerful and expansive Unnamed ETC transited through South Carolina, while TC Grace was transiting northward, west of Bermuda. The eastward upper atmospheric outflow along the southern quadrants of Unnamed ETC, combined with the frontal boundary, steered TC Grace out to sea. However, before dissipating or evacuating the area, TC Grace was absorbed by Unnamed ETC at 1800 UTC 29 October, resulting in a massive transfer of energy [32, 33]. By the morning of 30 October, the coupling of the three synoptic-scale atmospheric features formed the hybrid storm that would become known as the Perfect Storm (Figure 3-1).

By 1200 UTC 30 October, while located approximately 630 km south of Halifax, Nova Scotia, the Perfect Storm considerably strengthened as sustained surface wind speeds increased to TS-intensity and 78 kt gusts were observed, while the local surface pressure minimum deepened to 972 mb [32]. By 0000 UTC 02 November, a United States Air Force weather reconnaissance aircraft observed 86 kt flight-level winds, suggesting that the system had reached a peak intensity equivalent to a category-1 or -2 TC before making landfall (Figures 3-1 and 3-2). There was no change in classification to avoid public confusion throughout New England and the Canadian Maritimes; however, in reanalysis, NHC and the Meteorological Service of Canada formally refer to this phase of the Perfect Storm as Unnamed TC.

Damages

The Perfect Storm inundated the North Atlantic with large waves (Figure 3-3), maximally measuring 30.8 m, a regional record, by a Canadian buoy south of Nova Scotia [32]. Its heavy precipitation and storm surge caused extreme flooding along the Mid-Atlantic, New England, and Eastern Canadian coastlines [34, 35]. Although winds were destructive (Figure 3-4), they were not remarkable in the context of ETC-induced wind speeds. However, the Perfect Storm was extraordinarily large, as TS-level winds blew over a 500 km radius for approximately 114 hours [33]. While the Perfect Storm made landfall near Halifax, Nova Scotia, New England experienced the costliest damages that were estimated at $200 million dollars and 50,000 households left without power. Further, the unusual trajectory of the hybrid storm caught many fishing vessels off guard and led to 13 lives lost [36]. Of note, the closest point of approach of the Perfect Storm to New England was approximately 200 km southeast of Nantucket; combined with the storm coinciding with a neap tide, the upper-level atmospheric flow and lunar cycle likely spared New England from far greater damage.

The triad of coupled synoptic-scale features formed a uniquely dangerous storm that could only be described by Bob Case, NWS Boston Deputy Meteorologist In Charge, as, "Perfect." The use of that word quickly transcended the storm into local and international legend: first in the form of a 1997 bestselling novel, *The Perfect Storm*, by Sebastian Junger [36]; and then afterwards in the critically acclaimed 2000 film of the same name, which starred George Clooney, Mark Wahlberg, and Diane Lane. Both of these works detailed the loss of the *Andrea Gail*, a Gloucester, Massachusetts, based commercial fishing vessel, which accounted for 6 of the lives lost during the Perfect Storm.

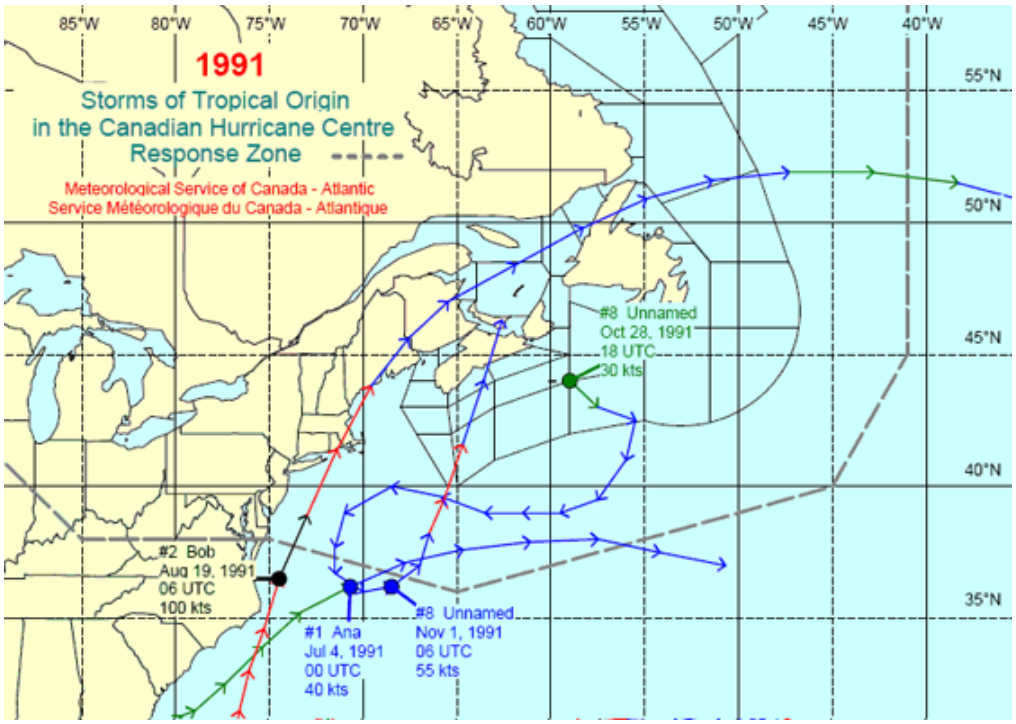

Figure 3-1: 1991 Canadian-TC summary, highlighting the best track positions for the Perfect Storm, referred to as Unnamed TC/ETC, from 28 October to 02 November. Figure courtesy of the Meteorological Service of Canada.

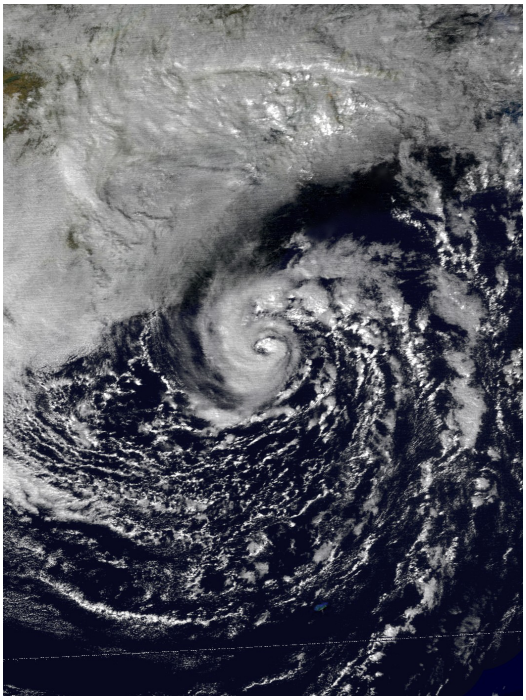

Figure 3-2: The Perfect Storm as viewed by GOES-7 at 1900 UTC 01 November. Satellite image courtesy of NOAA.

Figure 3-3: Waves crashing into homes Scituate, Massachusetts, due to the passage of the Perfect Storm. Photograph courtesy of the Boston Globe Staff.

Figure 3-4: Destruction caused by the wind field of the Perfect Storm in Scituate, Massachusetts. Photograph courtesy of Barry Chin of the Boston Globe.

3.2 Superstorm Sandy (2012)

Synoptic History

More recently, Superstorm Sandy was a typical, late-season TC that formed in the southwestern Caribbean Sea on 1200 UTC 24 October approximately 150 km south of Kingston, Jamaica. TC Sandy, first, made landfall in Jamaica as a category-1 TC at 1900 UTC 24 October, which was the first Jamaican landfall since TC Gilbert in 1988. Its second landfall was as a 100-kt, category-3 TC over eastern Cuba at 0525 UTC 25 October. Thereafter, it weakened below TC-status, however, the radius of TS-force winds would approximately double by 0000 UTC 27 October (Figure 3-5). It would grow as large as 800 km before reaching New Jersey two days later; classifying TC Sandy as the largest TC since 1988 [4, 37].

At 1200 UTC 27 October, the storm was reclassified as a category-1 TC as it exited the Greater Antilles. Although by then, it started to exhibit extratropical characteristics: the radius of maximum winds continued its massive expansion; asymmetry as the strongest winds were observed in the western quadrants of the storm; and the formation of two nearby fronts [4]. By early morning on 29 October, TC Sandy encountered an anomalous, extratropical blocking pattern, which prevented its transit out to sea and instead forced it further northward (Figures 3-5 and 3-6). This synoptic-scale feature provided sufficient baroclinic forcing, in combination with transit over the warm Gulf Stream, for TC Sandy to re-intensify [38]. By 1200 UTC, TC Sandy reached a secondary peak intensity as an 85-kt, category-1 TC [4]. This interaction initiated extratropical transition.

After taking aim at southern New Jersey, TC Sandy encountered much cooler waters and a cold air mass presiding over the Mid-Atlantic region, which accelerated extratropical transition. Also, a deep trough presiding over the southeastern United States helped increase the translation speed of the storm to 20 kt [4]. The 2100 UTC 29 October surface analysis revealed an occluded front wrapping into center of circulation, while the temperature gradient along a newly formed warm front increased. By that time, the storm lacked organized, deep moist convection and the central

dense overcast had dissipated. Consequently, NHC stripped Sandy of TC-status and reclassified the system as ETC Sandy [4]. At this time, the center of circulation was only 83 km southeast of Atlantic City, New Jersey (Figure 3-6). ETC Sandy made landfall at 2330 UTC 29 October near Brigantine, New Jersey, equivalent in intensity to a category 1-TC with a minimum surface pressure of 945 mb (Figure 3-5; [4]).

Damages

Superstorm Sandy effectively surprised the public, causing catastrophic damage along the New Jersey and New York coastlines. Damages eclipsed $85 billion dollars, which ranks Superstorm Sandy as fifth-costliest United States landfalling storm after adjusting for inflation and other normalization factors. Only TCs Katrina (2005), Harvey (2017), Ian (2022), and Maria (2017) were more economically disastrous [4, 39]. Further, 150 lives perished, which was the most fatalities caused by a storm outside the southern United States since TC Agnes in 1972 [4, 40]. Several coastal New Jersey and New York towns, such as Monmouth Beach and Ocean Beach Unit II, were devastated by extreme winds and storm surge of Superstorm Sandy (Figures 3-7 and 3-8). The boardwalks of Seaside Heights, Asbury Park, among other shoreline developments were completely destroyed.

Storm surge in New York City exceeded 3 m; and combined with heavy rains, a significant amount of Lower Manhattan streets, subway lines, and tunnels were flooded. In New Jersey, the highest storm surge recorded was 2.61 m at Sandy Hook Gateway National Recreation Area; however during the storm, the tide gauge failed and ceased reporting so this is likely an under-representation of the inundation [4]. The infrastructure of the Marine Academy of Science and Technology, a high school located 2.5 km from the northern most point of Sandy Hook, was destroyed, causing faculty and students to relocate until the following school year.

The effects of Superstorm Sandy were not isolated to New Jersey and New York. Its expanse was felt throughout the Mid-Atlantic and Northeast, highlighted by more than 20,000 flights cancelled and the accumulation of over 1 m of snow throughout West Virginia, Tennessee, and Maryland. Power outages occurred from North

Carolina to as far north as Quebec, Canada, to as far west as Illinois. In total, approximately 9 million households experienced power outages, which lasted months in some areas [4]. This included a two-day closure of the New York Stock Exchange; its longest weather-related closure since the Great Blizzard of 1888 that covered the surrounding area with approximately 5 feet of snow.

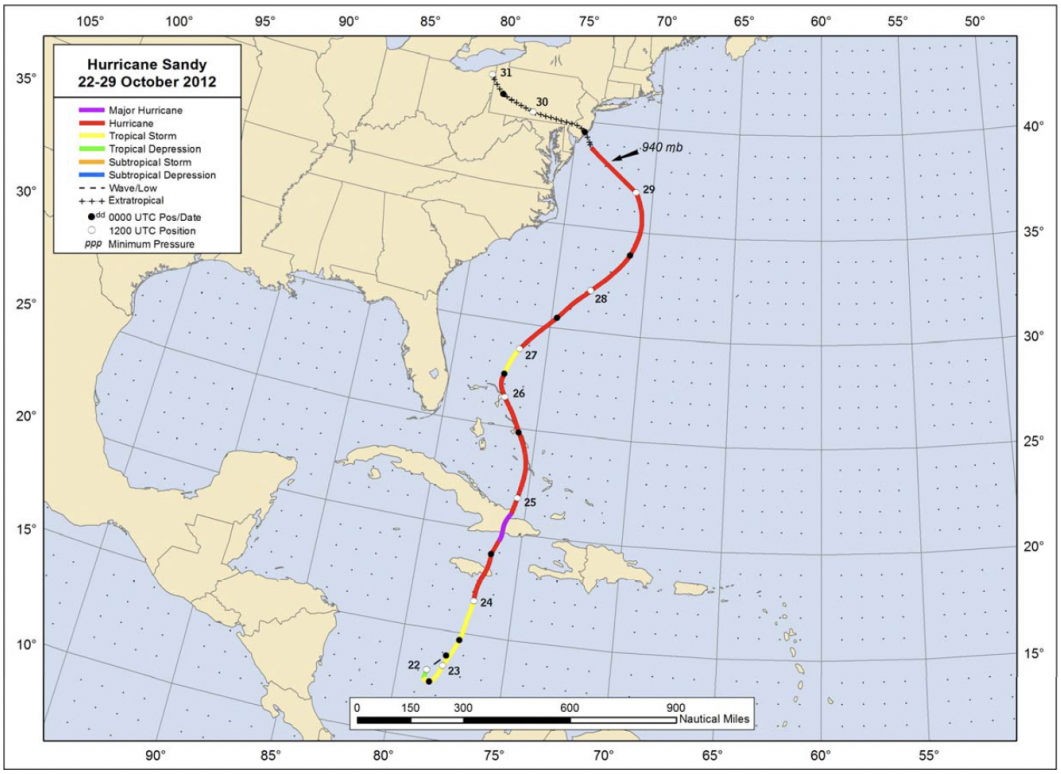

Figure 3-5: Best track positions for Superstorm Sandy from 0000 UTC 22 October to 1200 UTC 31 October. Figure from Blake et al. (2013) [4]).

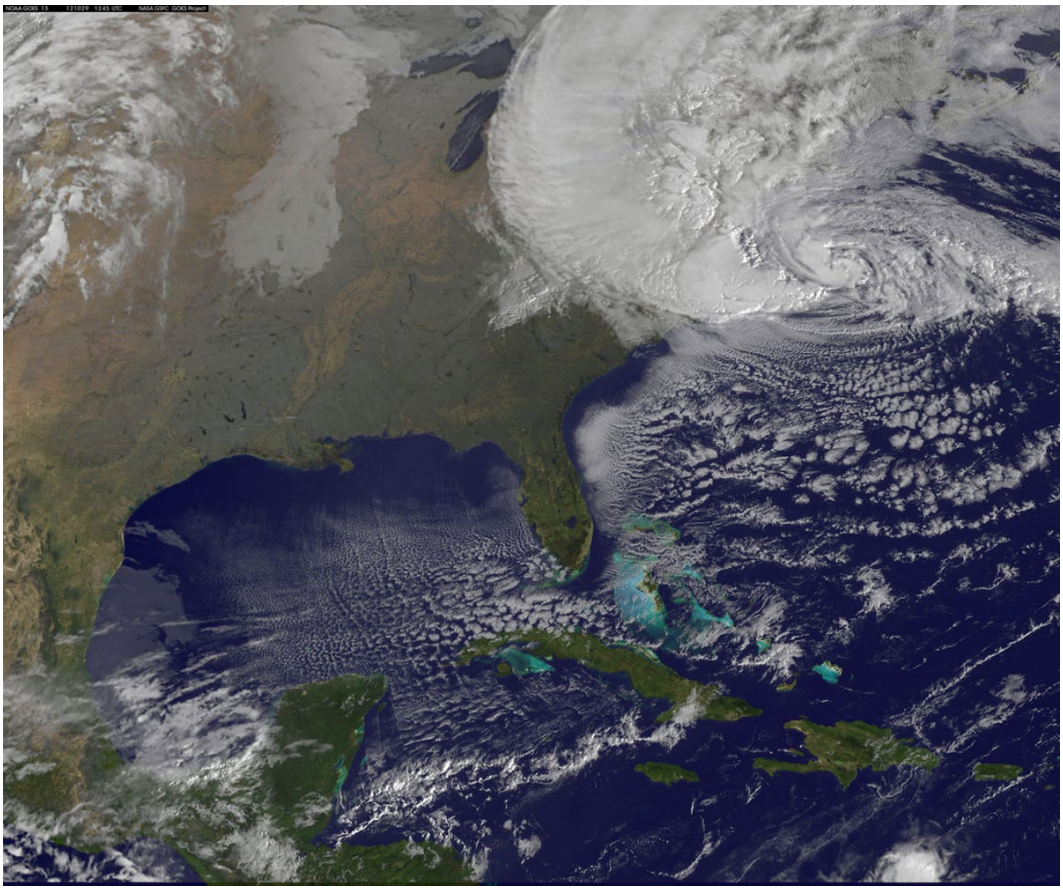

Figure 3-6: TC Sandy beginning its extratropical transition as viewed by GOES-13 at 1310 UTC 29 October. The storm would make landfall as ETC Sandy 10 hours later. Satellite image courtesy of NOAA.

Figure 3-7: The Casino Pier amusement park in Seaside Heights, New Jersey, destroyed by Superstorm Sandy. The Jet Star roller coaster is seen partially submerged in the surf zone, where it would remain until May. Photograph courtesy of Mario Tama of Getty Images.

Figure 3-8: Storm surge flooded the base of the Mantaloking Bridge and State Route 35 in Mantaloking, New Jersey, such that an inlet formed between the Barnegat Bay and Atlantic Ocean. Photograph courtesy of Master Sergeant Mark Olsen of the United States Air Force.

Chapter 4

Leveraging Autonomous Instruments

4.1 Identifying an Observational Gap

Not only do some ETCs like the Perfect Storm or Superstorm Sandy pose a comparable, even greater, threat to the public than TCs, but they present a significant forecasting challenge. Further complicating the matter, most extratropical transition events happen while a storm is over the open-ocean, such that satellite diagnostic techniques are the only tools typically available to observe evolving storm characteristics. This makes assessing storm conditions a very hard problem for forecasters to solve and leaves room for considerable error. While satellites are leveraged to provide data for coupled numerical prediction model initialization, the lack of in situ observations of the atmospheric boundary layer and upper ocean, as well as uncertainties in satellite observations due to clouds and precipitation, causes significant errors in the initialization [41, 42, 43]. As a result, monitoring extratropical transition events, as well as predicting ETC intensity, is incredibly challenging; even for the most experienced forecasters using the most advanced coupled numerical prediction models. These factors are major causes for concern as accurate ETC forecasts are critical to limiting loss of life and property damage, despite the non-TC status of the storm. One solution to bolster ETC observational and forecasting efforts is to strategically deploy autonomous and Lagrangian platforms and sensors (ALPS; [44]) ahead of and in the storm environment [45, 46].

4.2 Necessity for Subsurface Observations

While accurate storm track forecasting has significantly improved over the past few decades, forecasting storm intensity lags behind [47]. However, and fortunately, forecasts of storm intensity have slowly, but steadily improved since the early 2000s [48], in part because of increased subsurface ocean observations that are designed to support storm forecasting [45]. ALPS such as surface drifters, profiling floats, and gliders have been used to observe upper ocean structure before, during, and after TC passage since at least 2004 when Electromagnetic-Autonomous Profiling EXplorer (EM-APEX; [49]) floats were deployed ahead of Hurricane Frances (2004) during the Coupled Boundary Layer Air-Sea Transfer program (CBLAST; [50, 51, 52]). In a post-storm analysis, Sanford et al. (2011) [41] posited that the utility and unique capabilities of profiling floats made them prime candidates to investigate the dynamical responses of the upper ocean after significant forcing events in future studies [41, 53, 54]. These observations supported the theoretical model by Price (1981) [55] for explaining how the passage of a TC affects upper ocean structure.

Thereafter, Halliwell et al. (2011) [56] identified that ALPS, specifically profiling floats, were proficient for initializing coupled numerical prediction models, and that the integration of subsurface ocean data produced more credible intensity forecasts by allowing more accurate latent and sensible heat fluxes across the air-sea interface to be derived [42, 56, 57, 58]. TCs are primarily fueled by the ocean, thus the energy fluxes which govern their sensitivity are sensitive to subsurface properties, such as upper ocean heat content and stratification [59, 60, 61]. Both of these measurements are necessary to accurately initialize the oceanic components of coupled numerical prediction models in order to predict the necessary variables that couple the ocean and atmosphere such as latent heat, sensible heat, and momentum fluxes. Although forecasters can use real-time satellite observations and climatological data to predict TC intensity, this leaves room for significant error; error that is unsatisfactory when considering that forecasts and warnings are meant to save lives. Thus, subsurface measurements are paramount to improving forecasting efforts, which will keep the

public more informed and ultimately, safer [57, 58, 62, 63].

In order to provide the three-dimensional observations key to initializing coupled numerical prediction models for more accurate intensity forecasts, profiling floats and gliders have been strategic deployed ahead of storms to survey upper ocean temperature and salinity structure [46, 64]. In a similar manner, Sanabia et al. (2013) [57] demonstrated how the real-time delivery of upper ocean temperature profiles to coupled numerical prediction models significantly improved TC track and intensity forecasts. These studies built a framework to produce more credible TC intensity forecasts by strategically deploying ALPS along TC tracks, which assimilated upper ocean data in real-time; thus, better constraining coupled numerical prediction models in order to produce more accurate forecasts [42, 45]. This study aims to provide more evidence in support of this notion.

4.3 Increased Usage of Autonomous Platforms

Post-storm analyses rely on ALPS to investigate how storm passage affected upper ocean as there are no other observational capabilities readily available. Storms are a primary source of momentum, sensible heat, and moisture fluxes across the air-sea interface, and as previously discussed, they input anomalous near-inertial and kinetic energy into the upper ocean; signals of each mode of modulation are distinguishable thanks to the high resolution and persistent sampling of ALPS. Without the widespread use of ALPS, exploring the evolution of upper ocean dynamics is a challenging problem [43, 44, 58]. However, the capabilities of next-generation autonomous platforms, led by the Air-Launched Autonomous Micro Observer profiling float (ALAMO; [46, 65]), are rapidly advancing the understanding of air-sea interaction before, during, and after the passage of storms [42, 45, 52].

Observations from targeted ALAMO deployments ahead of Hurricanes Irma (2017) and Florence (2018) revealed a laterally expansive, near-uniform depth of TC-induced turbulence that mixed the surface layer and propagation of NIWs, identifiable by a heaving mixed layer base [58]. Observations from another targeted deployment ahead

of Hurricane Ignacio (2021) highlighted a rapid depression of the thermocline, followed by NIW propagation, turbulent mixing, and subsequent upper ocean cooling in the wake of the storm [46].

After a TC or ETC passes through a region, the surface and upper ocean cools, often described as a "cold wake." This phenomena has been well captured and documented using satellite-borne SST observations, and more recently by ALAMO during TCs Hilda, Ignacio, Oho, and Olaf (2015); Irma (2017); Florence (2018); Teddy (2020); Ida (2021); Ian (2022); and in Chapter 6, evidence will be provided in the case of ETC Epsilon, as well. This phenomena occurs due entrainment of cold subsurface water into the mixed layer as a result of TC-induced, enhanced upwelling and breaking of NIWs [58, 66, 67]. This mode of mixing dominates upper ocean dynamics during the storm, and can slowly communicate energy into the ocean interior during and after the passage of the storm [16]. Further, this mechanism depletes the local thermal energy budget; such that stalling storms may weaken due to decreased enthalpy flux [68, 69]. Or, even subsequent storms propagating through that same region could struggle to intensify or perhaps dissipate altogether as a result [70, 71, 72]. Important components of these processes are poorly understood, due in part to infrequent observations of parameters critical to these air-sea interactions. However, the widespread and increased usage of ALPS is filling that void.

Chapter 5

2020 NISKINe Deployment

5.1 Extratropical Cyclone Epsilon

Epsilon was a late-season, category-3 TC that originated from a trough that pinched off from a synoptic-scale, upper-level flow [5]. The trough, and its associated low pressure, interacted with a surface trough on 16 October; thus, classifying the formation of Epsilon as non-tropical. The coupling of these two features produced isolated deep moist convection; hence, initiating cyclogenesis [5]. By 1200 UTC 16 October, forecasters observed maturing low-level cyclonic vorticity, which led to the vertical stacking of the upper-level cutoff low and the surface trough. Thereafter, the two low pressure systems remained coupled, but only moderate convective activity ensued. The systems propagated equatorward over SSTs of 27°C, which enhanced convective activity. By 0600 UTC 19 October, satellite observations showed that the low had sufficiently developed and organized into large convective cloud clusters approximately 1300 km east of Bermuda. Subsequently, forecasters classified the system as Tropical Depression 27 (Figure 5-1; [5]). By 1200 UTC, the storm strengthened to TS-intensity and was therefore reclassified and officially named TS Epsilon [5].

On 21 October, vertical wind shear and dry air intrusions that previously inhibited further development subsided. As such, the storm sufficiently organized and an identifiable center of circulation emerged. By 1800 UTC, TS Epsilon underwent rapid intensification and was reclassified as a 100-kt, category-3 TC, while it was

approximately located 555 km southeast of Bermuda (Figure 5-1; [5]). At this time, forecasters observed a small radius of maximum winds, but an enormous TS-wind radius of over 500 km; hinting that as the storm developed it would grow increasingly more expansive. Of note, the storm is believed to be the farthest-east major TC to form after 20 October by 24° latitude. The previous record was held by TC Wilma (2005) after it gained TC-status at 80.3°W on 25 October [5, 73].

On 24 October, TC Epsilon interacted with another upper-level trough, causing it to accelerate northeast as it became embedded in the mid-latitude flow. By 25 October, the storm grew elongated across the North Atlantic due to a deepening extratropical low borne off the coast of Nova Scotia. This baroclinic influence contributed to further expanding the wind field (Figure 5-2). At 1800 UTC 25 October, the TC Epsilon weakened as it moved north of the warm waters of the Gulf Stream and was reclassified to TS-status (Figure 5-1; [5]). At 0600 UTC 26 October, the storm underwent extratropical transition and was reclassified as ETC Epsilon, while located approximately 900 km east of Cape Race, Newfoundland (Figures 5-1, 5-3, and 5-4; [5]).

In its final Epsilon-advisory, published at 1800 UTC 26 October, NHC noted that the storm would remain very dangerous and predicted that it would maintain its track and intensity deep into the subpolar North Atlantic [5]. The aforementioned deepening extratropical low underwent rapid intensification and absorbed ETC Epsilon by 1800 UTC 26 October (Figures 5-3 and 5-4). As predicted, the merged storm continued into the far subpolar North Atlantic, where it approached the NISKINe observational array. Remnants of ETC Epsilon were identifiable via satellite imagery through the 1800 UTC 29 October NWS/NCEP OPC forecast (Figure 5-4).

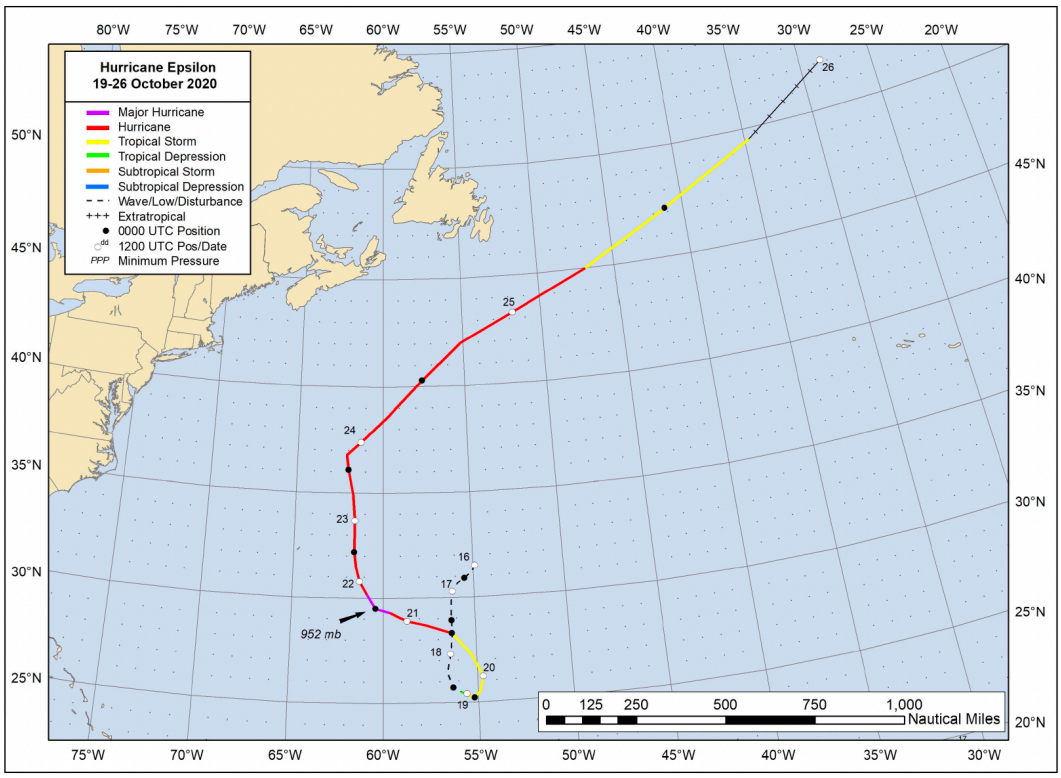

Figure 5-1: Best track positions for TC/ETC Epsilon from 1200 UTC 16 October to 1200 UTC 26 October. Figure from Papin (2020) [5].

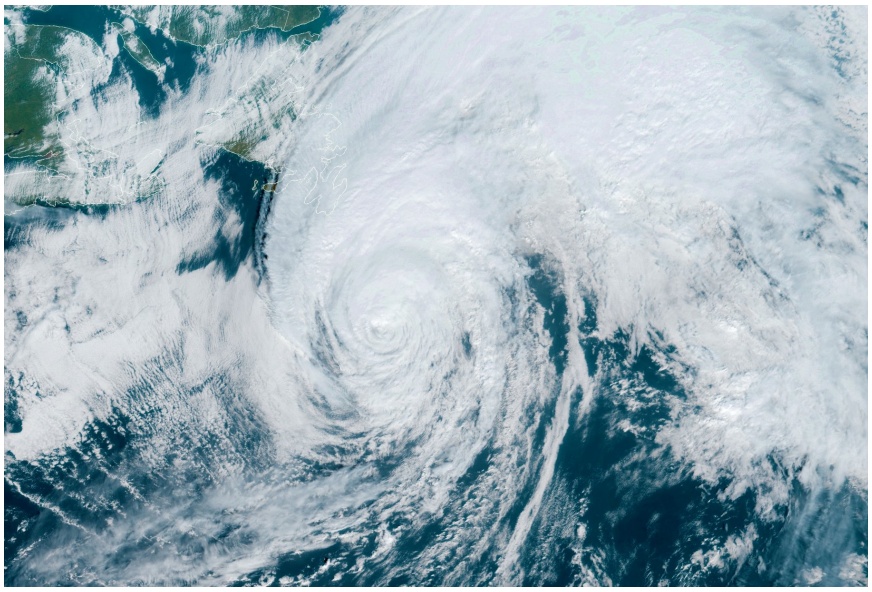

Figure 5-2: TC Epsilon, as viewed by GOES-16 at 1500 UTC 25 October, while located approximately 395 km southeast of Cape Race, Newfoundland. The storm would be reclassified as ETC Epsilon 15 hours later. Satellite image courtesy of NOAA.

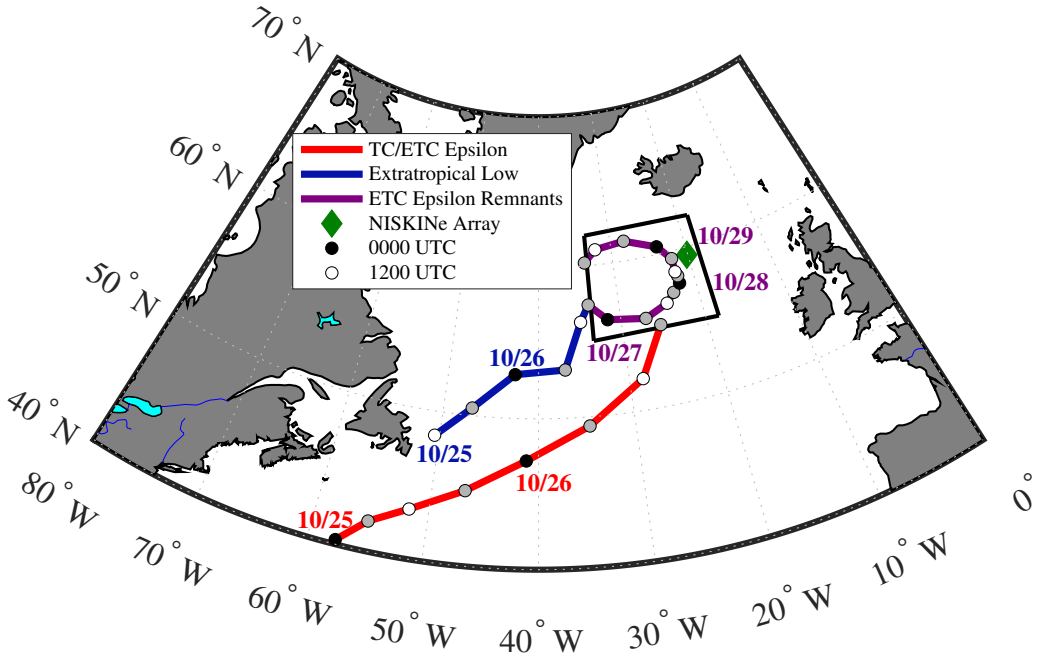

Figure 5-3: TC/ETC Epsilon (red), Extratropical Low (dark blue), and Remnants of ETC Epsilon (purple) best track positions from 0000 UTC 25 October to 1800 UTC 29 October. The approximate position of the NISKINe observational array (green diamond) is shown. The black box represents the focused observational area highlighted in Figure 5-5.

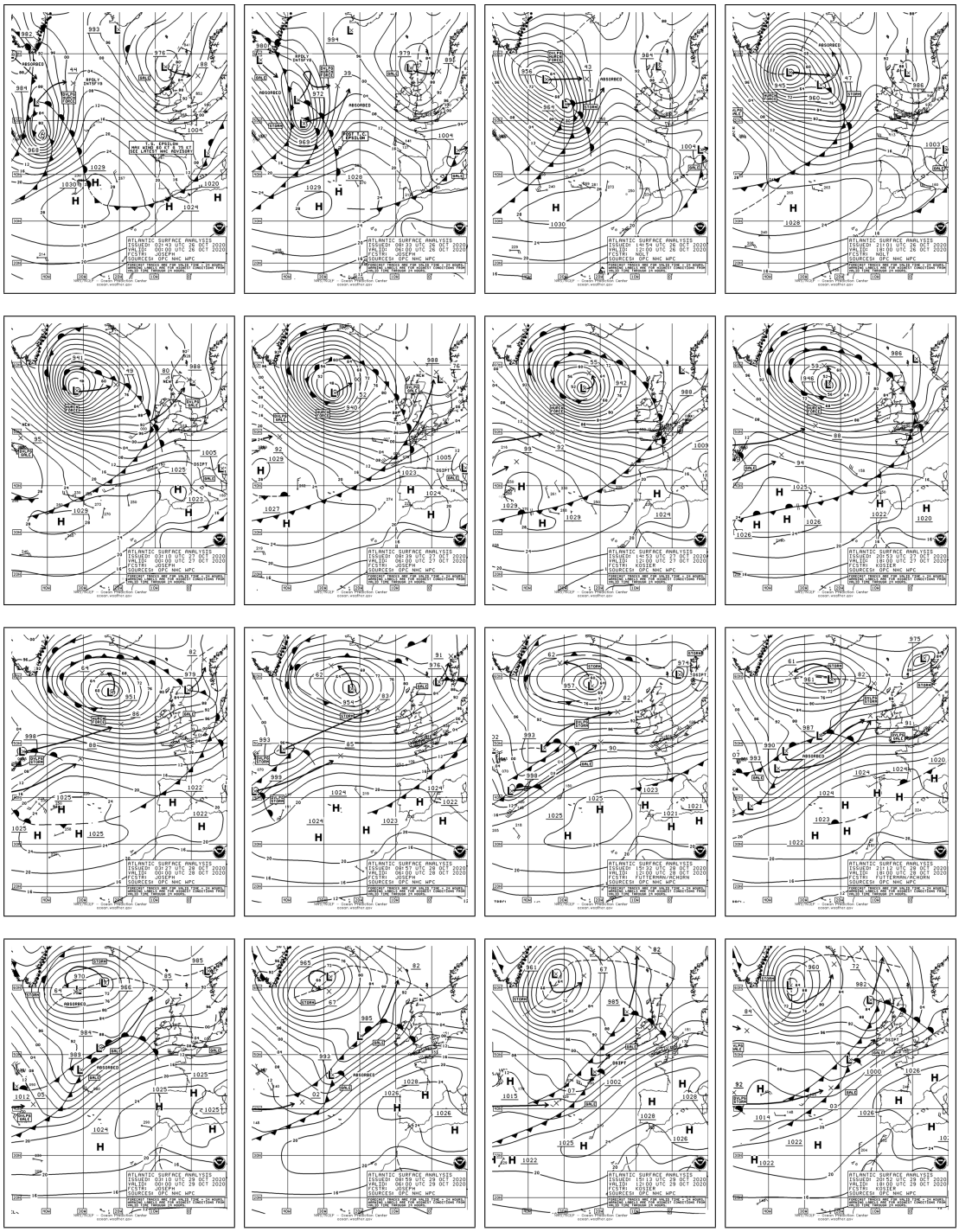

Figure 5-4: Atlantic surface analyses every six hours from 0000 UTC 26 October to 1800 UTC 29 October, hindcasting the surface conditions. The center of circulation of ETC Epsilon and its remnants are marked with an "X," coinciding with the "L" that delineates a local pressure minimum. Images courtesy of NWS/NCEP OPC.

5.2 Scientific Design

The NISKINe observational array was deployed on 04 October from the R/V *Armstrong* into an anticyclonic eddy, south of Iceland, at approximately 58.4°N, 21.5°W (Figures 5-3 and 5-5). All four autonomous instruments were deployed in rapid succession, with the intention of using the enhanced vorticity field of the eddy to keep the instruments in close proximity of each other throughout the experimental period. Of note, the deployment location was chosen because the anticyclone referenced above is quasi-permanent. This feature has been named the "PRIME Eddy" by previous observers (Figure 5-6; [74, 75]). This deployment strategy was designed to facilitate the contemporaneous collection of surface and subsurface ocean data of the subpolar North Atlantic over inertial and intraseasonal timescales.

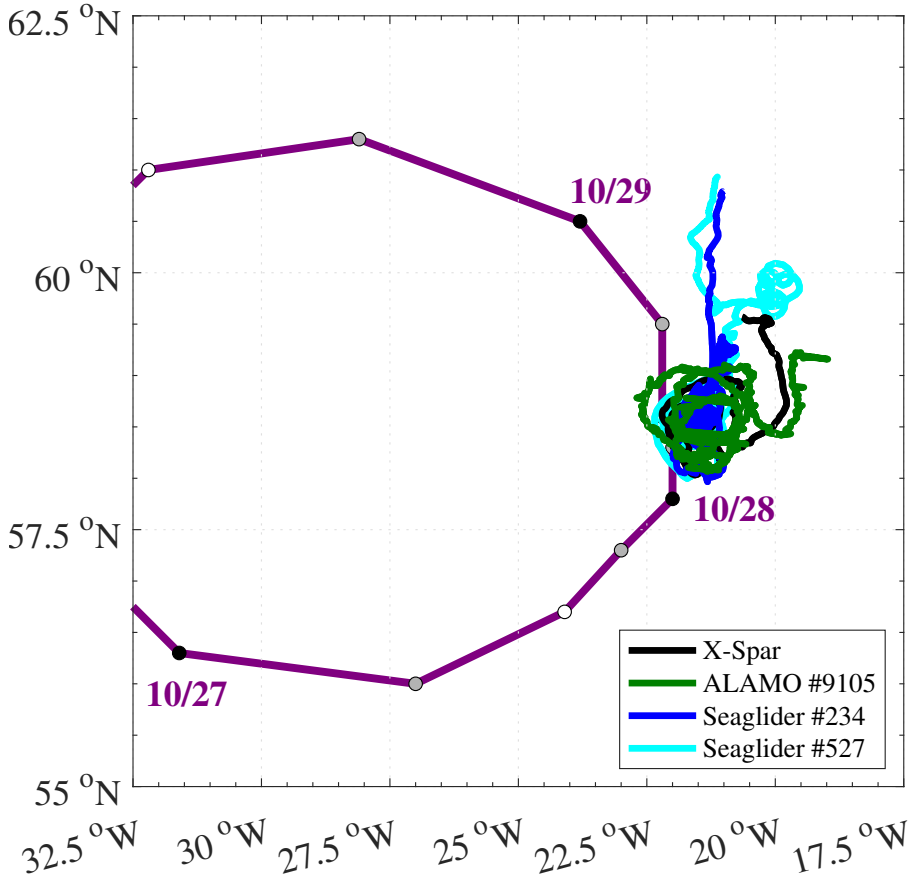

Figure 5-5: Remnants of ETC Epsilon (purple) directly interacted with the NISKINe observational array from 1200 UTC 27 October to 1200 UTC 29 October. The trajectories of each platform of the array are colored: X-Spar (black), ALAMO #9105 (green), Seaglider #234 (blue), and Seaglider #527 (cyan).

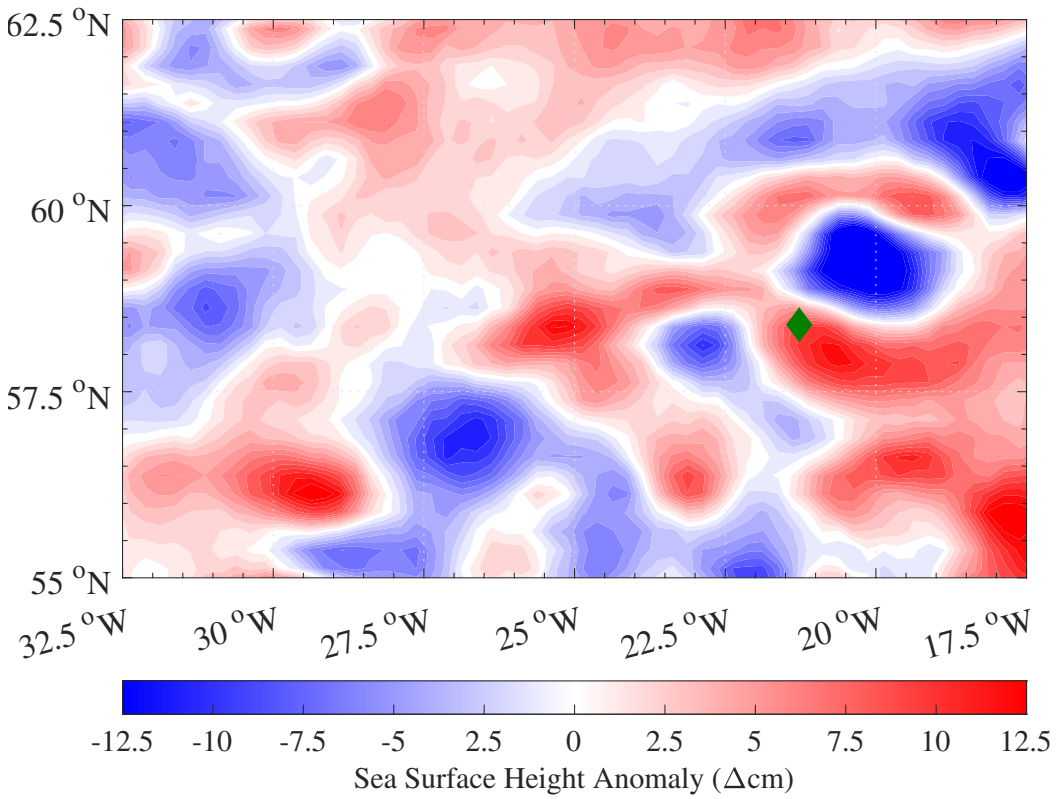

Figure 5-6: Sea surface height anomaly (Δcm) derived from NOAA satellite altimetry data showing the anticyclonic PRIME eddy, the chosen deployment location for the NISKINe observational array (green diamond).

5.2.1 eXpendable Spar Buoy

The eXpendable Spar buoy (X-Spar; [76]) is a recently developed freely-drifting platform designed and equipped to investigate air-sea interaction and upper ocean response to atmospheric forcing (Figure 5-7). X-Spar supports a variety of sensors above and below the ocean surface including those required to make direct measurements of momentum and buoyancy fluxes across the air-sea interface. The Direct Covariance Flux System (DCFS; [77]) estimates turbulent momentum and buoyancy fluxes as well as measures bulk wind speed and direction. The X-Spar is further enhanced with a suite of scalar atmospheric sensors and radiometers. This surface sensing suite represents the latest version of the autonomous atmospheric turbulent flux package deployed during the Climate and Ocean Variability, Predictability, and Change (CLIVAR) Mode Water Dynamics Experiment (CLIMODE; [18]), the Salinity

Processes in the Upper Ocean Regional Study (SPURS; [78]), the Ocean Observatories Initiative (OOI; [79]), and the Tropical Pacific Observing System (TPOS; [80]) project. The design of X-Spar is motivated by successful deployments of the Air-Sea Interaction Spar (ASIS; [81]), specifically during winter Gulf Stream drifts in support of CLIMODE [82].

Below the air-sea interface, X-Spar is capable of sampling the surface wave field using subsurface pressure sensors in conjunction with an inertial measurement unit, and the near-surface stratification using an array of temperature and salinity instruments. The small cross-sectional area and sensor placement 7-m above the air-sea interface induces minimal flow distortion and relative insensitivity to high frequency waves such as those produced in the storm environment [76]. As such, the raw atmospheric data observed by X-Spar is of higher quality than that which can be obtained from ships, autonomous surface vessels such as wave gliders, or traditional buoys. Importantly, X-Spar rapidly samples the air-sea interface on the order of once every ten minutes. Thus, high frequency atmospheric-ocean coupling data is readily observed without the need for fixed buoys or extensive time on station for research vessels. A unique capability of X-Spar is its ability to process, compute, and telemeter this high frequency data in near-real time, which means X-Spar does not need to be recovered to collect the desired measurements; hence the "X" for expendable [76].

During the 2020 NISKINe deployment, X-Spar observed meteorological, SST, and wave data. More specifically, wind speed, direction, and stress; surface and subsurface pressure; air-sea exchange rates of buoyancy and momentum; surface radiative fluxes; and estimates of SWH were all telemetered. Although X-Spar survived its encounter with the remnants of ETC Epsilon, after 45 days of operation, a system failure terminated data transmissions on 17 November. In the spring, a Icelandic fishing vessel came across X-Spar and reported to authorities. Subsequently, the instrument was deemed a hazard to navigation and was recovered by the Icelandic Coast Guard on 24 March [76].

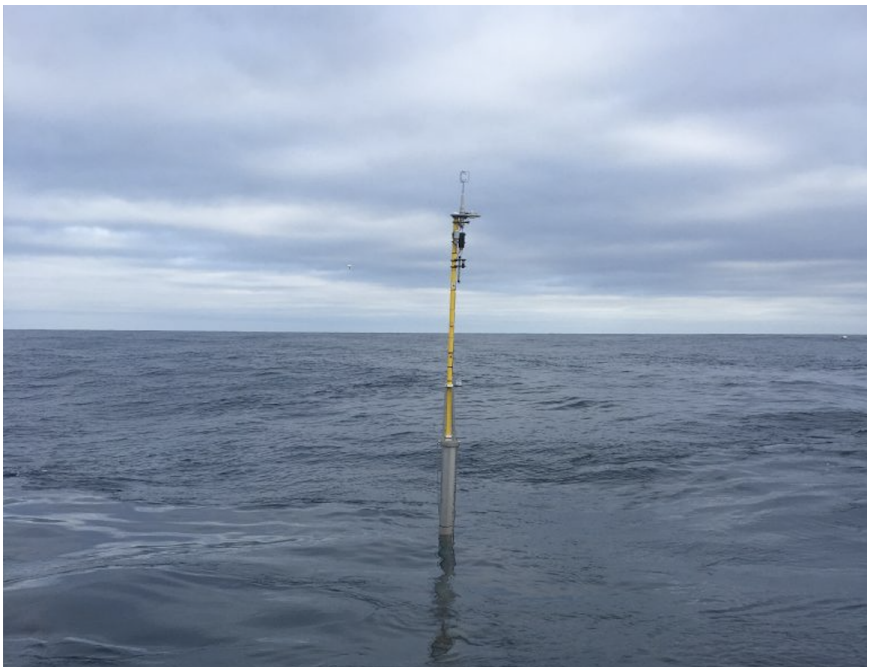

Figure 5-7: X-Spar drifting shortly after its deployment on 04 October 2020.

5.2.2 Air-Launched Autonomous Micro Observer

The need for improved observational assets to observe the upper ocean during TCs and ETCs was made evident by the significant societal and economic caused by the poorly intensity-forecasted Superstorm Sandy. In response, ALAMO was initially developed with funding from the National Oceanic and Atmospheric Administration (NOAA) under the Disaster Relief Appropriations Act of 2013, more commonly referred to as the Sandy Supplemental bill [46]. ALAMO was developed to meet the objective of a producing a rapdily deployable, persistent, subsurface ocean profiler capable of supporting operational storm reconnaissance missions. In doing so, ALAMO would replace the aging Airborne eXpendable BathyThermograph (AXBT), which is only capable of one profile and requires communication via VHF signal to the deploying aircraft.

ALAMO is a small profiling float which was originally designed to be launched from aircraft equipped with an "A-sized" sonobuoy launch tube, which is defined by MIL-S-81478C as 123.82 mm in diameter, an overall length of 914.39 mm, and a total package not exceeding 9 kg to include the air-deployment rigging and parachute

[46, 65]. Its diminutive engineering is the most recent iteration in the long progression of profiling float design [83]. After deployment, whether it be by air or other means, ALAMO provides observations of temperature and salinity structure in the upper ocean. This instrument can persistently monitor the upper ocean over many months, and depending on duty cycling it can last over a year. The most enduring floats to date were #9061, which traversed 292 km over the course of 645 vertical profiles, and #9023, which profiled for 415 days [65]. ALAMO communicates via a two-way Iridium transceiver, which allows for reprogramming of profiling frequency and maximum depth to tailor toward observational needs.

ALAMOs were initially test-deployed by the Air-deployed Profiling Instruments Group at Woods Hole Oceanographic Institution (WHOI) in collaboration with the Training and Research in Oceanic and Atmospheric Processes in Tropical Cyclones (TROPIC) program [57]. TROPIC had established a relationship with the United States Air Force Reserve 53rd Weather Reconnaissance Squadron - the "Hurricane Hunters" to deploy AXBTs on tasked storm reconnaissance missions [57]. After considerable cross-organizational effort and testing, it was determined that the WC-130J Hercules aircraft could support ALAMO deployments, given the similar weight and dimensions as the AXBT. ALAMO has continued to be deployed during operational storm reconnaissance missions, as highlighted in Jayne and Bouge (2017) [65], Sanabia and Jayne (2020) [58], and Jayne et al. (2022) [46]). As such, ALAMO, as well as other ALPS like surface drifters and gliders, is leading the way to provide a better understanding of air-sea interaction as it pertains to storm activity. The combination of high spatial and temporal resolution, sampling endurance, and the real-time data delivery have proven ALPS as a valuable contributor to the TC-prediction community [42, 64]. Using the same approaches and capabilities, their utility for investigating the dynamical effects of storm passage was explored during this study.

During the 2020 NISKINe deployment, ALAMO #9105 was programmed to rapidly profile to 200 dbar (1 dbar $\sim$ 1 m) at an interval of approximately two hours. In addition to a conductivity-temperature-depth sensor (CTD) to measure how temperature and salinity varied with depth, ALAMO #9105 was also equipped with a Wave In-

ertial Measurement Sensor (WIMS), one of the first of its test deployments of this technology. WIMS is a compact, low-power 9-axis inertial sensing device designed for use onboard ALAMO to capture the directional properties of surface gravity waves. Due to the limitations of satellite telemetry bandwidth, WIMS performs onboard orientation estimation, digital signal processing, and spectral analysis. At each surfacing, select co- and quadrature-power spectral densities are averaged across several segments of a ten minute sample window and transmitted by the instrument. These spectra can then be used to derive characteristics of the wave field, including SWH, period, and azimuthal direction. These combined capabilities of ALAMO were leveraged to evaluate the evolution of the upper ocean before, during, and after the passage of ETC Epsilon.

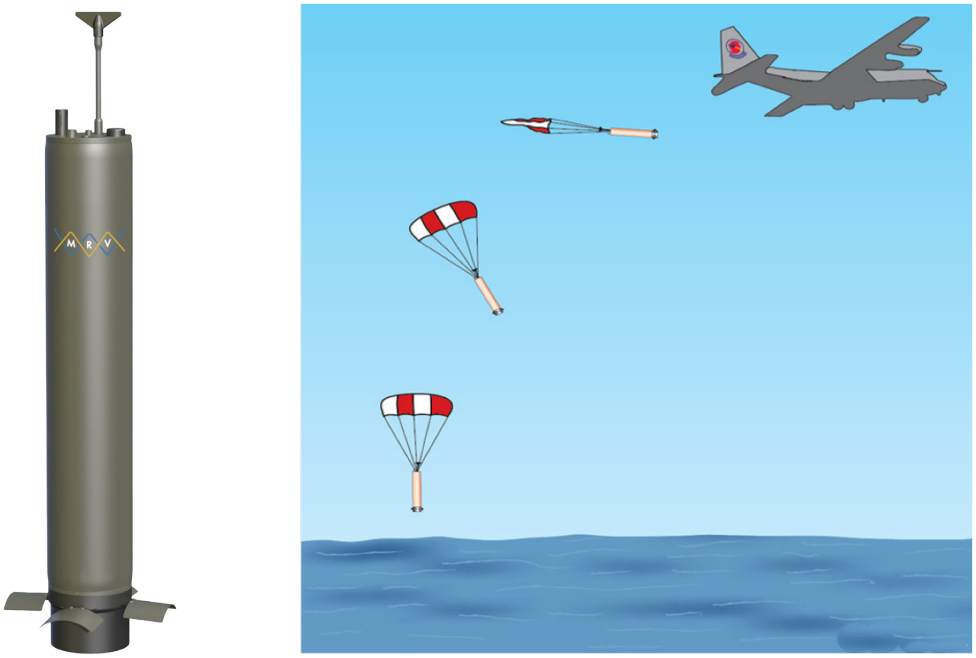

Figure 5-8: Left: Designed and manufactured by MRV Systems in collaboration with the Air-deployed Profiling Instruments Group at WHOI, ALAMO is comprised of an anodized aluminum tube; temperature, salinity, and pressure sensors, as well as a merged GPS-Iridium antenna attached to the top cap; a dual-chambered internal bladder and hydraulic pump to drive upward and downward motion; and stability fins to dampen motion when the float is surfaced. Right: Cartoon rendering of ALAMO being deployed from a WC-130J Hercules aircraft.

5.2.3 Seagliders

Gliders are buoyancy-driven, reusable, long-range autonomous underwater vehicles designed to glide up and down in the ocean and collect profiles of temperature, salinity, current velocities, and other ocean parameters [84]. They are uniquely maneuverable as they steer through the water by autonomously controlling attitude, and can thus execute desired survey patterns. Gliders surface at the end of every dive cycle, at which point they can download new commands and upload data via Iridium telemetry in a similar manner as ALAMO [85, 86]. Given that gliders horizontally propel themselves, they can be strategically positioned ahead of and hold their positions before, during, and after the passage of storms [44]. Gliders have been successfully deployed to improve understanding of upper ocean temperature and salinity stratification and mixing processes in relation to storm activity [64, 87].

Seaglider is a family of glider developed by the Integrative Observational Platforms (IOP) group at the University of Washington, Applied Physics Laboratory (UW-APL) (Figure 5-9; [85]). Two Seagliders, #234 and #527, were deployed during the 2020 NISKINe deployment to provide spatial coverage around X-Spar and compliment ALAMO. Each instrument measured temperature, salinity, pressure, horizontal current velocity, dissolved oxygen, and optics. Current velocities were measured directly using a Nortek Signature 1000 ADCP specifically designed for Seagliders. Each Seaglider collected ADCP data both on the descent and climb of each profile, with 15 bins and a cell size of 2 meters recorded every 15 seconds. The processing for the Seaglider ADCP follows the steps described in Todd et al. (2017) [88], which is based on lowered-ADCP processing [89] and subsequent developments [90, 91]. Initially, both Seagliders were programmed to execute regular patterns around X-Spar, but the buoy was moving too fast. Instead, the Seaglider operations were changed such that Seaglider #234 shadowed X-Spar, while Seaglider #527 executed north to south surveys across the observational area.

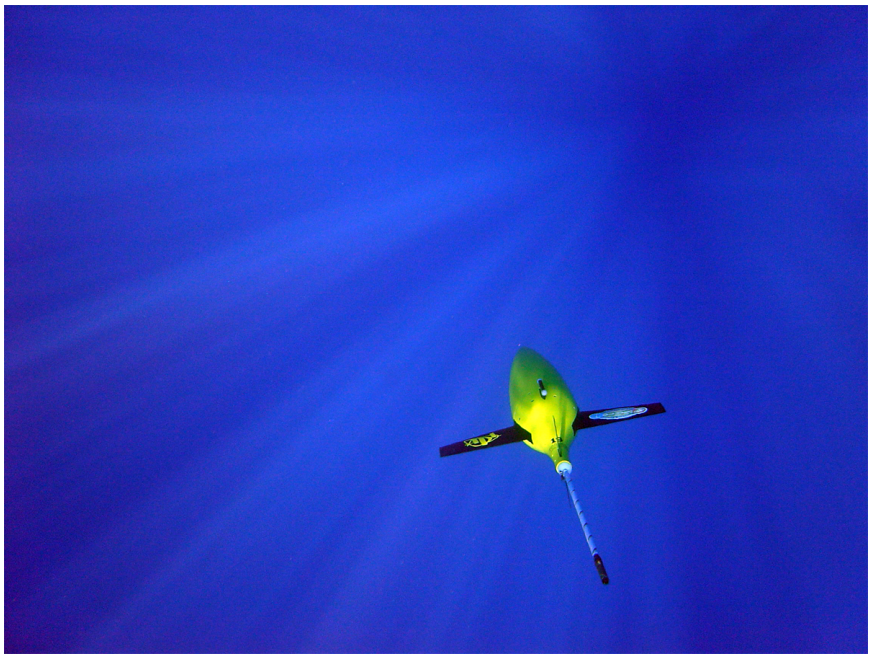

Figure 5-9: Seaglider executing a dive cycle, which extends from the surface to as deep as 1,000 dbar. Endurance of these vehicles largely depends on ocean stratification and programmed profile depth, but a nominal lifespan is over nine months.

5.3 Demonstration of Utility

Given the inherent overlap of sensing capabilities within the observational array, oceanic and atmospheric characteristics were contemporaneously observed by three different autonomous platforms. As of the deployment date, no specific synoptic-scale activity was targeted. The goal was to leverage the observational array to observe how strong forcing events, such as deep fall lows, would affect upper ocean structure on near-inertial to intraseasonal time scales. Fortuitously, approximately three weeks after the deployment, the NISKINe observational array was overrun by remnants of ETC Epsilon from 1200 UTC 27 October to 1200 UTC 29 October (Figure 5-5). Although the formation of ETC Epsilon and the propagation of its remnants far into the subpolar North Atlantic was unforeseen, the data collected by the NISKINe observational array provided an excellent opportunity to explore the upper ocean response, not only to a strong forcing event, but to the passage of a fully transitioned and formally named ETC.

Throughout the storm passage period, the assets were all within 52.2 km of each other and at least 650.4 km from the storm. The closest point of approach between the NISKINe observational array and the storm occurred at 1200 UTC 28 October, when each asset was within 51.0 km from the center of circulation: X-Spar: 7.9 km; ALAMO #9105: 51.0 km; Seaglider #234: 39.5 km; and Seaglider #527: 50.5 km (Figure 5-5 and Table 5.1). Evidence of ETC Epsilon-induced forcing was captured by the NISKINe observational array through at least 03 November, while remnants of the storm were no longer recognizable on satellite imagery after 1800 UTC 29 October (Figure 5-4).

Table 5.1: Distance (km) between each instrument in the NISKINe observational array and the center of circulation of the remnants of ETC Epsilon from 1200 UTC 27 October to 1200 UTC 29 October. The closest point of approach for each instrument occurred at 1200 UTC 28 October (italicized).

Datetime (UTC)	**X-Spar**	**ALAMO**	**Seaglider #234**	**Seaglider #527**
1200 27 OCT	224.9	267.1	257.0	248.0
1800	143.5	188.2	169.5	166.4
0000 28 OCT	83.2	124.2	98.2	101.8
0600	37.8	73.5	49.1	57.9
1200	*7.9*	*51.0*	*39.5*	*50.5*
1800	88.8	65.2	98.2	85.0
0000 29 OCT	219.1	210.2	242.3	225.4
0600	443.9	429.3	469.2	460.0
1200	627.3	649.8	650.4	647.9

Chapter 6

Surface Ocean Observations

6.1 Surface Pressure

X-Spar recorded a deep depression in surface pressure as the remnants of ETC Epsilon approached the NISKINe observational array: 1015 mb at 2310 UTC 20 October; a dip below 960 mb on 23 and 24 October, due to an deep fall low forming off the coast of Ireland; a rebound to 999 mb by 0410 UTC 26 October as that system dissipated; and then a rapid deepening to 937 mb at 2310 UTC 26 October just before storm passage, the lowest of the entire X-Spar record (Figures 6-1 and 6-2). X-Spar captured the sustained low pressure during the passage period nicely, as well, with measurements ranging from 981 to 938 mb (Figure 6-2). Observations indicate that the storm rapidly deepened shortly into the passage period and retested the 937 mb minimum from the previous day. At 1510 UTC 27 October X-Spar observed this deepening and reported a secondary minimum surface pressure of 938 mb (Figures 6-1 and 6-2). The 48-hour surface forecast, issued at 1724 UTC 25 October, valid for 1200 UTC 27 October, predicted that surface pressure would fluctuate between 940 and 956 mb in the vicinity of X-Spar at that time (Figure 6-3). X-Spar data shows that this was a slight underestimate and that the storm was deeper than forecasted by the NWS/NCEP OPC coupled numerical prediction models.

While more apparent in the observations discussed in Section 6.2, X-Spar captured the passage of the center circulation of the storm at 1140 UTC 28 October, reading 961

mb (Figures 6-1 and 6-2). Although it did not co-locate with the minimum surface pressure reading, this observation is still valid given that the storm was becoming increasingly disorganized at that time. As the remnants of ETC Epsilon continued to dissipate, the surface pressure slowly built. At 0440 UTC 31 October, X-Spar recorded 990 mb, indicating that surface pressure had climbed approximately 50 mb since the the beginning of the passage period. However, another rapid deepening occurred on 31 October and lasted until the morning of 01 November. It concluded with a 958 mb reading at 0410 UTC (Figures 6-1 and 6-2). It stands to reason that the remnants of ETC Epsilon could have been at play here, but, more likely, the chief contributor of this event was a second deep fall low that was passing by in close proximity to the eastern flank of the NISKINe observational array. By 2110 UTC 02 November, surface pressure crossed 1000 mb (Figures 6-1 and 6-2), and the remnants of ETC Epsilon had been no longer identifiable on satellite imagery for two days. This marked the end of the Epsilon-induced modulation of the surface pressure field.

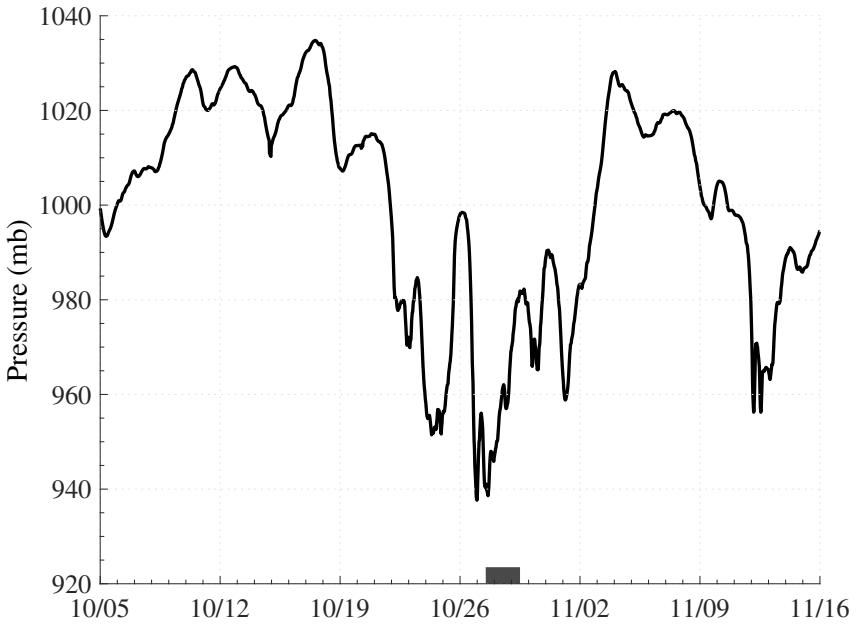

Figure 6-1: Time series of surface pressure (mb) observations from X-Spar before, during (gray rectangle), and after the passage of the remnants of ETC Epsilon.

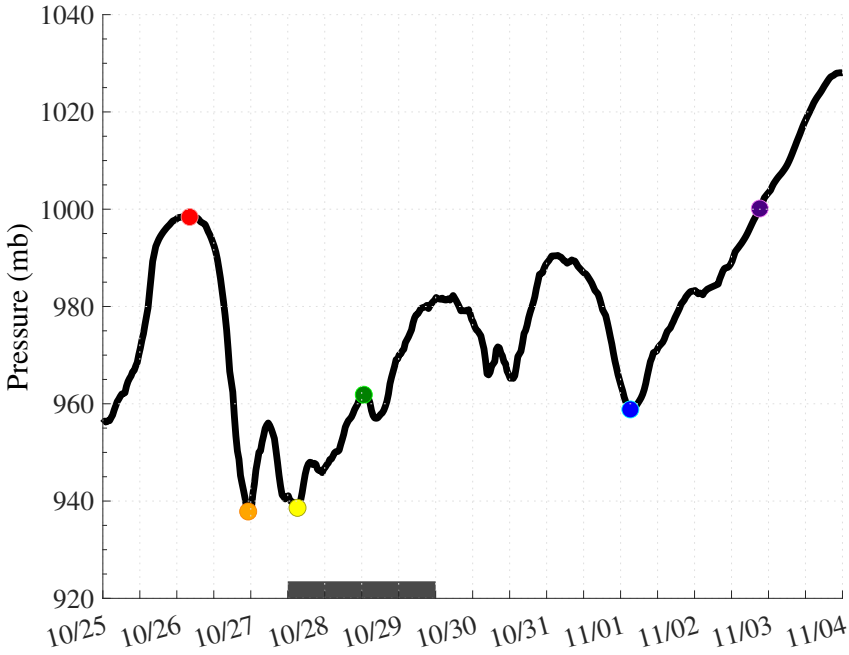

Figure 6-2: As Figure 6-1, but from 0000 UTC 25 October to 0000 UTC 04 November, highlighting the passage period to resolve the approach of the storm (red to orange circles), the surface pressure minimums (orange and yellow circles), the passage of the center of circulation (green circle), the formation of another deep fall low (blue circle), and the definitive conclusion of Epsilon-induced modulation (purple circle).

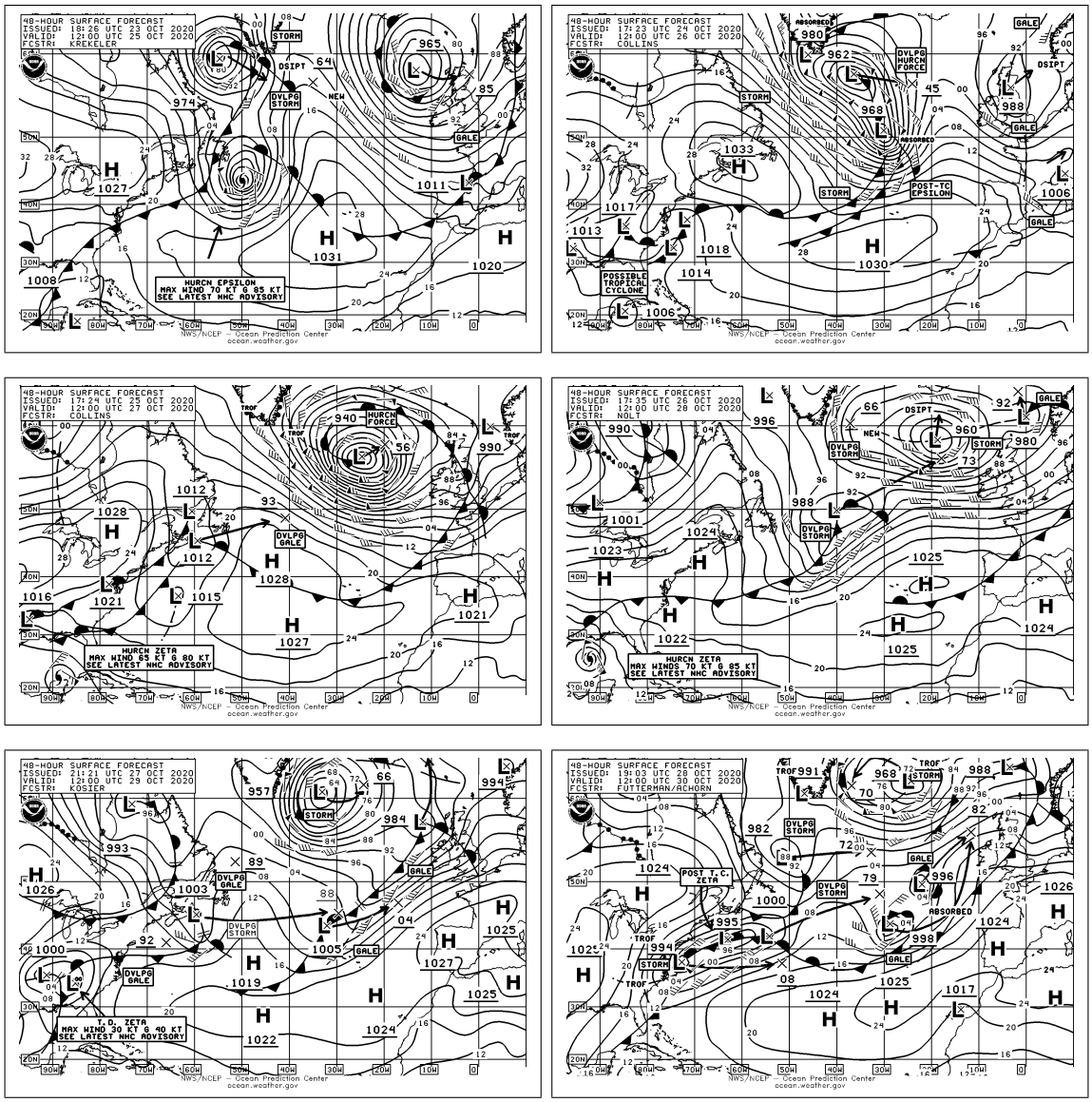

Figure 6-3: 48-hour surface forecasts every 24 hours from 1200 UTC 25 October to 1200 UTC 30 October, predicting North Atlantic surface conditions. Images courtesy of NWS/NCEP OPC.

The ALAMO and Seaglider CTDs include a pressure transducer to derive depth, which were leveraged to estimate a surface pressure anomaly. Such a calculations were possible because when surfaced, both platforms sample a pressure time series to correct their respective profiles for atmospheric pressure offset. While these anomalies are not suitably accurate for measurement of absolute atmospheric pressure, the effects of the passage of the remnants of ETC Epsilon are apparent. Most importantly, they are promisingly congruent with the direct measurements from X-Spar (Figures 6-4 and 6-5).

The deep depression of surface pressure was well captured using this method. At 2316 UTC 25 October, ALAMO #9105 recorded a surface pressure anomaly of -6 Δmb, which decreased to -65 Δmb by 0218 UTC 27 October (Figures 6-4 and 6-5). The sustained low pressure during the passage period was also adequately detailed, ranging from -53 Δmb at 1133 UTC 27 October to a -29 Δmb at 1249 UTC 29 October. ALAMO #9105 surfaced at 0206 UTC 01 November and observed the rapid deepening as the remnants of ETC Epsilon dissipated, -51 Δmb was recorded. At 0955 03 November, a -1 Δmb measurements indicated that the anomalous low pressure due to the passage of the remnants of ETC Epsilon had concluded (Figures 6-4 and 6-5).

Similar surface pressure anomalies were calculated from the Seaglider data, although a slightly different methodology was used. The Seaglider surface pressure anomalies were approximated as a water depth offset, where the total range in pressure associated with the passage of the storm ($\sim$100 mb) corresponded to about 1 m when expressed in this manner. While the magnitudes of the Seaglider pressure anomalies slightly differ from those of ALAMO #9105, the trends in the time series are nearly exact (Figures 6-4 and 6-5). It is encouraging that X-Spar, ALAMO #9105, Seaglider #234, and Seaglider #527 were largely in good agreement, especially given the novel anomaly computations. It remains to be seen if and how these measurements could be of use to operational centers.

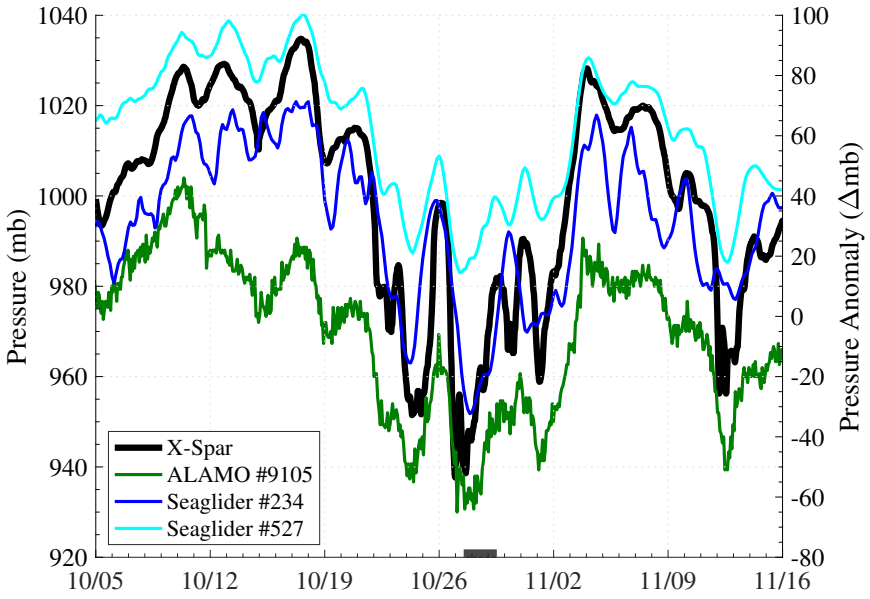

Figure 6-4: As Figure 6-1, but including ALAMO #9105 (green), Seaglider #234 (blue), and Seaglider #527 (cyan) surface pressure anomalies (Δmb).

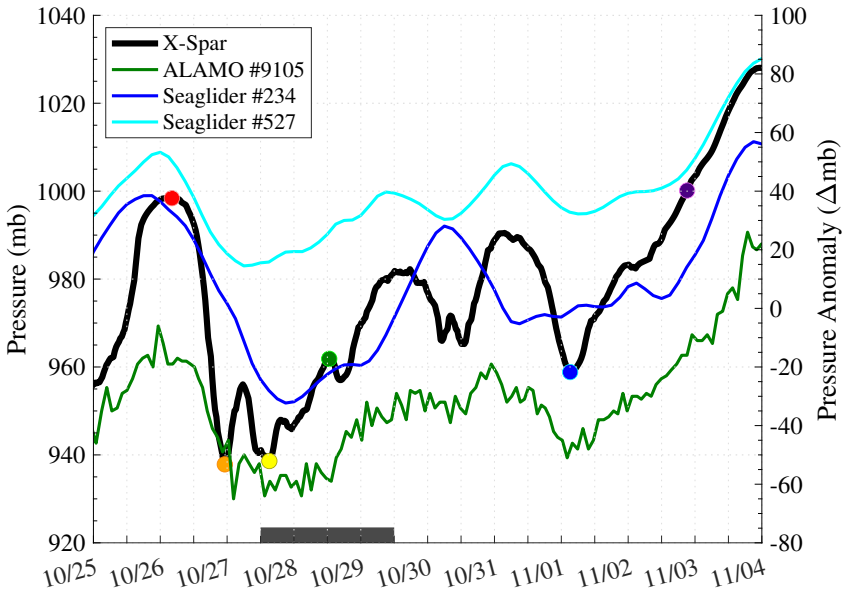

Figure 6-5: As Figure 6-2, but including ALAMO #9105 (green), Seaglider #234 (blue), and Seaglider #527 (cyan) surface pressure anomalies (Δmb).

6.2 Wind Speed and Direction

This first indication of the Epsilon-induced wind field in the vicinity of the NISK-INe observational array occurred at 1610 UTC 26 October when X-Spar measured 30.1 kt winds, marking the arrival of the first band of extreme winds (Figures 6-6 and 6-7). By 1710 UTC, X-Spar measured 34.2 kt, TS-level winds, which increased to 41.2 kt by 2310 UTC (Figures 6-7). At this time, the center of circulation of the storm was over 800 km southwest of X-Spar (Figures 5-3 and 6-3). This observation highlights the extraordinary expanse of the remnants of ETC Epsilon.

The first band of extreme winds concluded when a fine-scale cold front emerged just after 0000 UTC 27 October. At 0110 UTC, X-Spar recorded southeast (133°) winds blowing at 36.2 kt, but by 0140 UTC, south-southwest (194°) winds were blowing at just 17.7 kt. Then, by 0210 UTC, a west-southwest (244°) wind quickly increased to 31.0 kt (Figures 6-7 and 6-8). After the frontal boundary passed, winds regained near TS-intensity, and X-Spar observed the second and most sustained period of extreme winds. The maximum reading during this period was 36.9 kt at 1010 UTC 27 October and lasted until 0110 28 October when 30.5 kt winds were observed (Figure 6-7). Then, on the morning of 28 October, winds abruptly decreased, reaching a nadir of 3.6 kt at 1140 UTC 28 October; such calm winds that a wind vane would have been inactive and a human might not even perceived the breeze. X-Spar was detecting the passage of the center of circulation, which was also indicated by the change in wind direction from south (84°) at 1110 UTC 28 October increasing to north (353°) by 1140 UTC (Figures 6-7 and 6-8). The evolution of the wind direction at this time elucidates cyclonic spin. Thus, while satellite imagery hinted that only remnants of ETC Epsilon remained, X-Spar observations prove that it was still sufficiently organized to maintain its cyclonic vortex.

After the passage of the center of circulation, winds regained near TS-intensity, and shortly after 1540 UTC 28 October, X-Spar resolved the third band of extreme winds (Figure 6-7). This episode lasted briefly as winds fell below the 30-kt range by 2140 UTC. The NWS/NCEP OPC 48-hour surface forecast, issued at 0445 UTC

27 October, valid for 0000 UTC 29 October, predicted 35 to 40 kt southwest winds would blow in the vicinity of X-Spar (Figure 6-3). Data from X-Spar suggests that this forecast was an overestimate as it reported 25.8 kt winds as the third band of extreme winds had already subsided (Figure 6-7). Winds steadily decreased until 15.7 kt at 1810 UTC 29 October, before ramping back up to form the fourth and final band of extreme winds. This episode reached a peak intensity at 1210 UTC 30 October as X-Spar recorded 37.2 kt winds (Figures 6-7). As stated in Section 6.1, it is hard to discern how much the remnants of ETC Epsilon contributed to these winds as compared to the deep fall low that had formed; however, after approximately 1800 UTC 30 October ETC Epsilon-related wind signal certainly became indistinguishable (Figures 6-6 and 6-7).

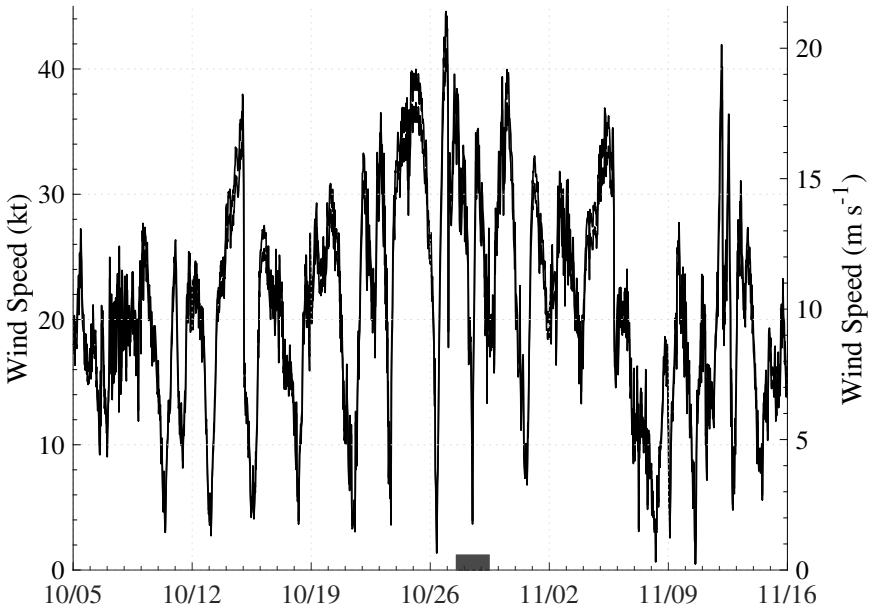

Figure 6-6: Time series of 7-m wind speed observations (corrected to 10 m) from X-Spar before, during (gray rectangle), and after the passage of the remnants of ETC Epsilon.

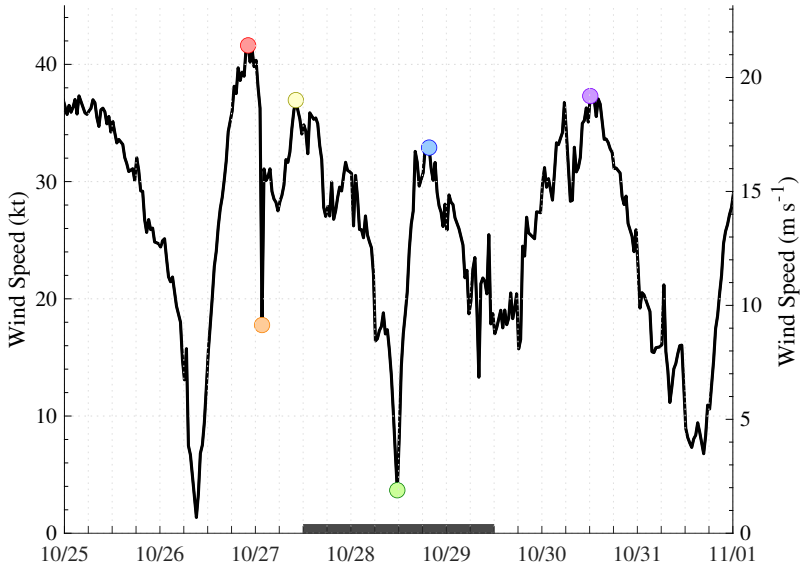

Figure 6-7: As Figure 6-6, but from 0000 UTC 25 October to 0000 UTC 01 November, highlighting the passage period to resolve all four bands of extreme winds (red, yellow, blue, and purple circles), a fine-scale cold front (orange circle), and the passage of the center of circulation (green circle).

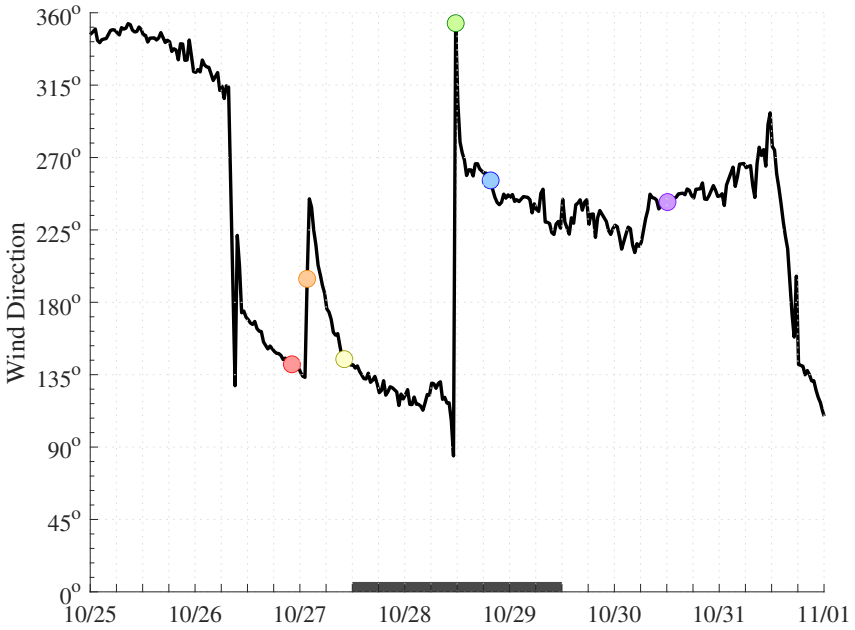

Figure 6-8: Time series of 7-m wind direction observations from X-Spar before, during (gray rectangle), and after the passage of the remnants of ETC Epsilon. The colored circles mark the same events as in Figure 6-7.

6.3 Total & Near-Inertial Wind Stress

X-Spar calculated direct covariance wind stress, which is a slightly less noisy representation of wind forcing in the storm environment. At 2210 UTC 26 October, during the arrival of the first band of extreme winds, X-Spar calculated a maximum wind stress of 1.32 N m^{-2}. The passage of the cold front at 0140 UTC 27 October was also well captured when wind stress fell to 0.12 N m^{-2} and then rapidly recovered into the second band of extreme winds. By 1010 UTC, the second band of extreme winds caused wind stress of 0.96 N m^{-2}. The data agrees with the passage of the center of circulation as it measured, remarkably, a wind stress 0.00 N m^{-2} at 1140 UTC 28 October. Wind stress then rebounded into the third and fourth bands of extreme winds, peaking at 0.69 N m^{-2} at 1940 UTC 28 October, and 1.01 N m^{-2} at 1210 UTC 30 October, respectively.

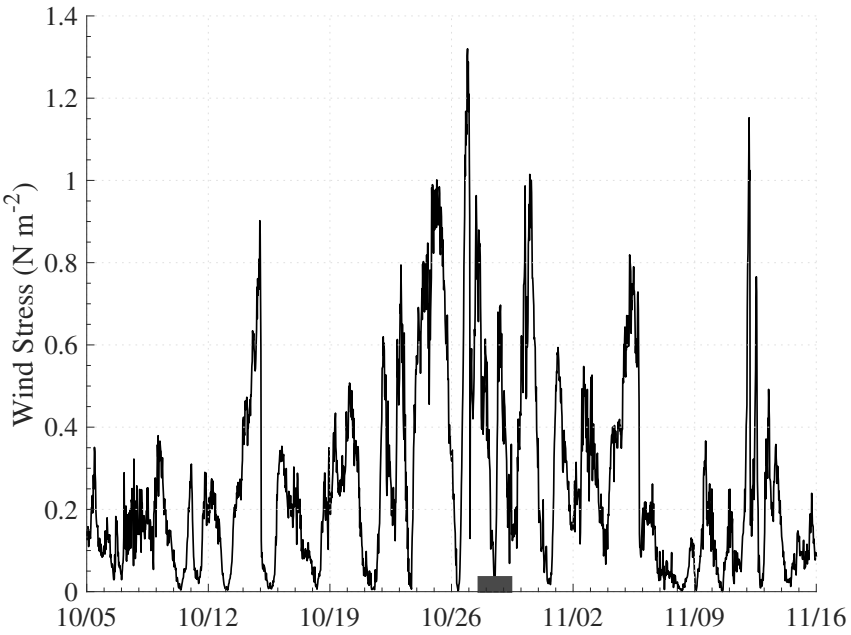

Figure 6-9: Time series of direct covariance wind stress (N m^{-2}) observations from X-Spar before, during (gray rectangle), and after the passage of the remnants of ETC Epsilon.

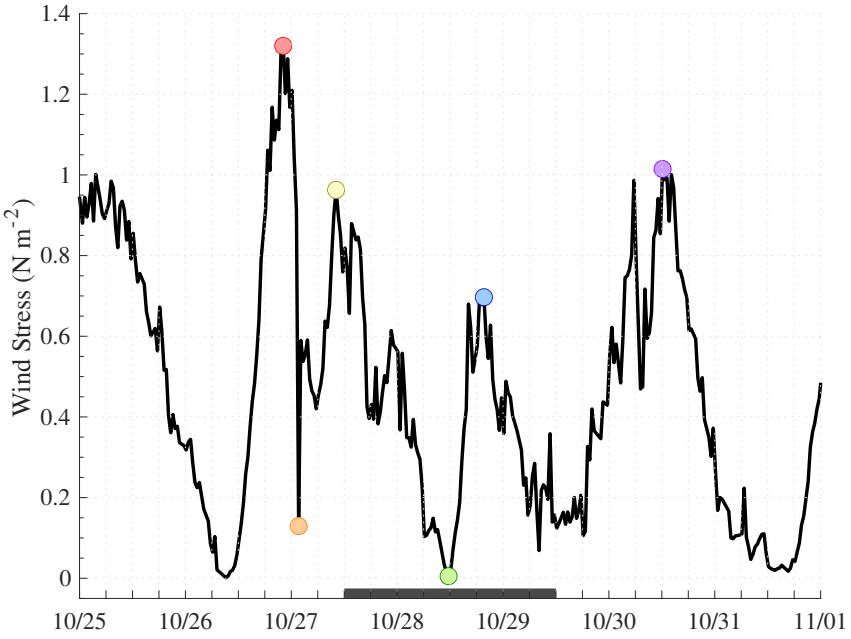

Figure 6-10: As Figure 6-9, but from 0000 UTC 25 October to 0000 UTC 01 November, highlighting the passage period. The colored circles mark the same events as in Figure 6-7.

According to the routine outlined by Silverthorne and Toole [6], an inertial bandpass filter was performed to extract near-inertial wind stress from the total direct covariance wind stress. The x-component and y-component of the total wind stress magnitude was bandpass filtered between 13.6 and 14.3 hours: the corresponding inertial periods to the minimum and maximum latitudinal positions of X-Spar during the observational period. The procedure returned a complex time series of the cyclonic and anticyclonic near-inertial signals, and after taking the absolute value of each, the amplitude of the near-inertial wind stress was derived and plotted (Figures 6-11 and 6-12).

The cyclonic and anticyclonic signals detail a major source of near-inertial energy as the remnants of ETC Epsilon approached the NISKINe observational array. Around 17 October, near-inertial wind stress increased due to forcing from the previously mentioned deep fall low that preceded ETC Epsilon (Figures 6-11 and 6-12). Given the bandpass filtering, there is no way to delineate when this forcing stopped and when Epsilon-induced forcing took over. However, the influence of the remnants of ETC Epsilon are apparent as the maximum near-inertial wind stress coincided with the approach and passage of the storm. The maximum cyclonic near-inertial wind stress was 3.74 cN m^{-2}, occurring at 0314 UTC 27 October; while The maximum anticyclonic near-inertial wind stress was 1.71 cN m^{-2} at 0144 UTC 27 October (Figures 6-11 and 6-12). After the passage of the storm, near-inertial wind stress drastically subsided.

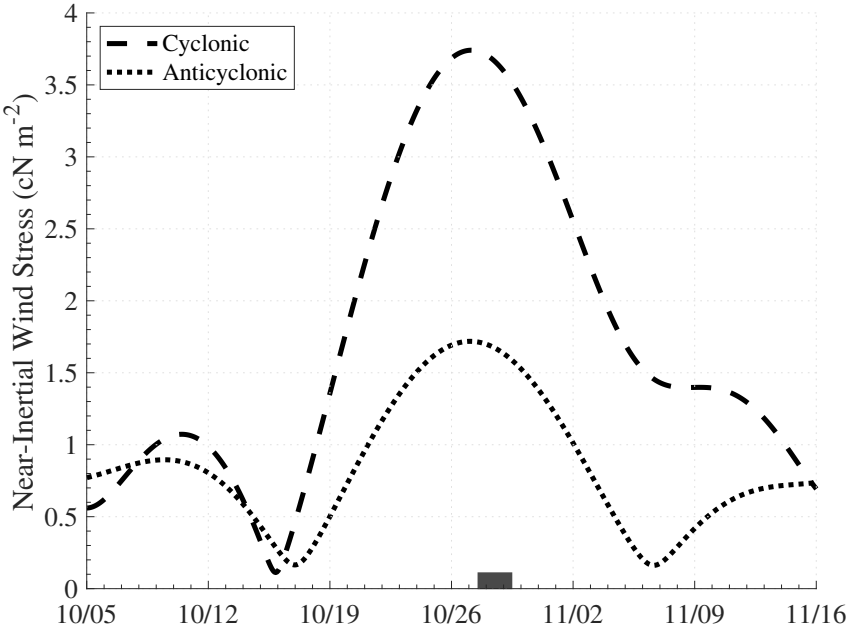

Figure 6-11: Time series of cyclonic and anticyclonic near-inertial wind stress (cN m^{-2}) estimations from X-Spar before, during (gray rectangle), and after the passage of the remnants of ETC Epsilon. Near-inertial wind stress was derived according to the procedure set forth by Silverthorne and Toole [6].

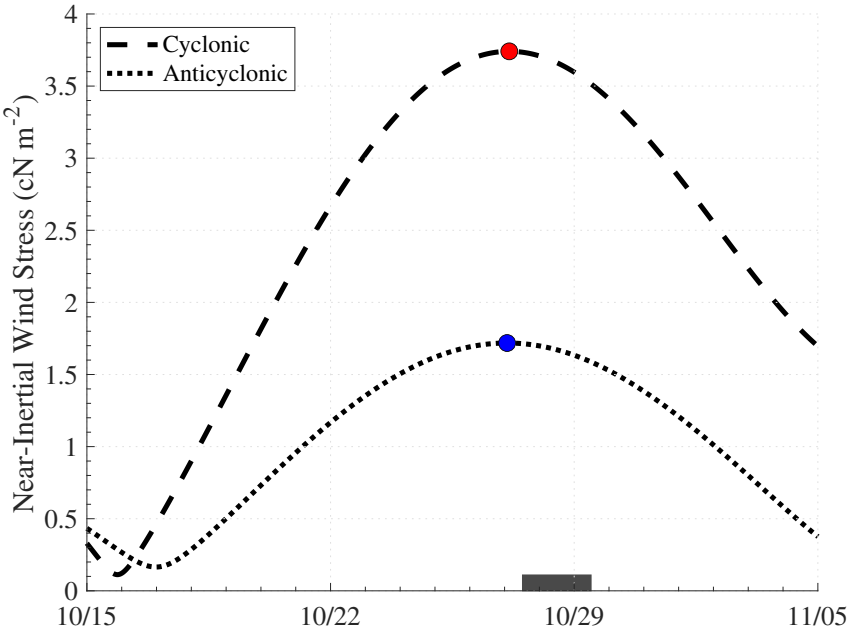

Figure 6-12: As Figure 6-11, but from 0000 UTC 15 October to 0000 UTC 05 November, highlighting the passage period to resolve the peaks of cyclonic and anticyclonic near-inertial wind stress.

6.4 Sea-State

Throughout its life cycle, Epsilon generated an enormous wave field, highlighted by record-breaking surf along the European Atlantic coast (Figures 6-13 and 6-14). On 28 October, the M6 weather buoy of the Irish Marine Data Buoy Observation Network, observed one of the largest individual waves ever recorded: a 32.3 m rogue wave located 435 km west of the Irish coast over the Rockall Trough (∼3,000 m depth) [92]. Reanalysis of the wave data has validated this observation and confirmed that the wave achieved rogue-status, as it reached 2.4 times the amplitude of the locally averaged SWH field. Further, on 29 October, Sebastian Steudtner of Germany set the world record for largest wave ever surfed when he took off on a 26.2 m wave off the coast of Praia do Norte, Nazaré, Portugal (Figure 6-15). The feat has since been ratified by Guinness World Records, breaking the previous three-year standing record by 1.8 m. Of note, Nazaré as it is known, is an infamous big-wave surf break, where waves can reach more than 30 m during the late fall and winter due to the combination of frequent strong storms and unique mechanics of a submarine canyon only 1 km from the surf zone. This surf break accounts for seven of the ten largest waves ever surfer, including the top three (`https://www.redbull.com/us-en/biggest-waves-surfed`).

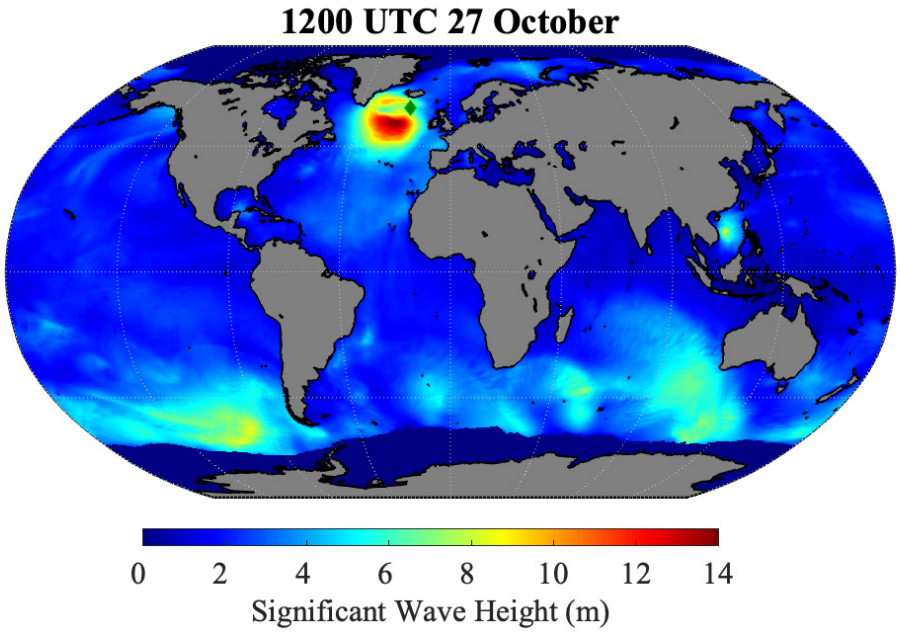

Figure 6-13: Global SWHs (m) at 1200 UTC 27 October highlighting that the waves observed by the NISKINe observational array (green diamond) were the largest in the world. Data courtesy of the Mercator Océan International Global Ocean Waves Reanalysis product.

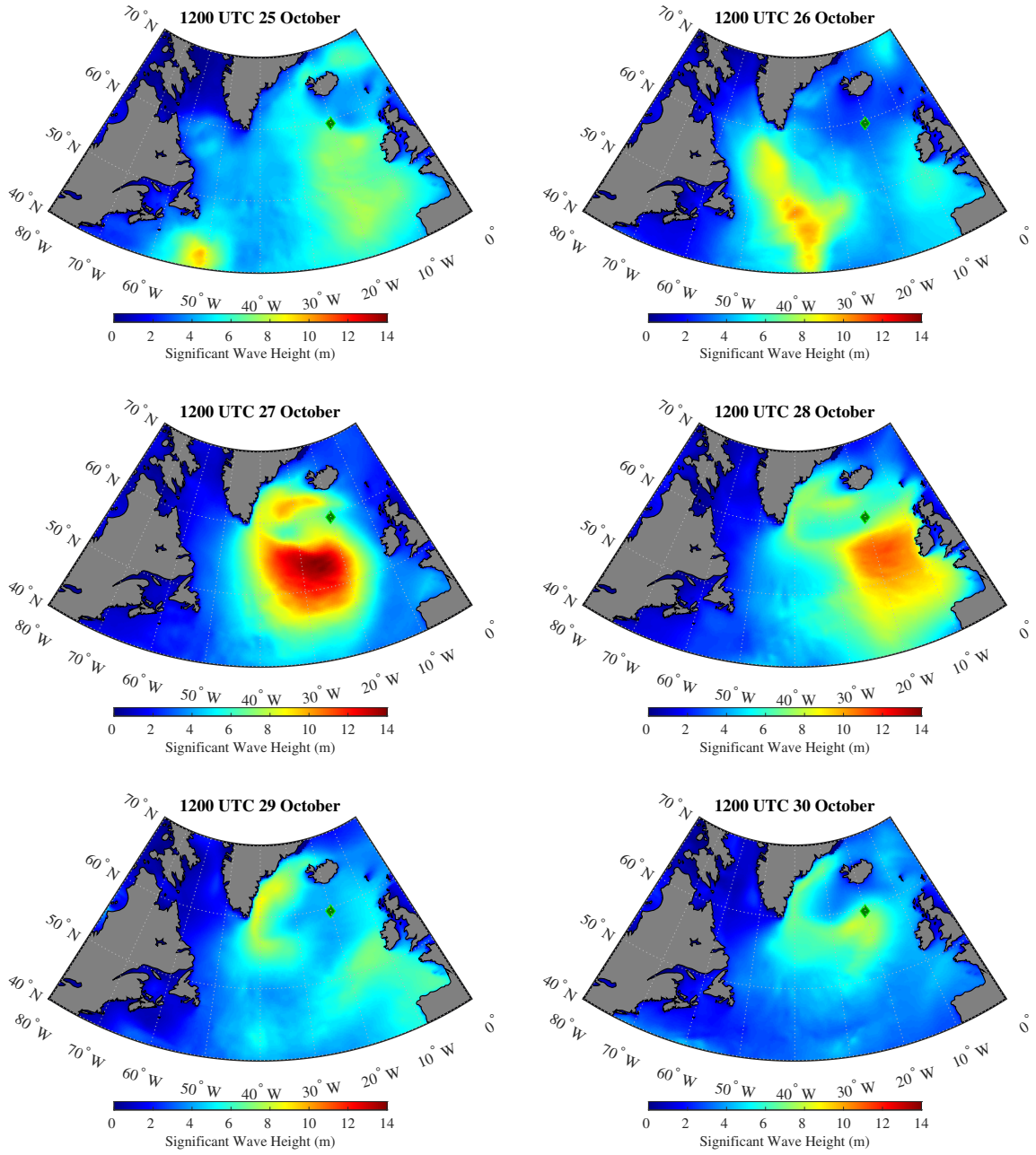

Figure 6-14: North Atlantic SWHs (m) every 24 hours from 1200 UTC 25 October to 1200 UTC 29 October. Data courtesy of the Mercator Océan International Global Ocean Waves Reanalysis product.

Figure 6-15: World record caliber waves breaking off the coast of Praia do Norte, Nazaré, Portugal, on 29 October due to the passage of the remnants of ETC Epsilon. Photograph courtesy of Heidi Hansen of Surfer Today.

X-Spar and ALAMO #9105 both observed 8 m SWHs as early as 0000 UTC 25 October, and showed that the mean wave field fluctuated between 6 and 10 m until 1800 UTC. On 26 October, SWHs decreased (Figures 6-16 and 6-17), closely coinciding with decrease of wind speed and stress (Figures 6-7 and 6-12). Then, SWHs built back to 8 m, and after briefly decreasing, increased further to exceed 10 m around 1200 UTC 27 October, the highest in the record (Figures 6-16 and 6-17). The NWS/NCEP OPC sea-state analysis, issued at 1325 UTC 27 October, valid for 1200 UTC, hindcasted that 7 to 9 m SWHs were in the vicinity of the NISKINe observational area (Figure 6-18). Both platforms recorded higher than hindcasted SWHs: ALAMO #9105 reported maximum SWHs of 9.8 m at 1911 UTC 27 October, while X-Spar measured 11.1 m at 1910 UTC (Figures 6-16 and 6-17). These observations indicate that the sea-state was slightly larger than NWS/NCEP OPC predicted.

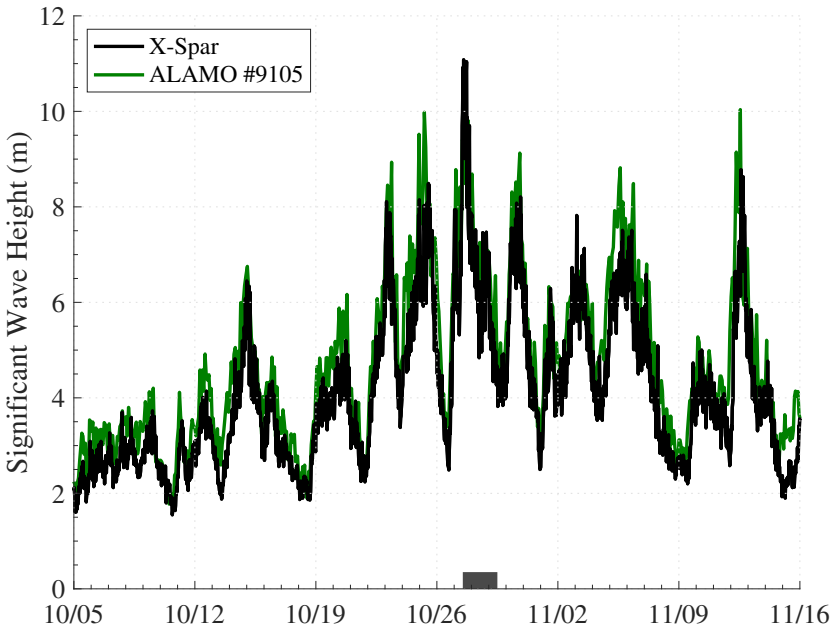

Figure 6-16: Time series of SWH (m) observations from X-Spar (black) and ALAMO #9105 (green) before, during (gray rectangle), and after the remnants of the passage of ETC Epsilon.

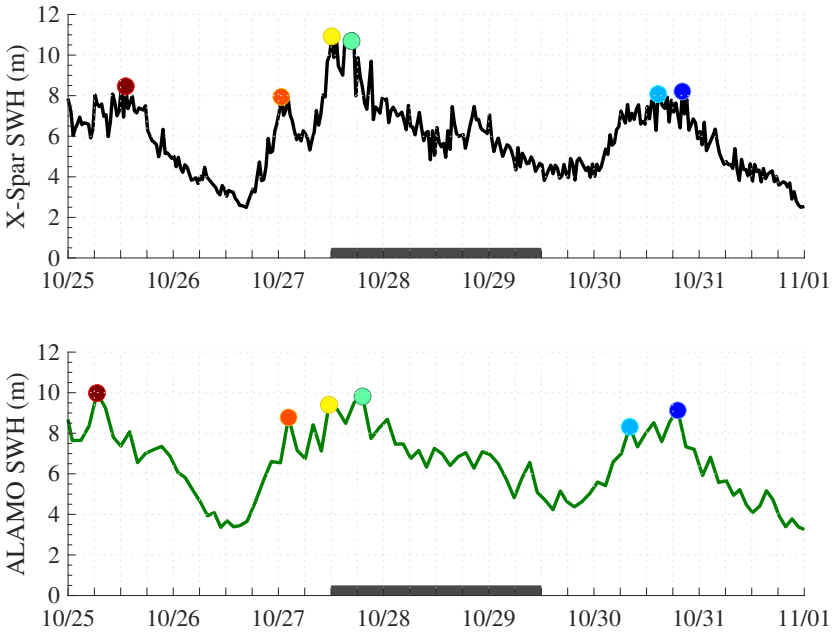

Figure 6-17: As Figure 6-16, but from 0000 UTC 25 October to 0000 UTC 01 November, highlighting the passage period to resolve 8 m SWHs due to the deep fall low preceding the remnants of ETC Epsilon (red circle), 8 to 10 m SWHs as the storm inundated the observational area (orange, yellow, and green circles), and 8 m SWHs on 30 October (blue circles), after which the evidence of an Epsilon-induced sea-state is hard to discern.

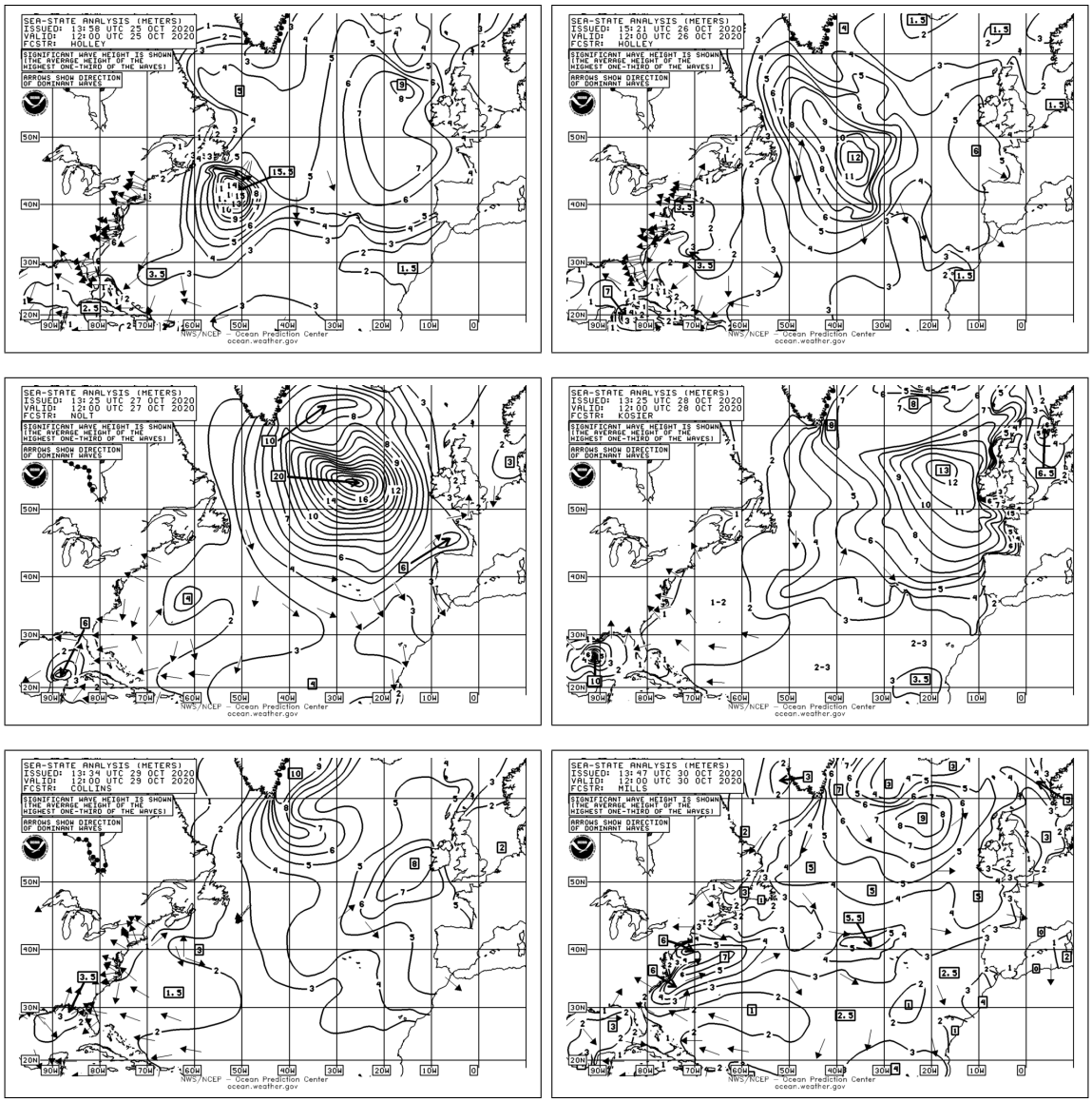

Figure 6-18: Sea-state analysis every 24 hours from 1200 UTC 25 October to 1200 UTC 30 October, hindcasting the North Atlantic sea-state. Images courtesy of NWS/NCEP OPC.

Post-storm analysis shows that the design of X-Spar likely led to a tendency to measure slightly lower SWHs (∼0.5 m) than ALAMO #9105. For the largest amplitude waves, ALAMO #9105 reports higher SWHs than X-Spar; while for the smallest amplitude waves, X-Spar reports higher SWHs than ALAMO #9105 (Figure 6-19). X-Spar, as a long spar buoy, tends to dampen high frequency motion while following the motion of the low frequency swell. Therefore, the low frequency component of the wave field is estimated by the heave of the platform, computed using the inertial

motion package. The high frequency component is measured by the subsurface pressure sensor, and the combination is used to compute the total wave field. However, the wave-induced pressure signal decays exponentially with depth, and, although an attempt was made to manually compensate for the decay, this is the most plausible reason for the discrepancy between the X-Spar and ALAMO #9105 SWH measurements.

Another possibility for the discrepancy is that ALAMO is simply a better wave-follower. While this seems like a disadvantage for X-Spar, the tendency to follow lower frequency waves makes X-Spar a more stable platform to make atmospheric boundary layer measurements. This allows for continuous and more accurate turbulent flux estimates, as compared to purely surface following platforms such as ALAMO when communicating via Iridium, traditional surface moorings, or Saildrone. Therefore, X-Spar may have an accuracy trade-off between atmospheric boundary layer measurements and observations of the wave field - at least with the current atmospheric sensor suite package. While both platforms are capable for collecting wave data, in their current designs, ALAMO is more-apt to observe high-frequency waves found in the storm environment; while X-Spar is better served to target lower frequency swell that organize and propagate away from the storm environment (Figure 6-19).

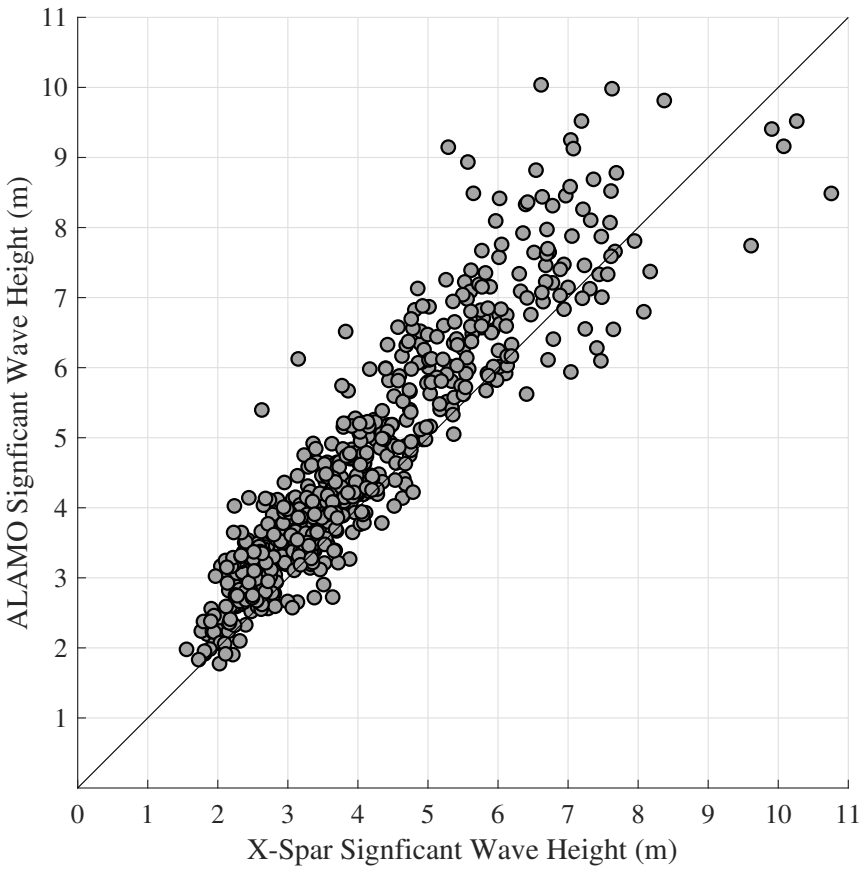

Figure 6-19: Scatter plot of X-Spar and ALAMO #9105 SWH observations with a one-to-one line for comparison.

6.5 Sea Surface Temperature

The NISKINe observational array provided a comprehensive way to assess SSTs before, during, and after the passage of the remnants of ETC Epsilon. All four instruments are capable of observing SSTs, and they all had similar readings; while, more promisingly, the trends in the data are exactly the same (Figure 6-20). At 1200 UTC 20 October, one week before the passage period, X-Spar measured 7-m air temperatures of 8.46°C and SSTs of 11.0°C. From 20 to 27 October, as the storm generated and approached the array, 7-m air temperature was fairly constant, while SSTs dropped by 0.5°C (Figure 6-20). From 29 October to 02 November, following the passage period, SSTs decreased by another 0.5 °C from 10.8°C to 10.3°C, while 7-m air temperatures fluctuated between 5.6°C and 9.2°C. Although an anomalous warm

air mass intruded into the observational area from 03 November to 06 November, causing slight warming of the surface ocean (Figure 6-20), the prominent cooling directly after the storm passage period is evidence of the cold wake of the storm. Observations of the cold wake caused by ETC Epsilon by all four instruments is an achievement for operational oceanography.

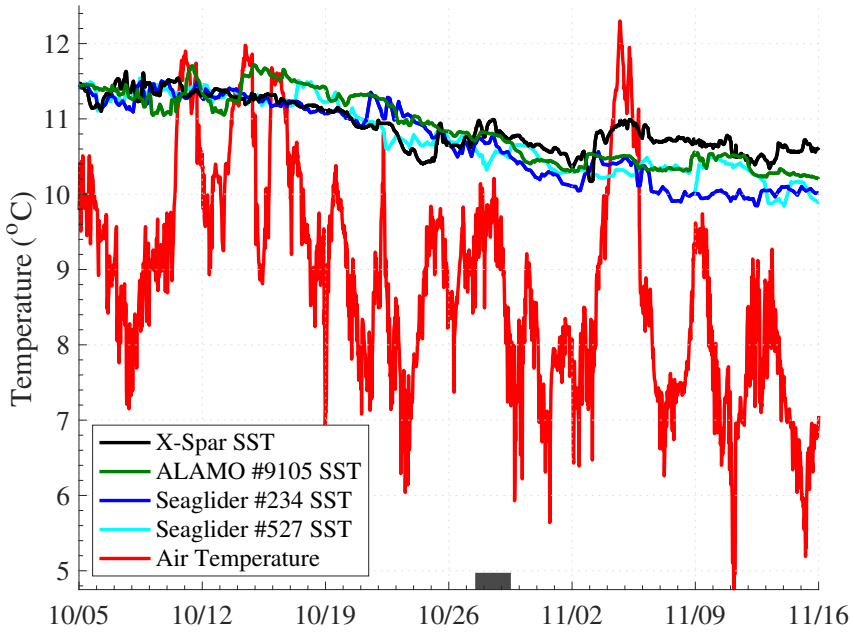

Figure 6-20: SSTs (°C) observations from NISKINe observational array: X-Spar (black), ALAMO #9105 (green), Seaglider #234 (blue), and Seaglider #527 (cyan), compared to 7-m air temperature observations from X-Spar (red), before, during (gray rectangle), and after the passage of the remnants of ETC Epsilon.

Chapter 7

Subsurface Ocean Observations

7.1 ALAMO Profiles

7.1.1 Temperature

Temperature profiles during early October show that the mean pre-passage thermocline resided between 60 and 100 dbar with mixed layer temperatures ranging from 11 to 11.5°C. On 25 October, mixed layer temperatures fell below 11.0° for the first time in the record, indicating the first sign of Epsilon-induced modulation (Figure 7-1). During the passage period, the mean mixed layer temperature decreased to 10.7°C, while the thermocline deepened between 100 and 120 dbar. Thus, during the passage period, Epsilon-induced forcing cooled the upper ocean by at least 0.8°C and shear-driven mixing deepened the thermocline by approximately 40 dbar. From 30 October to 17 November, mixed layer temperatures ranged from 10.0 to 10.6°C, while a weak thermocline existed below 120 dbar. As the storm dissipated, it left behind a considerably eroded thermocline and mixed layer temperatures had decreased by more than 1.0 °C (Figure 7-1). These observations validate the presence of a cold wake due to the passage of the remnants of ETC Epsilon, as presented in Figure 6-20.

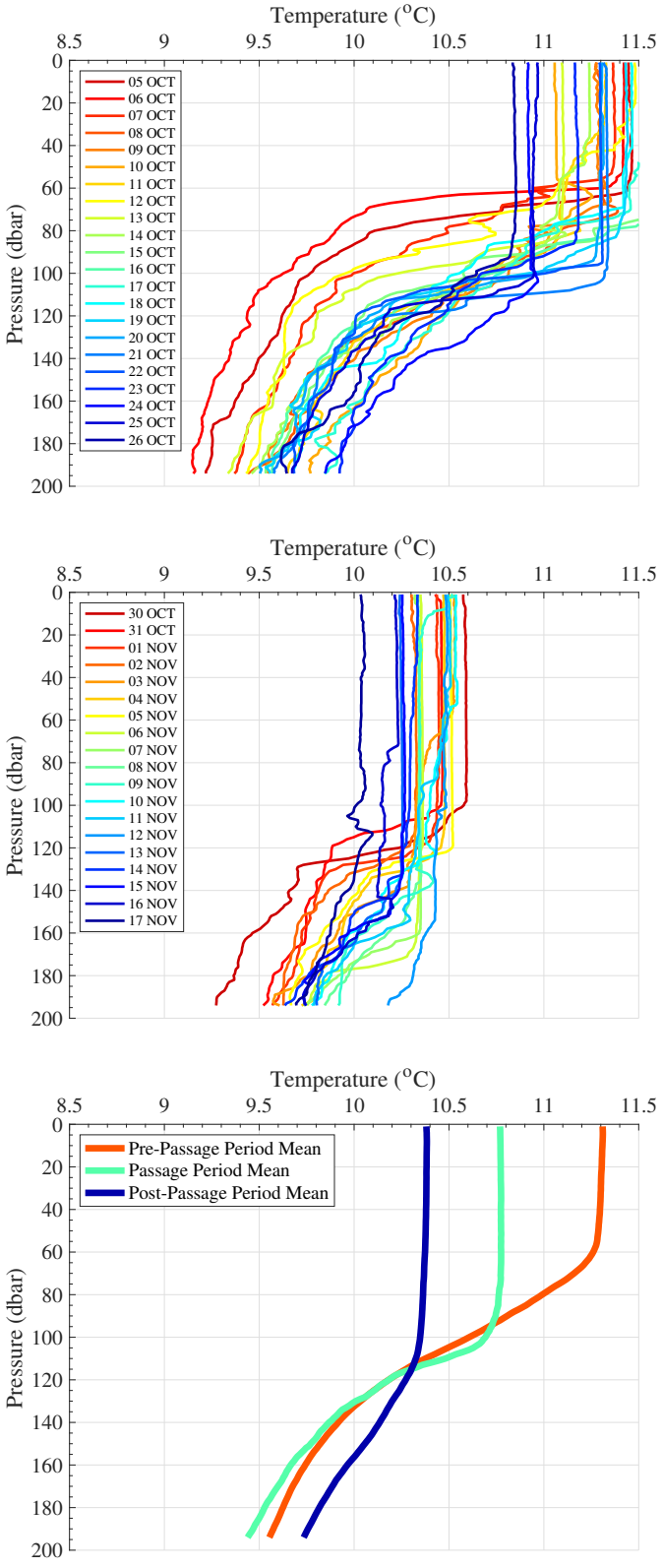

Figure 7-1: Top: ALAMO #9105 temperature (°C) profiles observed before the passage of the remnants of ETC Epsilon. Middle: As top panel, but for the post-passage period. Bottom: Mean temperature profiles before, during, and after the passage period.

7.1.2 Salinity

Pre-passage salinity profiles highlighted some variability due to the local precipitation and evaporation budget. The approach of the storm is highlighted as mixed layer salinities seemingly organized toward 35.25 PSU by 26 October. During the pre-passage period, the salinity field was constrained between 35.1 and 35.4 PSU, and the halocline resided between 60 and 80 dbar (Figure 7-2). The passage and post-passage mean salinity profiles are isohaline from the surface to below 100 dbar and exhibited an average mixed layer salinity of 35.25 PSU. Interestingly, the average mixed layer salinity increased during and after storm passage as compared to the pre-passage environment (Figure 7-2). These observations highlight that the mixing of saltier water, from depth, into the mixed layer and wind-induced evaporation outweighed any signature of fresh water input via precipitation during the passage period.

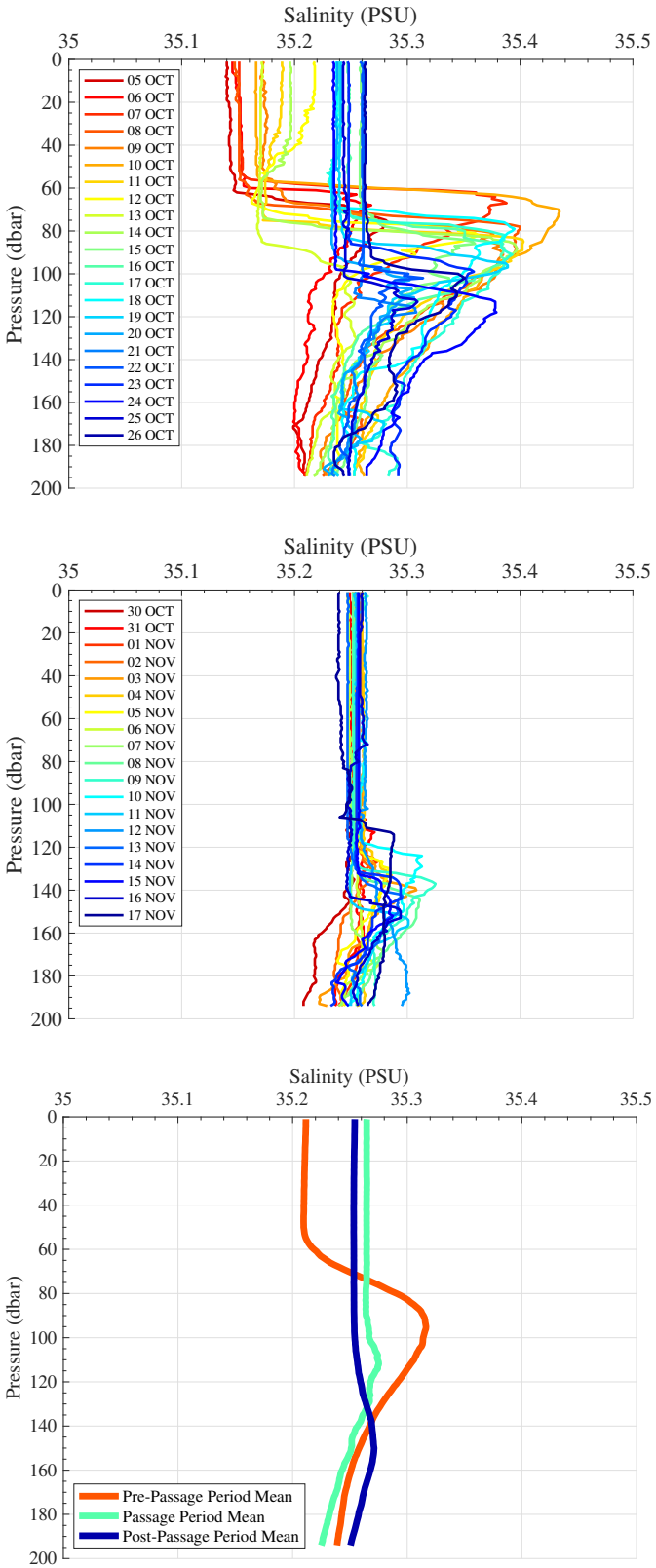

Figure 7-2: Top: ALAMO #9105 salinity (PSU) profiles observed before the passage of the remnants of ETC Epsilon. Center: As top panel, but for the post-passage period. Bottom: Mean salinity profiles before, during, and after the passage period.

7.1.3 Potential Density

Potential density ($\sigma_0 = \rho - 1000$) profiles show that before the passage of the remnants of ETC Epsilon, the North Atlantic grew more slightly dense as the upper ocean slightly cooled due to the seasonal transition from summer to fall (Figure 7-3). Throughout the pre-passage period, mixed layer potential density increased quasi-linearly towards 27 kg m^{-3}, and a strong pycnocline existed between 60 and 100 dbar. Given the steady increase in surface forcing leading up to the passage period, it is hard to discern when Epsilon-induced influence started to change the potential density field. However, by the start of the passage period on 27 October, significant Epsilon-induced modulation was occurring.

During the passage period, the pycnocline deepened beyond 100 dbar, and by the end of the passage period, mixed layer potential density ranged was bounded by 26.9 kg m^{-3} and 27.0 kg m^{-3} and a severely eroded pycnocline now existed at 150 dbar (Figure 7-3). Evolution of the potential density field was chiefly caused by the presence of shear-driven mixing and a decrease of upper ocean temperature as a result of the passage of the storm (Figures 7-1 and 7-3). This stands to reason in the context of the Equation of State for Seawater, as the dependence of potential density is nonlinear in the favor of temperature, vice salinity. This makes further sense given the context that variability of the salinity field was small and no precipitation signature was detected during the passage period (Figures 7-2).

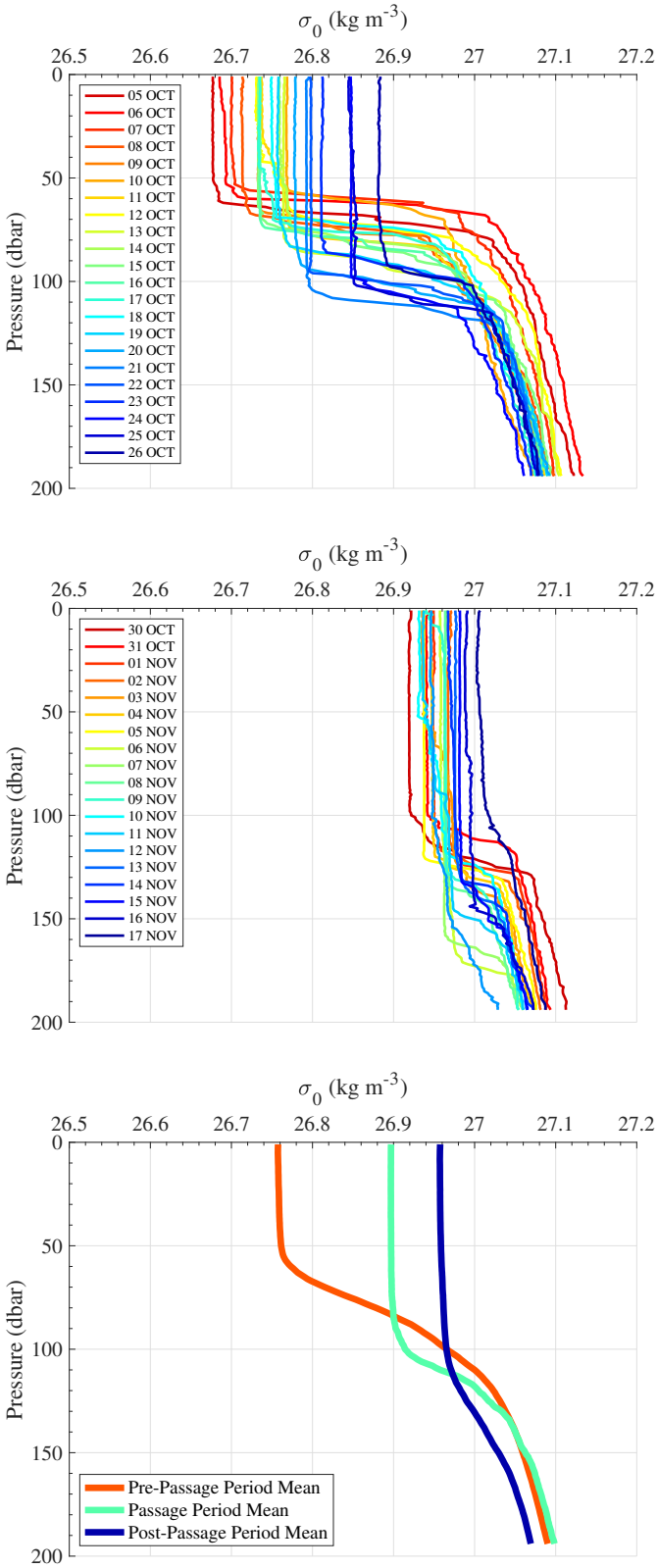

Figure 7-3: Top: ALAMO #9105 potential density ($\sigma_0 = \rho - 1000$; kg m^{-3}) profiles observed before the passage of the remnants of ETC Epsilon. Middle: As top panel, but for the post-passage period. Bottom: Mean potential density profiles before, during, and after the passage period.

7.2 Upper Ocean Transects

7.2.1 Temperature, Salinity, and Stratification

Subsurface ocean observations from the NISKINe observational array revealed a strong and enduring subsurface response due to the passage of the remnants of ETC Epsilon. Similar to the profiles presented in Section 7.1 (Figures 7-1, 7-2, and 7-3), ALAMO #9105, Seaglider #234, and Seaglider #527 upper ocean transects detailed intraseasonal variability characteristic of fall prior to the approach of the storm. Upper ocean conditions started to change by 26 October (Figures 7-4, 7-5, and 7-6), one day before storm passage, coinciding with the arrival of the Epsilon-induced surface forcing, as discussed in Chapter 6. Deepening of the mixed layer is evident in vertical records of the temperature, salinity, and potential density fields (Figures 7-4, 7-5, and 7-6). Further, the passage period delineates an impressive pre-storm and post-storm environment contrast of the upper ocean temperature. Figures 7-4, 7-5, and 7-6 highlight the stark transition from the summer to winter stratification regimes as well as a near-erasing of the halocline caused by Epsilon-induced forcing.

As early as 27 October, high-amplitude NIWs oscillated at the base of the mixed layer, evident by the contours heaving upward in the bottom panels of Figures 7-4, 7-5, and 7-6. The Brunt-Väisälä frequency, or buoyancy frequency, was derived using Seaglider data to better assess upper ocean stratification and the time evolution of the mixed layer surrounding the passage period (Figures 7-7 and 7-8). Strong stratification, indicated by a high buoyancy frequency, means more work is required to mix parcels across isopycnals; whereas, less work is required in regions of weak stratification. Thus, the depth of maximum buoyancy frequency can be used to asses mixed layer depth, which separates the upper ocean from the interior. Both Seagliders highlight the rapid and sustained increase of the depth of maximum buoyancy frequency during and after the passage of the storm and also indicate the presence of NIWs (Figures 7-7 and 7-8).

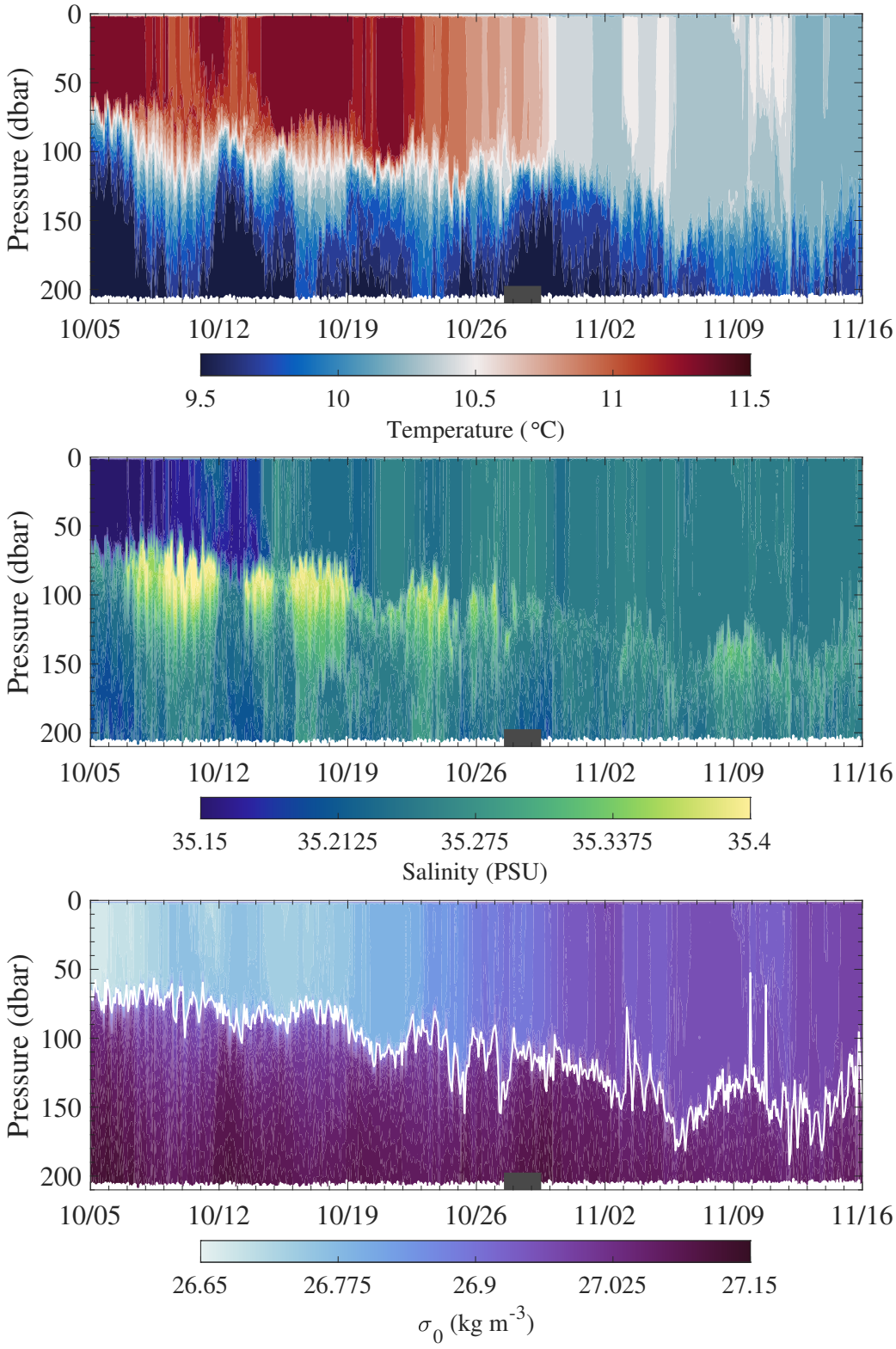

Figure 7-4: Top: ALAMO #9105 (°C) temperature transect before, during (gray rectangle), and after the passage of the remnants of ETC Epsilon. Middle: As top panel, but for salinity (PSU). Bottom: As top and middle panels, but for potential density ($\sigma_0 = \rho - 1000$; kg m^{-3}).

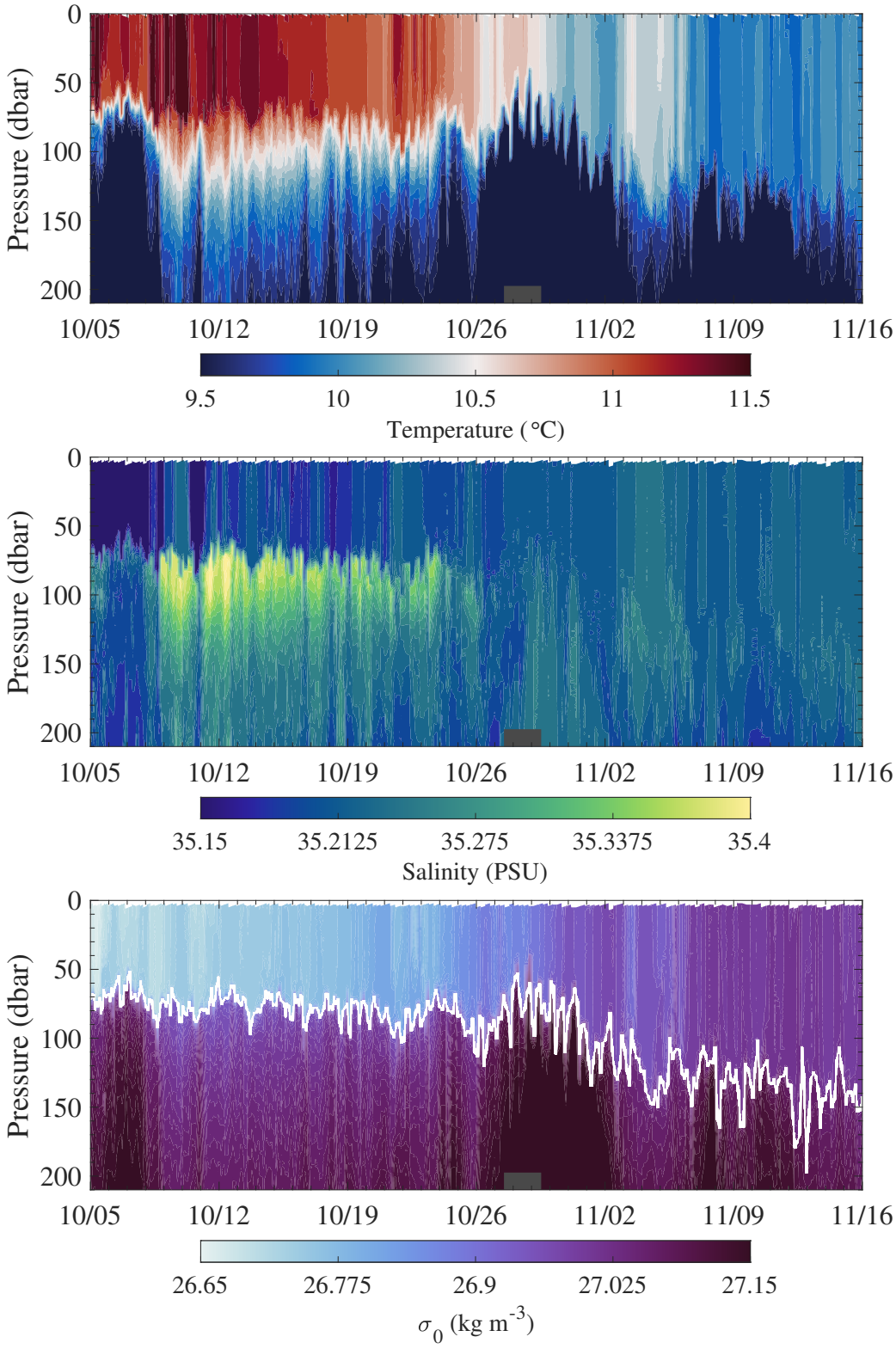

Figure 7-5: As Figure 7-4, but for Seaglider #234.

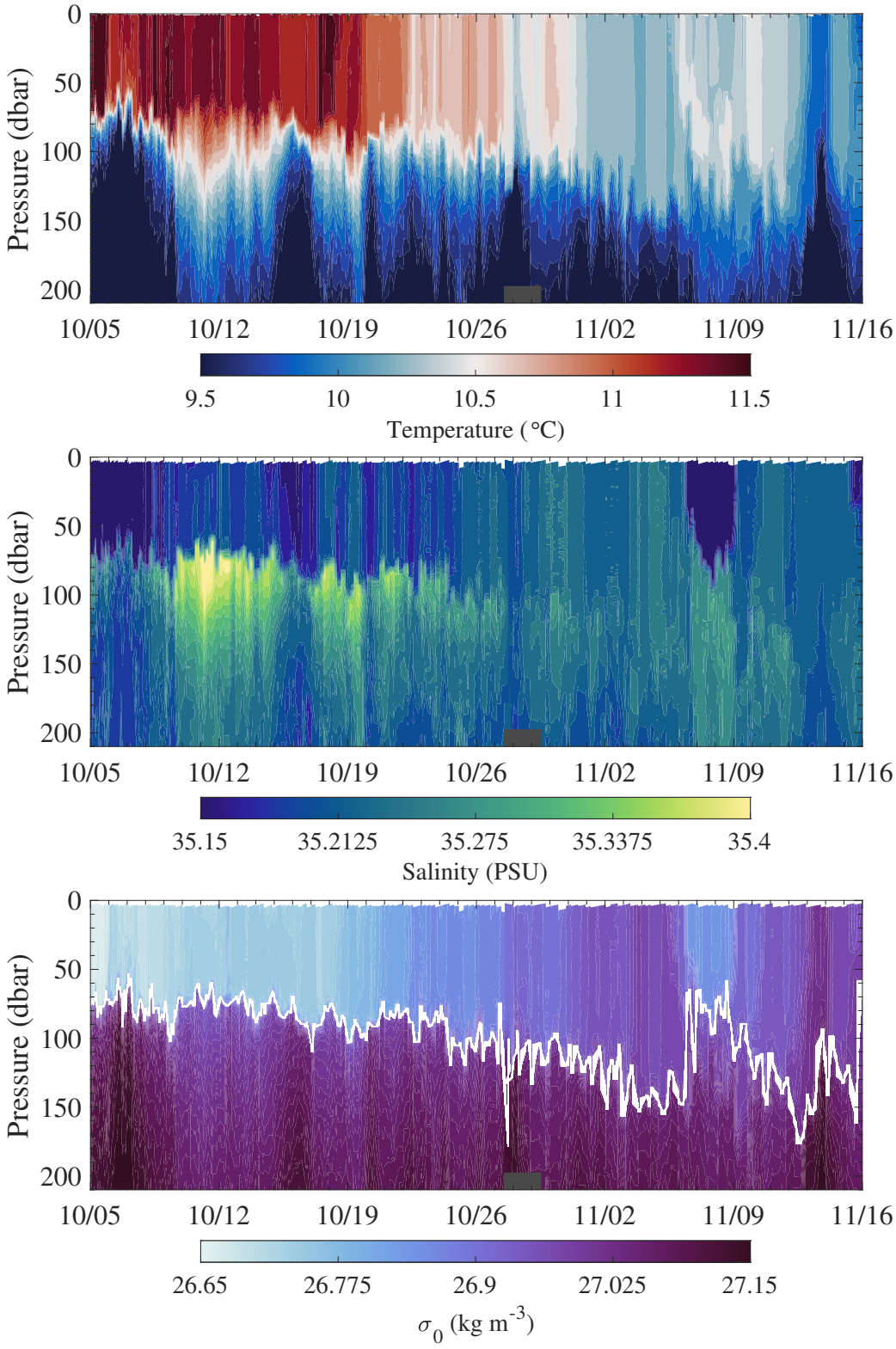

Figure 7-6: As Figures 7-4 and 7-5, but for Seaglider #527.

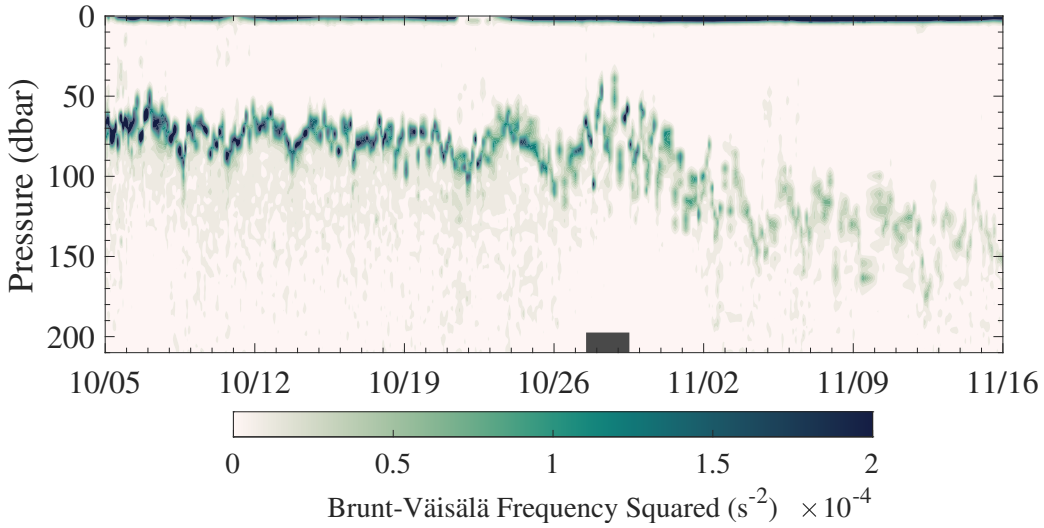

Figure 7-7: Brunt-Väisälä frequency squared (s^{-2}), as calculated from observations by Seaglider #234 before, during (gray rectangle), and after the passage of the remnants of ETC Epsilon.

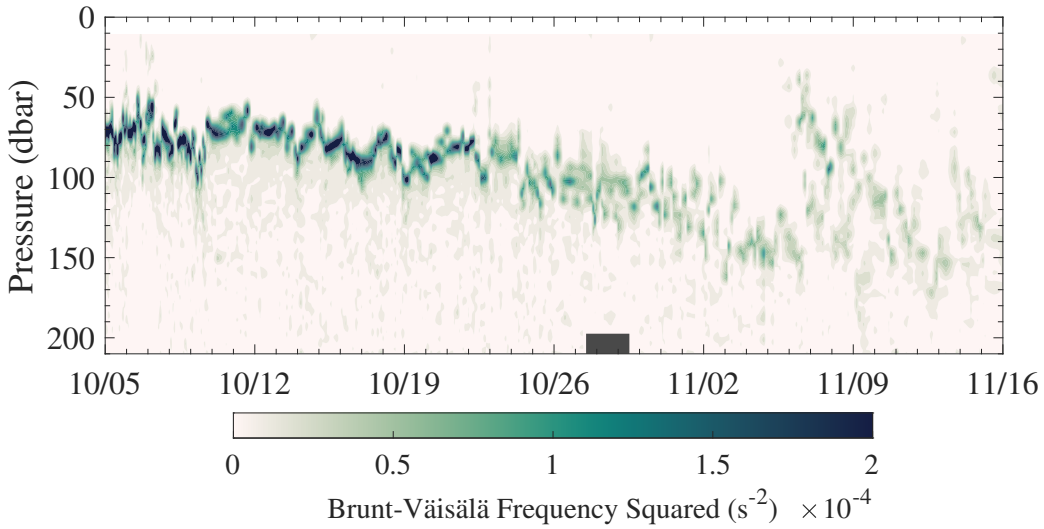

Figure 7-8: As Figure 7-7, but for Seaglider #527.

7.2.2 Total & Near-Inertial Currents

Calculations derived from Seaglider ADCP data elucidated how the remnants of ETC Epsilon input kinetic and near-inertial energy into the upper ocean (Figures 7-9, 7-10, 7-11, and 7-12). The near-inertial currents were extracted from the total current magnitudes using a complex Morlet wavelet demodulation at the local inertial frequency and filter-width of one day, according to the routine of Liu and Miller [93]. As early as 25 October, Seaglider #234 detailed near-inertial current magnitudes greater than 0.15 m s^{-1} as deep as 60 dbar (Figures 7-11 and 7-12). As expected, the strongest total and near-inertial currents were observed during and after the passage period and correlate to when heaving of the mixed layer was observed in Figures 7-4, 7-5, 7-6, 7-7, and 7-8. By 28 October, the near-inertial signal reached its peak, measuring greater than 0.20 m s^{-1} until 31 October and subsiding there afterwards. During this period, signals of this magnitude propagated as deep at 90 dbar.

The near-inertial currents extracted from the Seaglider #527 ADCP data were not as significant during the passage period. Figure 7-12 mainly details a significant input of near-inertial energy directly after deployment. Although, there was a moderate near-inertial signature on the order of 0.10 m s^{-1} during the passage period, which encouragingly extended past 100 dbar. Given these observations, there is not is sufficient evidence of NIW propagation into the ocean interior. Figures 7-11 and 7-12 indicate that NIWs rapidly decayed at approximately 100 dbar. Alternatively, the NIWs could have horizontally propagated away from the generation area in the "out-of" or "into-the-page" directions; however, this is unlikely. Given these observations, these signals of near-inertial energy are cautiously classified as high-mode NIWs that contributed to mixing close to the NISKINe observational array.

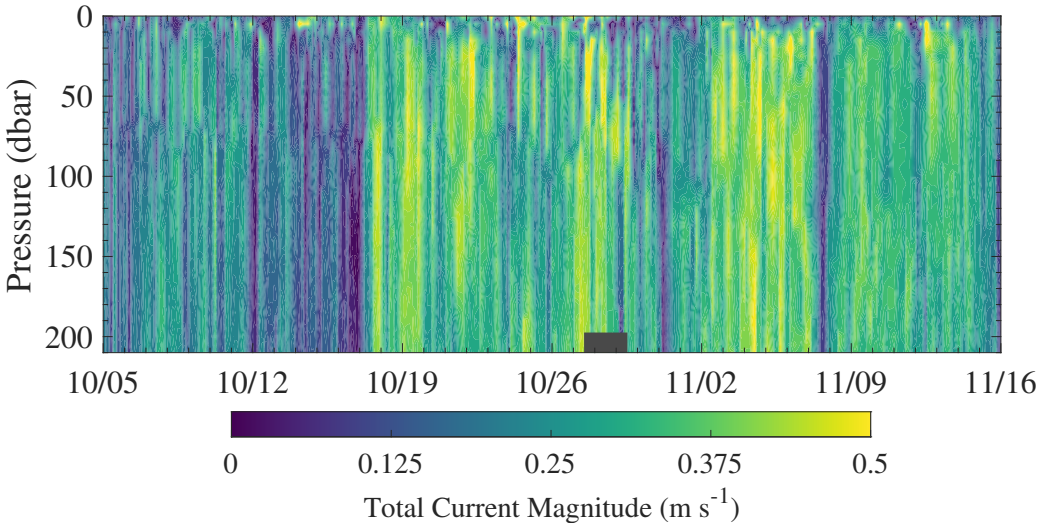

Figure 7-9: Total current magnitude (m s^{-1}), as calculated from observations by the ADCP onboard Seaglider #234 before, during (gray rectangle), and after the passage of the remnants of ETC Epsilon.

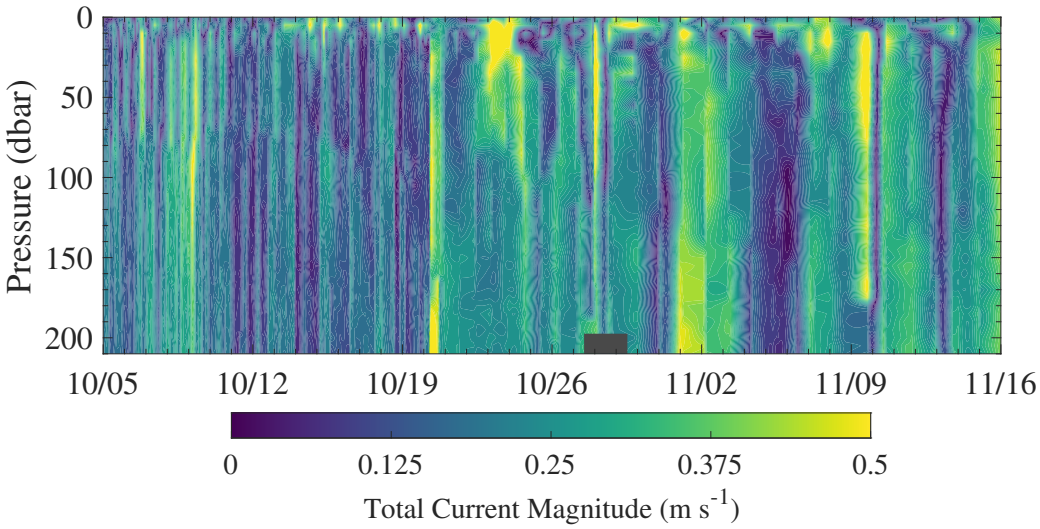

Figure 7-10: As Figure 7-9, but for Seaglider #527.

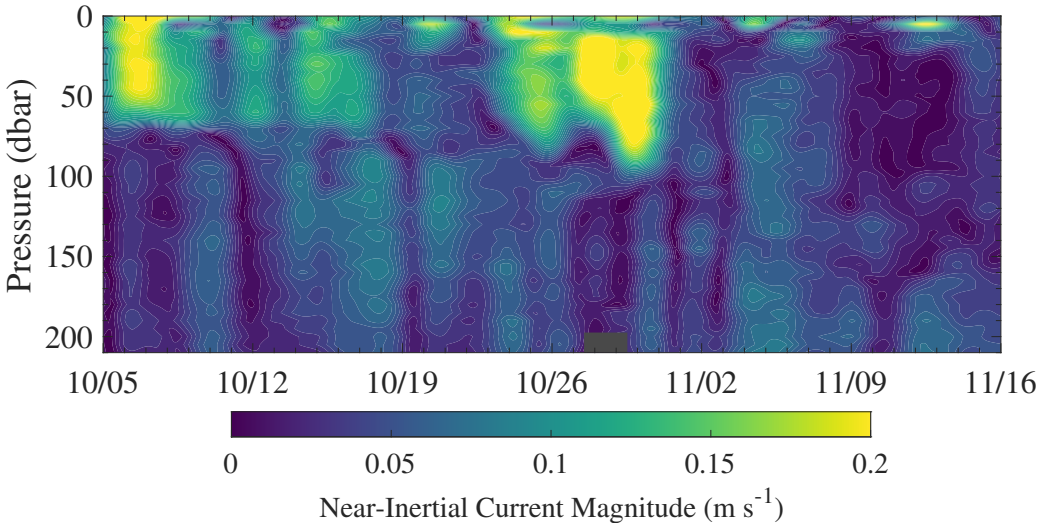

Figure 7-11: Near-inertial current magnitude (m s^{-1}), as calculated from observations by the ADCP onboard Seaglider #234 before, during (gray rectangle), and after the passage of the remnants of ETC Epsilon.

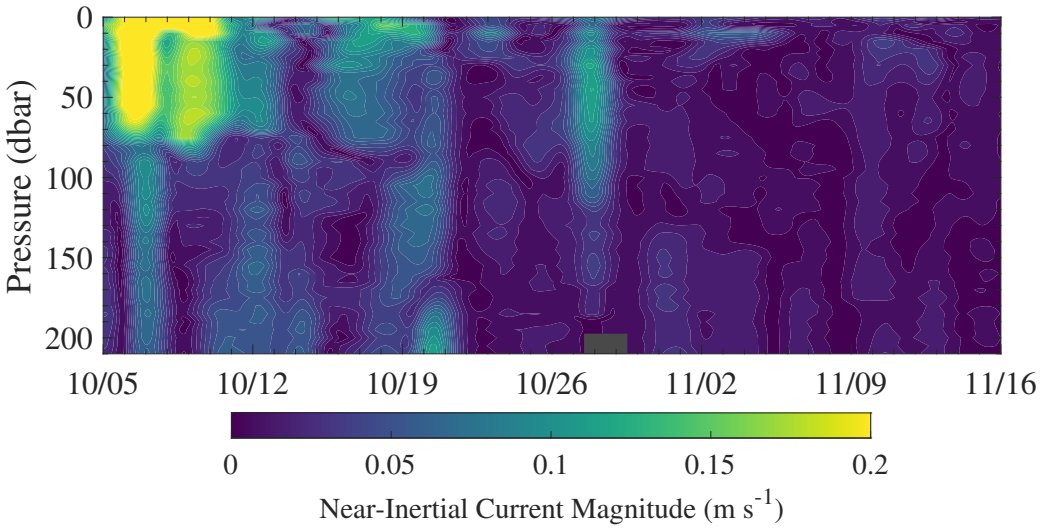

Figure 7-12: As Figure 7-9, but for Seaglider #527.

7.2.3 Shear-Driven Mixing

During and after the passage period, vertical velocity shear was strongly enhanced in the near-surface and at the base of the mixed layer (Figures 7-13 and 7-14). While the presence of strong velocity shear is necessary to drive shear-driven mixing, it is not a sufficient condition to induce it; as it must overcome the local stratification in order to stir the environment. Evidence for shear-driven mixing can be examined by using reduced shear, which is defined as $S^2 - 4N^2$, where S is the velocity shear (Figures 7-13 and 7-14), and N is buoyancy frequency, as above (Figures 7-7 and 7-8). This parameter is a means of assessing the stability regime across the upper ocean, unstable, stable, or neutral. Regions of the water column characterized by the unstable regime are the most susceptible to shear-driven mixing. In such regions, shear-driven mixing can overcome the existing stratification and vertically mix parcels. The passage of the remnants of ETC Epsilon intensified the signature of unstable regions (Figures 7-15 and 7-16), and as such, Epsilon-induced forcing triggered strong momentum and buoyancy forcing which enhanced vertical shear. These signature were most evident at the base of the mixed layer, resulting in significant deepening (Figures 7-13, 7-14, 7-15, and 7-16).

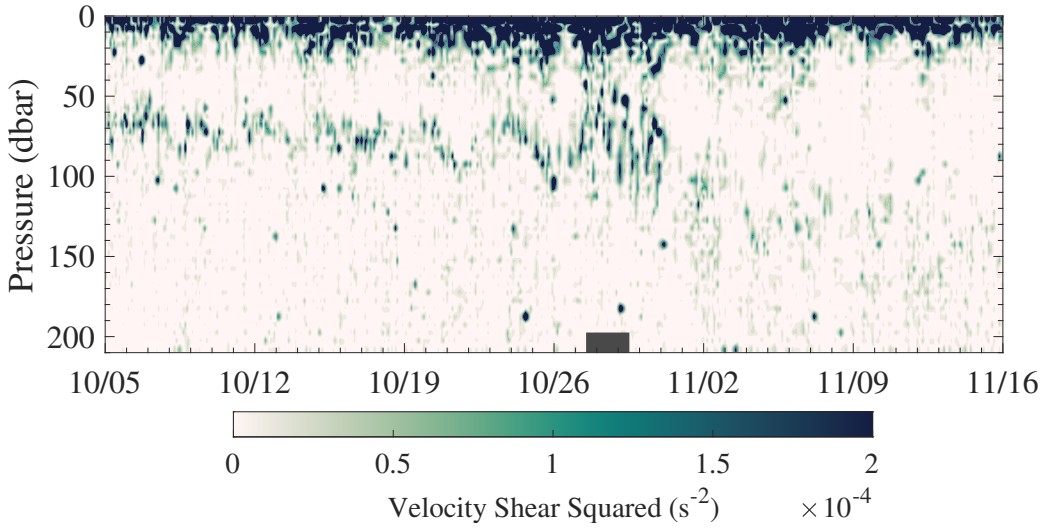

Figure 7-13: Velocity shear squared (s^{-2}), as calculated from observations by the ADCP onboard Seaglider #234 before, during (gray rectangle), and after the passage of the remnants of ETC Epsilon.

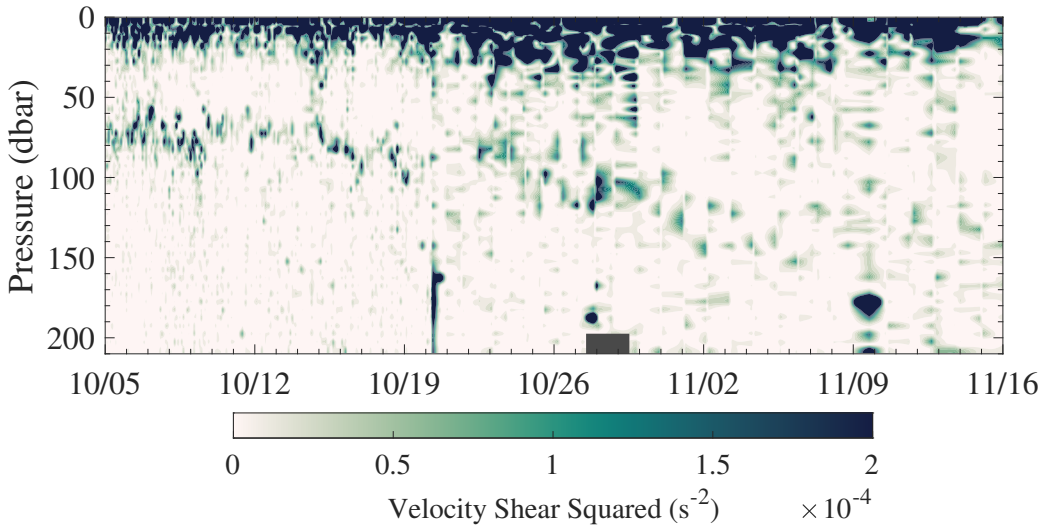

Figure 7-14: As Figure 7-13, but for Seaglider #527.

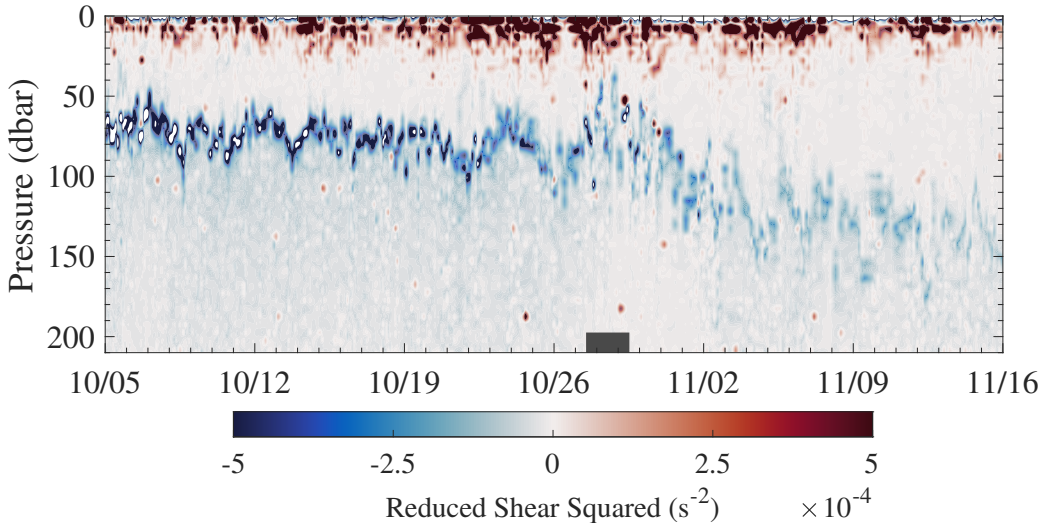

Figure 7-15: Reduced shear squared (s^{-2}), as calculated from observations by the ADCP onboard Seaglider #234 before, during (gray rectangle), and after the passage of the remnants of ETC Epsilon.

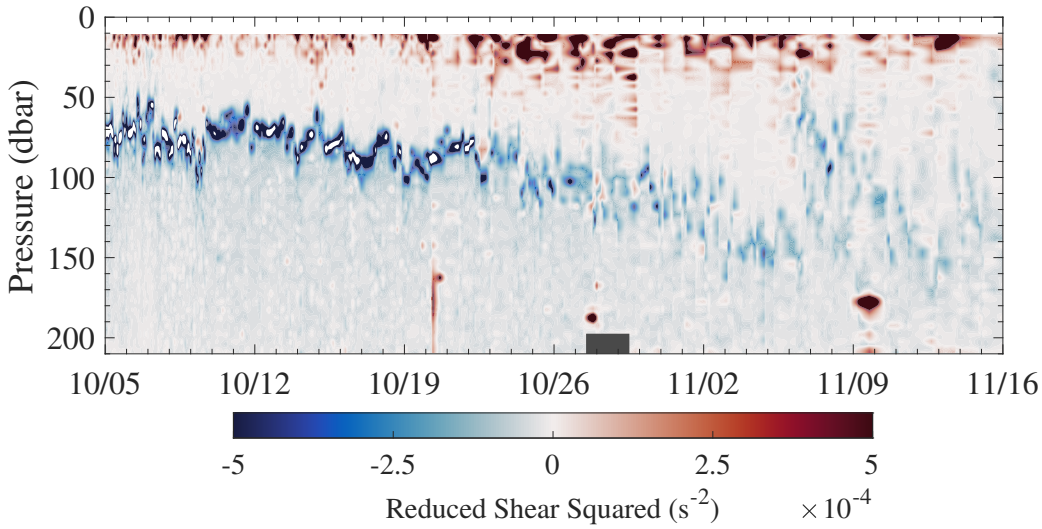

Figure 7-16: As Figure 7-15, but for Seaglider #527.

THIS PAGE INTENTIONALLY LEFT BLANK

Chapter 8

Conclusions and Way Ahead

8.1 Summary

Highlights of the surface and subsurface observations of the NISKINe observational array before, during, and after the passage of the remnants of ETC Epsilon are as follows: time evolution of total and inertial wind stress (Figures 6-9, 6-10, 6-11, and 6-12), leading to sustained period of surface cooling (Figure 6-20); modulation of the upper ocean temperature, salinity, and density structures (Figures 7-4, 7-5, and 7-6); vigorous shear-driven mixing (Figures 7-13, 7-14, 7-15, and 7-16), leading to a deepened mixed layer (Figures 7-7 and 7-8); and evidence of generation, propagation, and decay of high-mode NIWs (Figures 7-11 and 7-12). Given these observations, the NISKINe observational array elucidated how Epsilon-induced forcing accelerated the onset to the winter stratification regime by breaking down the residual North Atlantic summer stratification via significant cooling and mixing processes.

8.2 Contribution

As a part of the ONR NISKINe DRI, this study explored air-sea interaction in the subpolar North Atlantic during the passage of the remnants of ETC Epsilon using three types of autonomous platforms: the X-Spar buoy, the ALAMO profiling float, and two Seagliders. While the passage of the storm was unforeseen, the utility and

unique capabilities of each platform enabled a multi-pronged approach to investigate the evolution of the upper ocean before, during, and after the passage of a strong forcing event. The synergistic capabilities of the observational array facilitated a thorough understanding of how the storm affected upper ocean structure to the generation, propagation, and decay of NIWs. Most of all, the NISKINe observational array proved that it has the potential to become a force multiplier for the TC and ETC prediction communities. This is a significant accomplishment, and congratulations are due to all those involved.

8.3 Future Work

8.3.1 Improving Intensity Forecasts

Future deployments of this, or similar, complimentary observational arrays ahead of TCs and ETCs will provide coupled numerical prediction models with more comprehensive initialization datasets. The assimilation of real-time subsurface data will greatly improve the accuracy of intensity forecasts; thus, allowing forecasters to make more informed advisories and issue more credible warnings in order to keep the public safer.

8.3.2 NISKINe Dataset

Future work could include using measurements from the NISKINe observational array to test and interpret mixed layer models that predicted the upper ocean response to the passage of the remnants of ETC Epsilon. This will lead to an improved understanding about how momentum, sensible heat, and moisture fluxes input near-inertial energy into the upper ocean. Further, building off this contemporaneous dataset will facilitate a continued understanding of the physics that govern how the upper ocean responds to the passage of a TC or ETC.

8.3.3 X-Spar

On 24 March, X-Spar was recovered by the Icelandic Coast Guard who reported that its mast had broken off, and unfortunately, the full dataset was lost. However, analysis of the telemetered data is underway beyond this thesis. Future work will include leveraging X-Spar to investigate the seasonally varying upper ocean response to surface forcing and how high-mode NIWs affect the upper ocean in the presence of a mesoscale vorticity field. Further, X-Spar data will be used to improve the understanding of air-sea coupled physics and enhance bulk-formula-type air-sea flux parameterizations. Application of these capabilities will increase the skill of coupled numerical prediction models.

Even though the instrument was badly damaged, this deployment of X-Spar was worthwhile. The results from the 2020 NISKINe deployment are being used to harden the X-Spar telemetry system as well as increase the robustness and performance of the meteorological sensors in high winds and large, steep waves. This will likely call for a slight redesign. In future iterations of X-Spar, an infrared hygrometer will be merged with the DCFS to directly measure sensible and latent heat fluxes. Both are of particular interest in the tropics, so X-Spar could be deployed to investigate tropical cyclogenesis. The instrument will also be equipped with upward and downward-looking ADCPs to sample upper ocean currents and directional wave spectra. The salvaged structure of X-Spar is in storage at WHOI, awaiting refurbishment, further testing, and tasking.

8.3.4 ALAMO

More ALAMOs will be deployed during operational storm reconnaissance missions by the WHOI Air-deployed Profiling Instruments Group, thanks to continued support and hospitality of the United States Air Force Reserve 53$^{\text{rd}}$ Weather Reconnaissance Squadron. These observations will continue to measure ocean heat content and other important upper ocean features ahead of TCs, initialize coupled numerical prediction models with real-time subsurface data, and ultimately enable a better understanding

of the evolution of the upper ocean during and after storms. The continued integration of WIMS onboard ALAMO will allow for more rigorous characterizations of TC-induced wave fields, which will improve storm surge forecasting. Further, developments to improve ALAMO are currently underway. This includes the integration of passive acoustic receivers to estimate wind speeds and therein turbulent mixing beneath storms; acoustic positioning and communications to support Arctic missions and enhance under-ice capabilities, and testing of bottom anchoring modules.

8.3.5 Seagliders

The IOP group at APL-UW has been on the cutting edge of the development of buoyancy-driven autonomous underwater vehicles for over a decade. They will continue to do so by rolling out the new generation of Seaglider known as SGX. SGXs tout incredible endurance via 60% more battery life, which has resulted in year-round mission capability. This has proven especially advantageous for under-ice Arctic missions. Future missions for SGX could include interseasonal observations of the upper ocean.

8.4 Data Availability

X-Spar

Telemetered data from X-Spar is password-protected, but available at `https://www2.whoi.edu/site/casimas/data/niskine-data/`. Please contact Dr. James B. Edson, `jedson@whoi.edu`, or Dr. John M. Toole, `jtoole@whoi.edu`, to request access.

ALAMO #9105

Quality controlled data from ALAMO #9105 is publicly available at `https://argo.whoi.edu/alamo/9105/`.

Seagliders #234 and #527

Raw Seaglider data from the 2020 NISKINe deployment is publicly available at `https://iop.apl.washington.edu/seaglider/dives.php?glider=234\&mission=NISKINE_Oct20\&count=0`, and `https://iop.apl.washington.edu/seaglider/dives.php?glider=527\&mission=NISKINE_Oct20\&count=0`, respectively.

THIS PAGE INTENTIONALLY LEFT BLANK

Bibliography

[1] H. L. Simmons and M. H. Alford. Simulating the long-range swell of internal waves generated by ocean storms. *Oceanography*, 25(2):30–41, 2012. https://doi.org/10.5670/oceanog.2012.39.

[2] M. H. Alford, T. Peacock, J. A. MacKinnon, J .D. Nash, M. C Buijsman, L. R. Centurioni, S. Y. Chao, M. H. Chang, D. M. Farmer, O. B. Fringer, K. H. Fu, P. C. Gallacher, H. C. Graber, K. R. Helfrich, S. M. Jachec, C. R. Jackson, J. M. Klymak, D. S. Ko11, S. Jan, T. M. S. Johnston, S. Legg, I. H. Lee, R. C. Lien, M. J. Mercier, J. N. Moum, R. Musgrave, J. H. Park, A. I. Pickering, R. Pinkel1, L. Rainville2, S. R. Ramp, D. L. Rudnick, S. Sarkar, A. Scotti, H. L. Simmons, L. C. St Laurent, S. K. Venayagamoorthy, Y. H. Wang, J. Wang, Y. J. Yang, T. Paluszkiewicz, and T. Y. Tang. The formation and fate of internal waves in the South China Sea. *Nature*, 521:65–69, 2015. https://doi.org/10.1038/nature14399.

[3] D. J. Flynn. Mariner's tropical cyclone guide. Technical report, National Hurricane Center, National Weather Service, & National Oceanic and Atmospheric Administration, 2023. https://www.nhc.noaa.gov/marinersguide.pdf.

[4] E. S. Blake, T. B. Kimberlain, R. J. Berg, J. P. Cangialosi, and II J.L. Beven. Tropical cyclone report: Hurricane Wilma. Technical report, National Hurricane Center, 2013. https://www.nhc.noaa.gov/data/tcr/AL182012_Sandy.pdf.

[5] P. P. Papin. Tropical cyclone report: Hurricane Epsilon (AL272020). Technical report, National Hurricane Center, 2020. https://www.nhc.noaa.gov/data/tcr/AL272020_Epsilon.pdf.

[6] K. E. Silverthorne and J. M. Toole. Seasonal kinetic energy variability of near-inertial motions. *Journal of Physical Oceanography*, 39(4):1035–1049, 2009. https://doi.org/10.1175/2008JPO3920.1.

[7] R. A. Weller. The relation of near-inertial motions observed in the mixed layer during the JASIN (1978) experiment to the local wind stress and to the quasi-geostrophic flow field. *Journal of Physical Oceanography*, 12(10):2643–2660, 1982. https://doi.org/10.1175/1520-0485(1982)012%3C1122:TRONIM%3E2.0.CO;2.

[8] M. H. Alford. Sustained, full-water-column observations of internal waves and mixing near Mendocino Escarpment. *Journal of Physical Oceanography*, 40(12):2643–2660, 2010. https://doi.org/10.1175/2010JPO4502.1.

[9] S. Finette, M. H. Orr, A. Turgut, J. R. Apel, M. Badiey, C. S. Chiu, R. H. Headrick, J. N. Kemp, J. F. Lynch, A. E. Newhall, K. von der Heydt, B. Pasewark, S. N. Wolf, and D. Tielbuerger. Acoustic field variability induced by time evolving internal wave fields. *Journal of the Acoustical Society of America*, 108(3):957–972, 2000. https://doi.org/10.1121/1.1288662.

[10] P. Müller and A. Natarov. The Internal Wave Action Model (iwam). In *Near-Boundary Processes and Their Parameterization: Proc.'Aha Huliko'a Winter Workshop*, pages 95–105, University of Hawai'i at Mānoa, 2003. University of Hawai'i at Mānoa. http://www.soest.hawaii.edu/PubServices/1999pdfs/Muller.pdf.

[11] J. A. Colosi. Acoustic mode coupling induced by shallow water nonlinear internal waves: Sensitivity to environmental conditions and space-time scales of internal waves. *Journal of the Acoustical Society of America*, 123(3):1452–1464, 2008. https://doi.org/10.1121/1.2956471.

[12] R. T. Pollard. On the generation by winds of inertial waves in the ocean. *Deep Sea Research and Oceanographic Abstracts*, 17(4):795–812, 1970. https://doi.org/10.1016/0011-7471(70)90042-2.

[13] E. A. D'Asaro. The energy flux from the wind to near-inertial motions in the surface mixed layer. *Journal of Physical Oceanography*, 15(8):1043–1059, 1985. https://doi.org/10.1175/1520-0485(1985)015<1043:TEFFTW>2.0.CO;2.

[14] E. A. D'Asaro, C. C. Eriksen, M. D. Levine, C. A. Paulson, P. Niiler, and P. van Meurs. Upper-ocean inertial currents forced by a strong storm. Part I: Data and comparisons with linear theory. *Journal of Physical Oceanography*, 25(11):2909–2936, 1995. https://doi.org/10.1175/1520-0485(1995)025<2909:UOICFB>2.0.CO;2.

[15] S. R. Jayne, L. C. St. Laurent, and S. T. Gille. Connections between ocean bottom topography and earth's climate. *Oceanography*, 17(1):65–74, 2004. https://doi.org/10.5670/oceanog.2004.68.

[16] T. M. S. Johnston, S. Wang, C.-Y. Lee, J. N. Moum, D. L. Rudnick, and A. Sobel. Near-inertial wave propagation in the wake of Super Typhoon Mangkhut: Measurements from a profiling float array. *Journal of Geophysical Research: Oceans*, 126(2):15–17, 2020. https://doi.org/10.1029/2020JC016749.

[17] M. H. Alford. Internal swell generation: The spatial distribution of energy flux from the wind to mixed-layer near-inertial motions. *Journal of Physical Oceanography*, 31(8):2359–2368, 2001. https://doi.org/10.1175/1520-0485(2001)031<2359:ISGTSD>2.0.CO;2.

[18] J. Marshall, A. Andersson, N. Bates, W. Dewar, S. Doney, J. Edson, R. Ferrari, G. Forget, D. Fratantoni, M. Gregg, T. Joyce, K. Kelly, S. Lozier, R. Lumpkin, G. Maze, J. Palter, R. Samelson, K. Silverthorne, E. Skyllingstad, F. Straneo, L. Talley, L. Thomas, J. Toole, and R. Weller. The CLIMODE field campaign: Observing the cycle of convection and restratification over the Gulf Stream. *Bulletin of the American Meteorological Society*, 90(9):1337–1350, 2009. https://doi.org/10.1175/2009BAMS2706.1.

[19] M. H. Alford and M. Whitmont. Seasonal and spatial variability of near-inertial kinetic energy from historical mooring velocity records. *Journal of Physical Oceanography*, 37(8):2022–2037, 2007. https://doi.org/10.1175/JPO3106.1.

[20] W. G. Large, J. C. McWilliam, and P. P. Niiler. Upper ocean thermal response to strong autumnal forcing of the northeast Pacific. *Journal of Physical Oceanography*, 16(9):1524–1550, 1986. https://doi.org/10.1175/1520-0485(1986)016<1524:UOTRTS>2.0.CO;2.

[21] W. G. Large and G. B. Crawford. Observations and simulations of upper-ocean response to wind events during the Ocean Storms experiment. *Journal of Physical Oceanography*, 25(11):2831–2852, 1995. https://doi.org/10.1175/1520-0485(1995)025<2831:OASOUO>2.0.CO;2.

[22] A. J. Plueddemann and J. T. Farrar. Observations and models of the energy flux from the wind to mixed-layer inertial currents. *Deep Sea Research Part II*, 53(1–2):5–30, 2006. https://doi.org/10.1016/j.dsr2.2005.10.017.

[23] D. K. Lee and P. P. Niiler. The inertial chimney: The near-inertial energy drainage from the ocean surface to the deep layer. *Journal of Geophysical Research*, 103(C4):7579–7591, 1998. https://doi.org/10.1029/97JC03200.

[24] E. A. D'Asaro, T. B. Sanford, P. P. Niiler, and E. J. Terrill. Cold wake of Hurricane Frances. *Geophysical Research Letters*, 34(15):L15609, 2007. https://doi.org/10.1029/2007GL030160.

[25] A. E. Gill. On the behaviour of internal waves in the wakes of storms. *Journal of Physical Oceanography*, 14(7):1129–1151, 1984. https://doi.org/10.1175/1520-0485(1984)014<1129:OTBOIW>2.0.CO;2.

[26] S. C. Jones, P. A. Harr, J. Abraham, L. F. Bosart, P.J . Bowyer, J. L. Evans, D. E. Hanley, B. N. Hanstrum, R. E. Hart, F. Lalaurette, M. R. Sinclair, R. K. Smith, and C. Thorncroft. The extratropical transition of tropical cyclones: Forecast challenges, current understanding, and future directions. *Weather and Forecasting*, 18(6):1052–1092, 2003. https://doi.org/10.1175/1520-0434(2003)018<1052:TETOTC>2.0.CO;2.

[27] C. Evans, K. M. Wood, S. D. Aberson, H. M. Archambault, S. M. Milrad, L. F. Bosart, K. L. Corosiero, C. A. Davis, J. R. Dias Pinto, J. Doyle, C. Fogarty, T. J. Galarneau, C. M. Grans, K. S. Griffin, J. Gyakum, R. E. Hart,

N. Kitabatake, H. S. Lentink, R. McTaggart-Cowan, W. Perrie, J. F. D. Quinting, C. A. Reynolds, M. Riemer, E. A. Richie, Y. Sun, and F. Zhang. The extratropical transition and tropical cyclones. Part 1: Cyclone evolution and direct impacts. *Monthly Weather Review*, 145(11):4317–4344, 2017. https://doi.org/10.1175/MWR-D-17-0027.1.

[28] R. E. Hart and J. L Evans. A climatology of the extratropical transition of Atlantic tropical cyclones. *Journal of Climate*, 14(4):546–564, 2001. https://doi.org/10.1175/1520-0442(2001)014<0546:ACOTET>2.0.CO;2.

[29] R. H. Simpson. The hurricane disaster — potential scale. *Weatherwise*, 27(4):169–186, 2004. https://doi.org/10.1080/00431672.1974.9931702.

[30] J. A. Knox, J. D. Frye, J. D. Durkee, and C. M. Fuhrmann. Non-covective high winds associated with extratropical cyclones. *Geography Compass*, 5(2):63–89, 2011. https://doi.org/10.1111/j.1749-8198.2010.00395.x.

[31] R. T. Merrill. Tropical cyclone structure. Global guide to tropical cyclone forecasting. Technical Report TCP-31, World Meteorological Organization, Geneva, Switzerland, 1993.

[32] R. J. Pasch and L. A. Avila. Atlantic hurricane season of 1991. *Monthly Weather Review*, 120(11):2671–2687, 1992. https://doi.org/10.1175/1520-0493(1992)120<2671:AHSO>2.0.CO;2.

[33] R. E. Davis and R. Dolan. The "All Hallow's Eve" coastal storm: October 1991. *Journal of Coastal Research*, 8(4):978–983, 1992. https://www.jstor.org/stable/4298051.

[34] J. M. Cordeira and L. F. Bosart. Cyclone interactions and evolutions during the "Perfect Storms" of late October and early November 1991. *Monthly Weather Review*, 139(6):1683–1707, 2011. https://doi.org/10.1175/2010MWR3537.1.

[35] V. J. Cardone, R. E. Jensen, D. T. Resio, V. R. Swail, and A. T. Cox. Evaluation of contemporary ocean wave models in rare extreme events: The "Halloween Storm" of October 1991 and the "Storm of the Century" of March 1993. *Journal of Atmospheric and Oceanic Technology*, 13(1):198–230, 1996. https://doi.org/10.1175/1520-0426(1996)013<0198:EOCOWM>2.0.CO;2.

[36] S. Junger. *The Perfect Storm*. W. W. Norton & Company, 1997.

[37] J. L. Demuth, M. DeMaria, and J. A. Knaff. Improvement of Advanced Microwave Sounding Unit tropical cyclone intensity and size estimation algorithms. *Journal of Applied Meteorology and Climatology*, 45(11):1573–1581, 2006. https://doi.org/10.1175/JAM2429.1.

[38] C. T. Fogarty and E. S. Blake. The double life of Hurricane Sandy and a climatological perspective of these post-tropical giants [in "State of the Climate

2012"]. *Bulletin of the American Meteorological Society*, 94(8):S109–S110, 2013. https://doi.org/10.1175/2013BAMSStateoftheClimate.1.

[39] Jr. R. A. Pielke, J. Gratz, C. W. Landsea, D. Collins, M. A. Saunders, and R. Musulin. Normalized hurricane damage in the United States: 1900–2005. *Natural Hazards Review*, 9:29–42, 2008. https://doi.org/10.1061/(ASCE)1527-6988(2008)9:1(29).

[40] E. S. Blake, C. W. Landsea, and E. J. Gibney. The deadliest, costliest, and most intense United States tropical cyclones from 1851 to 2010 (and other frequently requested hurricane facts). NOAA Technical Memorandum NWS NHC-6, National Weather Service & National Hurricane Center, 2011. https://www.nhc.noaa.gov/pdf/nws-nhc-6.pdf.

[41] T. B. Sanford, J. F. Price, and J. B. Girton. Upper-ocean response to Hurricane Frances (2004) observed by profiling EM-APEX floats. *Journal of Physical Oceanography*, 41(6):1041–1056, 2011. https://doi.org/10.1175/2010JPO4313.1.

[42] G. J. Goni, R. E. Todd, S. R. Jayne, G. Halliwell, S. Glenn, J. Dong, R. Curry, R. Domingues, F. Bringas, L. Centurioni, S. F. DiMarco, T. Miles, J. Morell, L. Pomales, H.-S. Kim, P. E. Robbins, G. G. Gawarkiewicz, J. Wilkin, J. Heiderich, B. Baltes, J. J. Cione, G. Seroka, K. Knee, and E. R. Sanabia. Autonomous and Lagrangian ocean observations for Atlantic tropical cyclone studies and forecasts. *Oceanography*, 30(2):92–103, 2017. https://doi.org/10.5670/oceanog.2017.227.

[43] E. J. Lindstrom, A. Y Shcherbina, L. Rainville, J. T. Farrar, L. R. Centurioni, S. Dong, E. A D'Asaro, C. Eriksen, D. M. Fratantoni, B. A. Hodges, V. Hormann, W. S. Kessler, C. M. Lee, S. C. Riser, L. C. St. Laurent, and D. L. Volkov. Autonomous multi-platform observations during the Salinity Processes in the Upper-ocean Regional Study. *Oceanography*, 30(2):38–48, 2017. https://doi.org/10.5670/oceanog.2017.218.

[44] C. M. Lee, T. Paluszkiewicz, M. M. Omand, and R. E. Todd. Autonomous instruments significantly expand ocean observing: An introduction to the special issue on autonomous and Lagrangian platforms and sensors (ALPS). *Oceanography*, 30(2):15–17, 2017. https://doi.org/10.5670/oceanog.2017.211.

[45] R. Domingues, A. Kuwano-Yoshida, P. Chardon-Maldonado, R. E. Todd, G. Halliwell, H-S Kin, I-I Lin, K. Sato, T. Narazaki, L. K. Shay, T. Miles, S. Glenn, J. A. Zhang, and S. R. Jayne. Ocean observations in support of studies and forecasts of tropical and extratropical cyclones. *Frontiers in Marine Science*, 6:446, 2019. http://doi.org/10.3389/fmars.2019.00446.

[46] S. R. Jayne, W. B. Owens, P. E. Robbins, A. K. Ekholm, N. M. Bogue, and E. R. Sanabia. The Air-Launched Autonomous Micro Observer. *Journal of*

Atmospheric and Oceanic Technology, 39(4):491–502, 2022. https://doi.org/10.1175/JTECH-D-21-0046.1.

[47] R. Gall, J. Franklin, F. Marks, E. N. Rappaport, and F. Toepfer. The Hurricane Forecast Improvement Project. *Bulletin of the American Meteorological Society*, 94(3):329–343, 2013. https://doi.org/10.1175/BAMS-D-12-00071.1.

[48] J. P. Cangialosi, E. Blake, M. DeMaria, A. Penny, A. Latto, E. Rappaport, and V. Tallapragada. Recent progress in tropical cyclone intensity forecasting at the National Hurricane Center. *Weather and Forecasting*, 35(5):1913–1922, 2020. https://doi.org/10.1175/WAF-D-20-0059.1.

[49] T. B. Sanford, J. H. Dunlap, J. A. Carlson, D. C. Webb, and J. B. Girton. Autonomous velocity and density profiler: EM-APEX. In *Proc. Eighth Working Conf. on Current Measurement Technology*, pages 152–156, Southampton, United Kingdom, 2005. IEEE/OES. https://doi.org/10.1109/CCM.2005.1506361.

[50] P. G. Black, E. A. D'Asaro, T. B. Sanford, W. M. Drennan, J. A. Zhang, J. R. French, P. P. Niiler, Eric J. Terrill, and E. J. Walsh. Air-sea exchange in hurricanes: Synthesis of observations from the Coupled Boundary Layer Air-Sea Transfer experiment. *Bulletin of the American Meteorological Society*, 88(3):357–374, 2007. https://doi.org/10.1175/BAMS-88-3-357.

[51] T. B. Sanford, J. F. Price, J. B. Girton, and D. C. Webb. Highly resolved observations and simulations of the ocean response to a hurricane. *Geophysical Research Letters*, 34(13):L13604, 2007. https://doi.org/10.1029/2007GL029679.

[52] S. Chen, J. A. Cummings, J. M. Schmidt, E. R. Sanabia, and S. R. Jayne. Targeted ocean sampling for tropical cyclones. *Journal of Geophysical Research: Oceans*, 122(5):3505–3518, 2017. https://doi.org/10.1002/2017JC012727.

[53] E. D'Asaro, P. Black, L. Centurioni, P. Harr, S. R. Jayne, I.-I. Lin, C. Lee, J. Morzel, R. Mrvaljevic, P. P. Niiler, L. Rainville, T. Sanford, and T. Y. Tang. Typhoon-ocean interaction in the western North Pacific: Part 1. *Oceanography*, 24(4):24–31, 2011. http://doi.org/10.5670/oceanog.2011.91.

[54] X. Zhou, T. Hara, I. Ginis, E. D'Asaro, J. Y. Hsu, and B. G. Reichl. Drag coefficient and its sea state dependence under tropical cyclones. *Journal of Physical Oceanography*, 52(7):1447–1470, 2022. https://doi.org/10.1175/JPO-D-21-0246.1.

[55] J. F. Price. Upper ocean response to a hurricane. *Journal of Physical Oceanography*, 11(2):153–175, 1981. https://doi.org/10.1175/1520-0485(1981)011<0153:UORTAH>2.0.CO;2.

[56] Jr. G. R. Halliwell, L. K. Shay, J. K Brewster, and W. J. Teague. Evaluation and sensitivity analysis of an ocean model response to Hurricane Ivan. *Monthly Weather Review*, 139(3):921–945, 2011. https://doi.org/10.1175/2010MWR3104.1.

[57] E. R. Sanabia, B. S. Barrett, P. G. Black, S. Chen, and J. A. Cummings. Real-time upper-ocean temperature observations from aircraft during operational hurricane reconnaissance missions: AXBT demonstration project year one results. *Weather and Forecasting*, 28(6):1404–1422, 2013. https://doi.org/10.1175/WAF-D-12-00107.1.

[58] E. R. Sanabia and S. R. Jayne. Ocean observations under two major hurricanes: Evolution of the response across the storm wakes. *AGU Advances*, 1(3):e2019AV000161, 2020. https://doi.org/10.1029/2019AV000161.

[59] Jr. G. R. Halliwell, V. Kourafalou, M. Le Hénaff, L. K. Shay, and R. Atlas. OSSE impact analysis of airborne ocean surveys for improving upper-ocean dynamical and thermodynamical forecasts in the Gulf of Mexico. *Progress in Oceanography*, 130:32–46, 2015. https://doi.org/10.1016/j.pocean.2014.09.004.

[60] K. S. Mogensen, L. Magnusson, and J. R. Bidlot. Tropical cyclone sensitivity to ocean coupling in the ECMWF coupled model. *Journal of Geophysical Research: Oceans*, 122(5):4392–4412, 2017. https://doi.org/10.1002/2017JC012753.

[61] B. Jaimes de la Cruz, L. K. Shay, J. B. Wadler, and J. E. Rudzin. On the hyperbolicity of the bulk air-sea heat flux functions: Insights into the efficiency of air-sea moisture disequilibrium for tropical cyclone intensification. *Monthly Weather Review*, 149(5):1517–1534, 2021. https://doi.org/10.1175/MWR-D-20-0324.1.

[62] M. DeMaria, M. Mainelli, L. K. Shay, J. A. Knaff, and J. Kaplan. Further improvements to the Statistical Hurricane Intensity Prediction Scheme (SHIPS). *Weather and Forecasting*, 20(4):531–543, 2005. https://doi.org/10.1175/WAF862.1.

[63] M. Mainelli, M. DeMaria, L. K. Shay, and G. Goni. Application of oceanic heat content estimation to operational forecasting of recent Atlantic category 5 hurricanes. *Weather and Forecasting*, 23(1):3–16, 2008. https://doi.org/10.1175/2007WAF2006111.1.

[64] T. N. Miles, D. Zhang, G. R. Foltz, J. A. Zhang, C. Meinig, F. R. Bringas, J. Triñanes, M. Le Hénaff, M. F. Aristizabal Vargas, S. Coakley, C.R. Edwards, D. Gong, R. E. Todd, M. J. Oliver, W. D. Wilson, K. Whilden, B. Kirkpatrick, P. Chardon-Maldonado, J. M. Morell, D. Hernandez, G. Kuska, C. D. Stienbarger, K. Bailey, C. Zhang, S. M. Glenn, and G. J. Goni. Uncrewed ocean gliders and Saildrones support hurricane forecasting and research. *Oceanography*, 34(4):78–81, 2022. https://doi.org/10.5670/oceanog.2021.supplement.02-28.

[65] S. R. Jayne and N. M. Bogue. Air-deployable profiling floats. *Oceanography*, 30(2):29–31, 2017. https://doi.org/10.5670/oceanog.2017.214.

[66] L. Stramma, P. Cornillon, and J. Price. Satellite observations of sea surface cooling by hurricanes. *Journal of Geophysical Research*, 91(C4):5031–5035, 1986. https://doi.org/10.1029/JC091iC04p05031.

[67] R. K. Mrvaljevic, P. G. Black, L. R. Centurioni, Y.-T. Chang, E. A. D'Asaro, S. R. Jayne, C. M. Lee, R.-C. Lien, I-I Lin, J. Morzel, P. P. Niiler, L. Rainville, and T. B. Sanford. Observations of the cold wake of Typhoon Fanapi (2010). *Geophysical Research Letters*, 40(2):316–321, 2013. https://doi.org/10.1029/2012GL054282.

[68] K. Balaguru, G. R. Foltz, L. R. Leung, E. D'Asaro, K. A. Emanuel, H. Liuand, and S. E. Zedler. Dynamic potential intensity: An improved representation of the ocean's impact on tropical cyclones. *Geophysical Research Letters*, 42(16):6739–6746, 2015. https://doi.org/10.1002/2015GL064822.

[69] S. Chen, R. L. Elsberry, and P. A. Harr. Modeling interaction of a tropical cyclone with its cold wake. *Journal of the Atmospheric Sciences*, 74(12):3981–4001, 2017. https://doi.org/10.1175/JAS-D-16-0246.1.

[70] S. Brand. The effects on a tropical cyclone of cooler surface waters due to upwelling and mixing produced by a prior tropical cyclone. *Journal of Applied Meteorology and Climatology*, 10(5):865–874, 1971. https://doi.org/10.1175/1520-0450(1971)010%3C0865:TEOATC%3E2.0.CO;2.

[71] K. Balaguru, S. Taraphdar, L. R. Leung, G. R. Foltz, and J. A. Knaff. Cyclone-cyclone interactions through the ocean pathway. *Geophysical Research Letters*, 41(19):6855–6862, 2014. https://doi.org/10.1002/2014GL061489.

[72] K. B. Karnauskas, L. Zhang, and K. A. Emanuel. The feedback of cold wakes on tropical cyclones. *Geophysical Research Letters*, 48(7):e2020GL091676, 2021. https://doi.org/10.1029/2020GL091676.

[73] R. J. Pasch, E. S. Blake, H. D. Cobb III, and D. P. Roberts. Tropical cyclone report: Hurricane Sandy (AL182012). Technical report, National Hurricane Center, 2006. https://www.nhc.noaa.gov/data/tcr/AL252005_Wilma.pdf.

[74] A. P. Martin, I. P. Wade, K. J. Richards, and K. J. Heywood. The PRIME eddy. *Journal of Marine Research*, 56(2):439–462, 1998. https://doi.org/10.1357/002224098321822375.

[75] I. P. Wade and K. J. Heywood. Tracking the PRIME eddy using satellite altimetry. *Deep Sea Research Part II*, 48(4–5):725–737, 2001. https://doi.org/10.1016/S0967-0645(00)00094-1.

[76] C. A. Clayson, J. B. Edson, S. M Faluotico, T. M. Lanagan, and J. M. Toole. The X-Spar: An expendable, low-cost, air-sea flux buoy. *Journal of Atmospheric and Oceanic Technology*, page submitted, 2023.

[77] J. B. Edson, A. A. Hinton, K. E. Prada, J. E. Hare, and C .W. Fairall. Direct covariance flux estimates from mobile platforms at sea. *Journal of Atmospheric and Oceanic Technology*, 15(2):547–562, 1998. https://doi.org/10.1175/1520-0426(1998)015<0547:DCFEFM>2.0.CO;2.

[78] E. Lindstrom, F. Bryan, and R. Schmitt. SPURS: Salinity Processes in the Upper-ocean Regional Study — the North Atlantic experiment. *Oceanography*, 28(1):14–19, 2015. http://doi.org/10.5670/oceanog.2015.01.

[79] L. M. Smith, J. A. Barth, D. S. Kelley, A. Plueddemann, I. Rodero, G. A. Ulses, M. F. Vardaro, and R. Weller. The Ocean Observatories Initiatives. *Oceanography*, 31(1):16–35, 2018. https://doi.org/10.5670/oceanog.2018.105.

[80] N. Smith, W. S. Kessler, S. Cravatte, J. Sprintall, S. Wijffels, M. F. Cronin, A. Sutton, Y. L. Serra, B. Dewitte, P. G. Strutton, K. Hill, A. Sen Gupta, X. Lin, K. Takahashi, D. Chen, and S. Brunner. Tropical Pacific Observing System. *Frontiers in Marine Science*, 6:31, 2019. http://doi.org/10.3389/fmars.2019.00031.

[81] H. C. Graber, E. A. Terray, M. A. Donelan, W. M. Drennan, and J. C. van Leer. ASIS – A new air-sea interaction spar buoy: Design and performance at sea. *Journal of Atmospheric and Oceanic Technology*, 17(5):708–720, 2000. https://doi.org/10.1175/1520-0426(2000)017<0708:AANASI>2.0.CO;2.

[82] J. B. Edson, V. Jampana, R. A. Weller, S. Bigorre, A. J. Plueddemann, C. W. Fairall, S. D. Miller, L. Mahrt, D. Vickers, and H. Hersbach. On the exchange of momentum over the open ocean. *Journal of Physical Oceanography*, 43(8):1589–1610, 2013. https://doi.org/10.1175/JPO-D-12-0173.1.

[83] W. J. Gould. From Swallow floats to Argo — the development of neutrally buoyant floats. *Deep-Sea Research Part II*, 52(3–4):529–543, 2005. https://doi.org/10.1016/j.dsr2.2004.12.005.

[84] D. L. Rudnick. Ocean research enabled by underwater gliders. *Annual Review of Marine Science*, 8(1):519–541, 2016. https://doi.org/10.1146/annurev-marine-122414-033913.

[85] C. Eriksen, T. Osse, R. Light, T. Wen, T. Lehman, P. Sabin, J. Ballard, and A. Chiodi. Seaglider: A long-range autonomous underwater vehicle for oceanographic research. *IEEE Journal of Oceanic Engineering*, 26(4):424–436, 2001. https://doi.org/10.1109/48.972073.

[86] L. Rainville, C. M. Lee, K. Arulananthan, S. U. P. Jinadasa, H. J. S. Fernando, W. N. C. Priyadarshani, and H. Wijesekera. Water mass exchanges between

the Bay of Bengal and Arabian Sea from multiyear sampling with autonomous gliders. *Journal of Physical Oceanography*, 52(10):2377–2396, 2022. https://doi.org/10.1175/JPO-D-21-0279.1.

[87] R. Domingues, M. Le Hénaff, G. R. Halliwell, J. A. Zhang, F. Bringas, P. Chardon-Maldonado, H. Kim, J. M. Morell, and G. J. Goni. Ocean conditions and the intensification of three major Atlantic hurricanes in 2017. *Monthly Weather Review*, 149(5):1265–1286, 2021. https://doi.org/10.1175/MWR-D-20-0100.1.

[88] R. E. Todd, D. L. Rudnick, J. T. Sherman, W. B. Owens, and L. George. Absolute velocity estimates from autonomous underwater gliders equipped with Doppler current profilers. *Journal of Atmospheric and Oceanic Technology*, 34(2):309–333, 2017. https://doi.org/10.1029/2010JC006536.

[89] M. Visbeck. Deep velocity profiling using lowered acoustic Doppler current profilers: Bottom track and inverse solutions. *Journal of Atmospheric and Oceanic Technology*, 19(5):794–807, 2017. https://doi.org/10.1175/1520-0426(2002)019<0794:DVPULA>2.0.CO;2.

[90] R. E. Todd, D. L. Rudnick, M. R. Mazloff, R. E. Davis, and B. D. Cornuelle. Poleward flows in the southern California Current System: Glider observations and numerical simulation. *Journal of Geophysical Research*, 116(C2):C02026, 2011. https://doi.org/10.1029/2010JC006536.

[91] A. M. Thurnherr, D. Symonds, and L. St. Laurent. Processing explorer ADCP data collected on Slocum gliders using the LADCP shear method. In *2015 IEEE/OES Eleventh Current, Waves and Turbulence Measurement (CWTM)*, pages 1–7, St. Petersburg, FL, March 2015. IEEE. https://doi.org/10.1109/CWTM.2015.7098134.

[92] M. N. Guidhir, D. Kennedy, A. Berry, B. Christy, C. Clancy, C. Creamer, G. Westbrook, and S. Gallagher. Irish wave data — rogues, analysis and continuity. *Journal of Marine Science and Engineering*, 10(8):1073, 2022. https://doi.org/10.3390/jmse10081073.

[93] P. C. Liu and G. S. Miller. Wavelet transforms and ocean current data analysis. *Journal of Atmospheric and Oceanic Technology*, 13(5):1090–1099, 1996. https://doi.org/10.1175/1520-0426(1996)013<1090:WTAOCD>2.0.CO;2.